Theoretical and Experimental Foundations of Coherent Pulse Stacking Amplification

by

John M. Ruppe III

A dissertation submitted in partial fulfillment
of the requirements for the degree of
Doctor of Philosophy
(Electrical Engineering)
in the University of Michigan
2017

Doctoral Committee
Professor Almantas Galvanauskas, Chair
Professor Steven T. Cundiff
Professor Karl M. Krushelnick
Associate Research Scientist John A. Nees
Professor Herbert G. Winful

John M. Ruppe III

jmruppe@umich.edu

ORCID iD: 0000-0002-6942-9468

Dedication

This thesis is dedicated to my wife Kristen.

Acknowledgements

I would like to thank all of the people who I have encountered on this academic journey that have believed in me and provided much needed guidance and support.

I would first like to thank Professor Galvanauskas. You have forever changed the way I look at and try to solve problems (not just physics based problems, but all types of problems that one encounters in life). I have been extremely lucky to have had you as an advisor, and I have learned an immeasurable amount of information from you that I will carry with me. I would also like to thank you for believing in me and instilling a confidence that was not there when I first joined your group, and for that I will be forever grateful.

Next I would like to thank John Nees. Your experimental knowledge and sheer joy of performing experiments in the lab are incredible. It scares me to think about where the status of the experiments performed in this thesis would be without your guidance. I would also like to thank you for believing in me and for listening and talking through some of my own (potentially crazy) ideas.

I would like to thank all of my current and former colleagues: Hanzhang Pei, Tong Zhou, Morteza Sheikhsofla, Siyun Chen, Cheng Zhu, Weizhi Du, I-Ning Hu, and Michael Haines. Demonstrating and developing this new technique has really been a team effort, and it would not be possible without all of your hard work and dedication.

I would also like to thank Russell Wilcox and Wim Leemans from Berkeley National Lab as well as Jay Dawson, Paul Pax, and Diana Chen from Livermore National lab for their collaboration on this project.

Finally I would like to thank the friends I made in Ann Arbor for always being there when I needed you most.

Table of Contents

List of Figures

List of Tables

Abstract

Coherent combining of fiber lasers has the potential to be the system of choice for next generation high peak power high average power laser systems, which could enable a myriad of new scientific and industrial applications. These fiber based systems have inherently good average power handling capabilities; however, new technologies are required in order to boost the pulse energy into the desired range. This thesis focuses on a novel time domain coherent combining technique called coherent pulse stacking amplification which has the ability to increase the pulse energy by two orders of magnitude for each fiber.

In this thesis, we develop the theoretical and experimental foundations of the coherent pulse stacking amplification (CPSA) technique. We build up the theoretical framework behind CPSA, which is based on the concept of coherently combining (a.k.a. stacking) a burst of pulses in the time domain into a single pulse. We give a recipe for how to design such a burst of pulses and a recipe for how to design the system of interferometers that can stack such pulses. We propose a method to stabilize these interferometers and also develop the theory for how this stabilization method performs in the presence of environmental noise sources. We also give several options for the spatial arrangement of these interferometers and mathematically analyze the pros and cons of each option. Finally we perform several proof-of-principle experiments in order to illustrate the efficacy of CPSA. These experiments show that a burst of up to 81 pulses can be stacked into a single pulse and that such a burst can have a total energy that is nearly two orders of magnitude more than what can be obtained with a single pulse without using CPSA.

To summarize, this thesis provides the necessary theoretical analysis and proof-of-principle experiments to verify the CPSA technique. When used in combination with coherent spatial combining, CPSA can enable next generation fiber based high peak power high average power laser systems.

Chapter 1 Introduction

1.1 Background

Since the invention of the laser in the 1950s by Townes, Basov, and Prokhorov, numerous applications of coherent laser radiation have arisen [1]. These applications drive further laser source development, which in turn leads to new applications. As the laser source development gets more mature, the laser performance parameters (e.g. average power, peak power, etc.) get pushed to the physical limit of operation, and new innovations are required in order to break through those physical limitations. One of the most important of these innovations in the area of high intensity lasers was the development of chirped pulse amplification (CPA) by Strickland and Mourou in 1985 [2]. Chirped pulse amplification has allowed laser peak intensities to scale from 10^{15} W/cm^2 in 1985 to 10^{22} W/cm^2 in 2004, thus opening up many new regimes of high field science [3]. CPA works by reducing the peak power in the laser amplifier by nearly 5 orders of magnitude, thus avoiding severe nonlinear effects in the laser amplifier (including damage). The peak power is reduced by stretching the pulse in the time domain by nearly 5 orders of magnitude (to ~1ns) before the laser amplifier and compressing the pulse back to ultrashort durations (~10fs to ~1ps) after the amplifier. Therefore for many laser amplifier technologies (e.g. Ti:sapphire), the CPA allows the corresponding 5-6 orders of magnitude energy increase, which then can be further complemented by approximately another 2 orders of magnitude via aperture scaling (to >150mm diameter) to reach the maximum achievable energies (~1J to >100J) [4]. However, some laser amplifier technologies (e.g. fiber amplifiers) are limited in transverse aperture scaling (<150μm diameter for single mode

operation) [5,6], and in these media CPA does not permit efficient extraction of the stored energy. Indeed, the CPA enabled energies from fiber amplifiers are approximately 2 orders of magnitude lower (~100μJ to ~1mJ for single mode operation) than the stored energy.

1.2 Fiber Chirped Pulse Amplification (FCPA) and Energy Scaling Limitations in Fibers

The scaling of pulse energies and peak powers from fiber chirped pulse amplification (FCPA) has traditionally been accomplished by increasing the core diameter of the fiber while retaining single mode operation, since the stretched pulse duration is limited. Various different optical fiber geometries have been proposed that allow the scaling of the core diameter with single mode operation. Several of these geometries are shown below in Fig. 1.1 [7,8,9,10]. However, this coarse scaling is limited to approximately 50μm to 100μm mode field diameter due to various constraints. Therefore, the achievable fiber CPA energies are limited by nonlinearities in the fiber, and are significantly below the stored energy level.

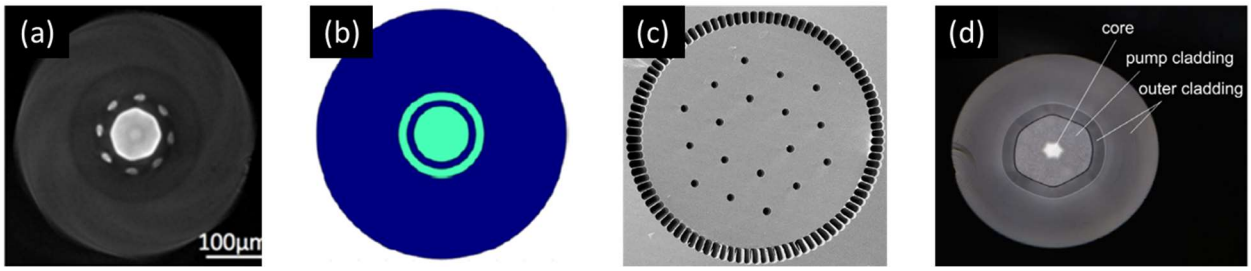

Figure 1.1: (a) Chirally coupled core (CCC) fiber, (b) Single trench fiber, (c) Large pitch fiber, (d) Step index fiber

The primary limitation on the energy scaling for these optical fibers comes from the $\chi^{(3)}$ nonlinearity, or Kerr nonlinearity, which is present in all known optical materials [11]. This nonlinearity is responsible for causing the index of refraction of the optical fiber to become a function of the laser intensity, as well as for causing four wave mixing effects. This nonlinearity is accumulated as the laser pulse passes through more and more optical material, and the total effect can be characterized by the B-integral, which is defined in Eq. 1.1 below [12].

$$B = \frac{2\pi}{\lambda} \int n_2(z) I_{peak}(z) dz \tag{1.1}$$

Where in Eq. 1.1 λ is the central wavelength, n_2 is the nonlinear refractive index, and I_{peak} is the peak intensity of the laser pulse. The integral is done over the full optical path of the laser pulse. As a reference, the value of n_2 in optical fibers made from fused silica has been measured to be $n_{2,silica} \approx 2.5 \times 10^{-16} cm^2 / W$ [13]. In general, distortions in the compressed pulse increase as the B integral increases [11]. Because distortions accumulate gradually with the B integral, there is no sharp threshold in B integral value at which nonlinearities suddenly arise. However, it is customary in the field to use an approximate rule of thumb of $B < \pi$, for which, these distortions are considered negligible [11].

While in FCPA systems the practical limitations on the pulse energy are set by self-phase modulation (and four wave mixing), it is worth noting that the ultimate energy limitations are defined by fiber thresholds for optical damage and nonlinear self-focusing. Optical damage effects in bulk fused silica fibers scale with the square root of the pulse duration and have been measured to occur at a reference fluence level of $U^*_{ref} = 800$ J/cm^2 at a pulse duration of $\tau_{ref} = 6ns$, so then the formula for the fluence at which bulk damage will occur is given by $U^*_{pulse} = U^*_{ref} \sqrt{\frac{\tau_{pulse}}{\tau_{ref}}}$ for a pulse duration of τ_{pulse} [15]. Another fundamental limit is nonlinear self-focusing (caused by the same $\chi^{(3)}$ nonlinearity), which will cause the beam to self-focus and therefore destroy the optical fiber if the peak power exceeds a critical peak power, which for optical fibers is in the range of $P_{crit} \approx 3 \times 10^6$ W to 6×10^6 W for a central wavelength of 1μm [12].

In order to properly determine the amount of nonlinearity acquired by the amplified pulse, it is necessary to account for the changing pulse shape in the power amplifier, which occurs due to strong saturation in this stage. This reshaping effect can be described by the Franz-Nodvick theory [14]. This theory is valid when the pulse is much shorter than the gain recovery time, so the pump has a negligible effect on the population inversion in the amplifier during pulse amplification. Consequentially, the front of the laser pulse will see the maximum inversion, and therefore the largest gain, while the back of the pulse will see a lower/depleted inversion, and therefore a lower gain. This time dependent gain causes the laser pulse to be reshaped. The magnitude of this reshaping depends on the ratio between the extracted energy and the stored energy.

In the Franz-Nodvick theory, the total stored energy in the fiber can be calculated as:

$$E_{stored} = U_{sat} \ln\left[G_0\right] A_{eff} \tag{1.2}$$

In Eq. 1.2 the total stored energy is dependent on the saturation fluence, which can be related to the stimulated emission cross section σ_e through $U_{sat} = \frac{\hbar\omega}{\sigma_e 2^*}$, where $\hbar\omega$ is the photon energy, and 2^* is a saturation factor that takes into account how quickly the lower laser level population empties compared to the pulse duration ($2^* \approx 1$ for rapidly emptying lower level) [14]. Also A_{eff} is the effective mode field area for the fiber. Knowledge of the stored energy is important not only for knowing how much energy can be extracted from the fiber amplifier, but also is critical in determining the degree of pulse reshaping that will occur under given conditions in the fiber amplifier.

Understanding pulse reshaping effects is instrumental both for calculating the accumulated B integral and for determining the optimum conditions under which this B integral

can be minimized. For the same energy, if the B integral is equal at all points along the pulse, then the peak B integral is minimized (as opposed to a pulse shape where the B integral varies along the pulse). By utilizing the Franz-Nodvick theory, a formula for an optical pulse intensity profile in the time domain with a minimum B-integral has been developed in Chapter 2 in Eq. 2.14. This optimal pulse profile is roughly flat top for output pulses from a weakly saturated amplifier, and becomes a decaying function with an increasing decay rate as the degree of saturation increases. Since in fiber CPA, nonlinearity occurs before significant saturation, these effects are of minor importance. However, in the coherent pulse stacking amplification (CPSA) technique described in this thesis where nearly all of the stored energy can be extracted, consideration of these effects becomes crucial.

The formula for an optical intensity profile with a minimum B-integral (Eq. 2.14) can be used to determine the nonlinearity-limited intensity extracted from the fiber amplifier, which is the energy per unit area per unit time that can be extracted from the amplifier with a specified B-integral:

$$I_{\phi_{NL}\text{limited}}(t) = I_{out}(t) - I_{in}(t) = \left\{\frac{\phi_{NL}}{n_2 k_0 L}\right\} \ln[G_0] \exp\left[\frac{-\phi_{NL}}{n_2 k_0 L U_{sat}} t\right] \tag{1.3}$$

Where here, ϕ_{NL} is the B-integral, L is the measured length of the fiber, n_2 is the nonlinear refractive index, k_0 is the central wavevector, G_0 is the small signal gain, and U_{sat} is the saturation fluence. By utilizing Eq. 1.3, a dependence of the nonlinearity-limited fluence (energy per unit area that can be extracted with a specified B-integral) $\left(U_{\phi_{NL}\text{limited}}(\tau) = \int_0^{\tau} I_{\phi_{NL}\text{limited}}(t)\,dt\right)$ with $B = \phi_{NL}$, as a function of the pulse duration τ can be determined:

$$U_{\phi_{NL}\text{limited}}(\tau) = U_{sat} g_0 L \left(1 - \exp\left[\frac{-\phi_{NL}}{n_2 k_0 L U_{sat}} \tau \right] \right) = U_{stored} f \tag{1.4}$$

The small-signal gain is $G_0(L) = \exp[g_0 L]$, with the g_0 term being the small signal gain coefficient in units of m^{-1}. Here f denotes the ratio between the extracted energy, which produces a given B-integral for a specified pulse duration, and the total stored energy in the fiber $f = \left(1 - \exp\left[\frac{-\phi_{NL}}{n_2 k_0 L U_{sat}} \tau \right] \right)$. It is worth noting here that ϕ_{NL} and τ can be treated as independent parameters. For example, it is clear that by increasing the pulse duration for a fixed B-integral, the extracted energy can become arbitrarily close to the total stored energy in the fiber. In this case the pulse shape is kept constant. Alternatively if the product $\phi_{NL}\tau$ is kept constant, then increasing the pulse duration will correspondingly reduce the B-integral while keeping the ratio f fixed. In this situation the pulse shape must be changed with increasing pulse duration. In general, one can keep increasing the pulse duration τ while simultaneously decreasing the B-integral (via the proper change in the output pulse shape according to Eq. 2.14) in such a way that the ratio f approaches 1.

It is interesting to note that the ratio between the duration of a properly shaped pulse and the fiber length is completely determined by the specific selection of f and ϕ_{NL} values: $\frac{\tau_{f,\phi_{NL}}}{L} = \frac{n_2 k_0 U_{sat} \ln\left[\frac{1}{1-f} \right]}{\phi_{NL}}$. For example, for a typical saturation fluence in Yb-doped fiber at around 1.04μm wavelength of $U_{sat} = 100$ J/cm^2, and selecting a B-integral of $\phi_{NL} = \pi$, with

extraction of 90% of the stored energy $(f = 0.9)$, the pulse duration per unit fiber length can be calculated as $\frac{\tau_{0.9,\pi}}{L} \approx 110$ ns/m.

A plot of the nonlinearity-limited fluence as a function of the pulse duration (Eq. 1.4) is shown below in Fig. 1.2. The parameters used for the calculation are: $U_{sat} = 100$ J/cm^2, $\phi_{NL} = \pi$, $n_2 = 2.5\times10^{-16}$ cm^2/W, $k_0 = 6.1\times10^6$ m^{-1}, $L = 1$ m. We use several values of the small signal gain G_0 corresponding to different levels of population inversion.

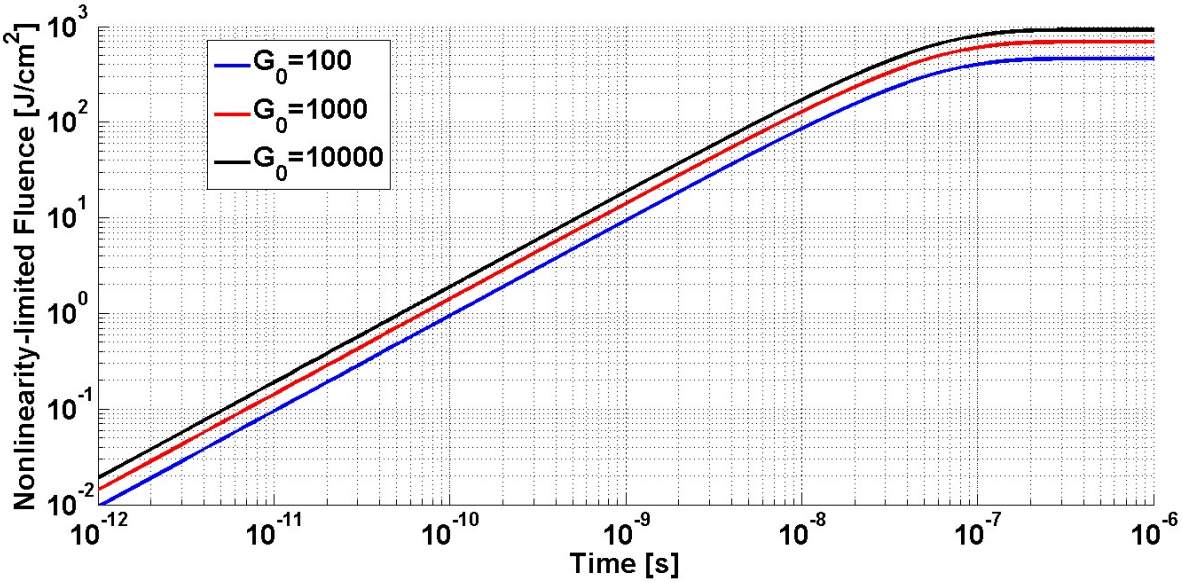

Figure 1.2: Calculated nonlinearity limited fluence as a function of pulse duration for several values of small signal gain

It is evident from Fig. 1.2 that in this case for pulse durations less than ~100ns, the energy extraction is limited by the nonlinearity-limited fluence (i.e. B-integral). While for pulses longer than ~100ns, the energy extraction becomes limited by the stored energy. For example, for 1ns pulses, the energy extraction is limited by nonlinearity to about 15J/cm^2 to 20J/cm^2, which is much less than the total stored fluence of 500J/cm^2 to 1000J/cm^2. This stored energy can be accessed with pulse duration longer than ~100ns, consistent with the previous discussion.

It is useful to convert these fluences into energies by considering the typical mode areas of large core fibers. Flexible optical fibers have been demonstrated with mode field diameters (MFD) of more than 40μm, yielding an FCPA energy of ~200μJ for 1ns pulses and a total stored energy of ~10mJ. Photonic crystal rod type fibers can have mode field diameters up to 90μm, which would yield an FCPA energy of ~1mJ for 1ns pulses and a total stored energy of ~50mJ. We replot Fig. 1.2 below (in Fig. 1.3) for these typical mode field areas along with the self-focusing threshold and the optical damage thresholds, and assuming a small signal gain of $G_0 = 1000$. Fig. 1.3 illustrates that the energy extraction from these fiber amplifiers is limited by the B-integral for shorter pulse durations and by the stored energy for larger pulse durations, rather than by optical damage or self-focusing.

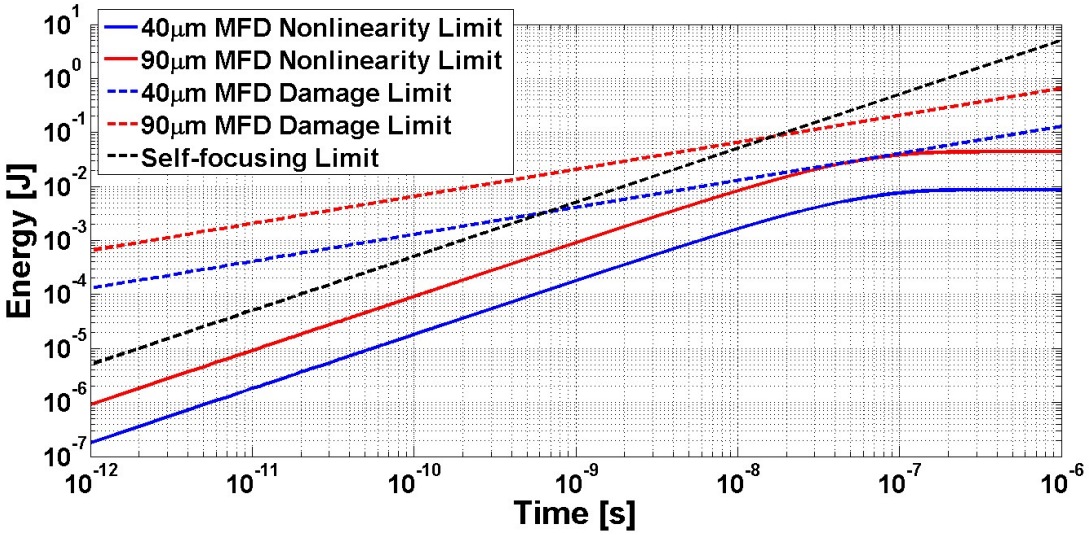

Figure 1.3: Fiber amplifier energy limitations including limits due to nonlinearity, bulk damage, and self-focusing

Traditional grating based compressors cannot handle these ~100ns long pulse durations due to the extremely large grating size that would be required to extract nearly all of the stored energy. The grating based compressors scaling is such that a 10cm grating can be used to compress a 1ns pulse, resulting in a scaling of roughly 10cm/ns [16]. Therefore in order to reach the requisite 100ns pulse durations, 10m gratings would be required, which is currently not

technologically feasible. However, these ~100ns long pulse durations can be achieved using the coherent pulse stacking amplification (CPSA) technique.

1.3 Power and Energy Scaling and Coherent Combining of Fiber Laser Arrays

Future applications of high intensity laser systems (e.g. particle accelerators) are relying on achieving high peak power lasers with high repetition rates, while maintaining good wall-plug efficiency. Some of the key laser parameters have been specified in a paper by Leemans, and for a 10GeV electron acceleration stage, the laser driver will need to produce 30J, 130fs pulses at a repetition rate of 10's kHz (100's kW average power) with a wall plug efficiency exceeding 25% [17]. Current laser technology is not capable of achieving these results, so new innovations are required in order to make these laser based electron accelerators a reality.

Conventional solid state laser technology based on Ti:Sapphire and/or Nd:Glass slabs has had great success in scaling to the required pulse energy and pulse durations (and beyond). However, thus far this technology has been limited to average powers ~100W, which is orders of magnitude less than the 100's kW required [18]. Various approaches to improving the thermal power handling of these laser systems (which is what limits the average power) include cryogenic cooling of the laser crystal and flowing cold Helium across the face of an amplifier slab. These improvements in thermal conditions have allowed average power scaling up to ~1kW, but scaling up to 100's kW with these materials does not seem feasible. There is some investigative work being done into other laser materials (e.g. Tm:YLF) that could potentially scale beyond 1kW with the multi-slab geometry; however, it is unclear what average powers can ultimately be achieved with such a system.

A radically different approach to power and energy scaling is through the use of coherently combined fiber amplifier arrays. One single-mode CW fiber laser can output as much

as 10kW average power [19], and nanosecond pulsed fiber lasers have been scaled to over 1kW average power in a single fiber channel [20], albeit not with single-mode beam quality. The primary challenge for fiber amplifiers is achieving large pulse energies due to the relatively small core areas, as discussed in section 1.2, which cause nonlinear effects to build up and ultimately limit the maximum energy. Since a single fiber amplifier can be quite compact, many of these channels can be coherently combined to exceed the energy and average power limitations of a single fiber. Utilizing an array of these fibers with pulse durations around 1ns, as done in conventional FCPA, will require 10^4-10^5 parallel fiber channels in order to reach a total pulse energy of 10J, since a single fiber can only output 100μJ-1mJ [21] (as shown in Fig. 1.3). Clearly such a large number channels would be a significant technological challenge.

Considering the results of Fig. 1.3, one can see that extraction of the full stored energy would allow a reduction in the array size by a factor of 10^2 (down to 10^2 to 10^3 channels), provided that pulses longer than ~100ns are used as opposed to conventional FCPA with ~1ns pulses. Up to now, it was not possible to achieve these pulse durations. This thesis demonstrates and develops a new method for solving this problem called coherent pulse stacking amplification (CPSA), in which these long pulse durations and the energy close to the stored energy are achieved.

1.4 Coherent Pulse Stacking Amplification (CPSA)

The coherent pulse stacking amplification (CPSA) technique is based on coherent time-domain pulse combining, which complements conventional CPA to effectively extend the pulse duration by orders of magnitude. Principally, CPSA consists of two parts, as illustrated in Fig. 1.4 below. The pulse forming subsystem prior to amplification creates a properly conditioned (i.e. stackable) burst of stretched pulses. This burst can contain from several up to >100 pulses

with a resulting burst duration ranging from several nanoseconds to >100ns. The pulse stacking subsystem after amplification stacks this burst into a single stretched pulse (typically ~1ns long), which is then compressed in a standard diffraction grating arrangement to an ultrashort duration.

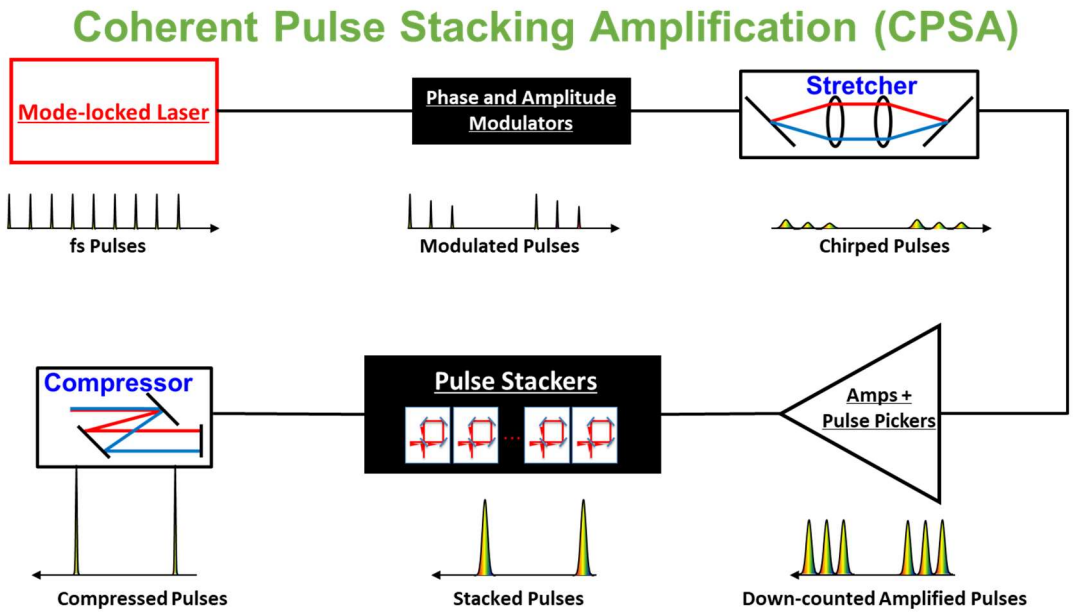

Figure 1.4: Coherent pulse stacking amplification (CPSA) single fiber channel diagram

Pulse burst formation is accomplished by taking a pulse train directly from a modelocked laser and amplitude and phase modulating the pulses to synthesize a stackable burst by using a pair of fast fiber pigtailed electro-optic modulators, and therefore is very compact and monolithically integrated. Stackability is enabled by imprinting the proper phase on each pulse in the burst. Amplitude modulation is used to carve out the burst, and to pre-shape it such that it will compensate strong saturation effects during amplification, thus producing at the output of the final amplifier a minimum-nonlinearity burst profile described by Eq. 2.14. The pulse stackers consist of free-space interferometers that are phase controlled to achieve coherent time domain pulse combining (i.e. pulse stacking). The free-space arrangement allows the pulse stackers to be scalable to high energies and average powers. The important practical aspects are that these pulse stackers can be configured using only a few (e.g. 5 to 10) interferometers,

arranged in a compact fashion (described in more detail in Chapter 4), and that they can accommodate a wide range of pulse burst intensity profiles required for efficient energy extraction under various saturation conditions (described in more detail in Chapter 2).

We have shown in [31] that Gires-Tournois interferometers (GTIs) can be used for pulse stacking. A Gire-Tournois Interferometer (GTI) can be configured as a travelling wave optical cavity which consists of a partially reflecting front mirror and other nearly 100% reflectivity mirrors that form the rest of the cavity, where the cavity roundtrip time is defined to be an integer number of oscillator periods (up to a fraction of the carrier wave) [31]. In order to explain how the pulse stacking works, let's first consider a single GTI cavity. A single GTI whose roundtrip period is equal to that of the modelocked oscillator (up to a fraction of an optical cycle) is characterized by its front mirror reflectivity and its roundtrip phase for the carrier wave (cavity phase). The 2 degrees of freedom of this GTI (its reflectivity and cavity phase) can be chosen to controllably stack 2 pulses [31]. Therefore, a sequence of M of these GTIs has 2M degrees of freedom (only 2M-1 are independent), and it can be shown that these degrees of freedom can be optimized to stack approximately 2M pulses (i.e. $2M \pm 1$) with a prescribed amplitude profile [31]. Note, however, that the number of cavities is equal to half the number of pulses and this linear scaling would lead to very complicated stacking arrangements. This can be overcome by multiplexing cavities with different lengths (albeit with an integer number of oscillator periods for each cavity). As it is explained in more detail in Chapter 2, there is a great variety of multiplexed cavity configurations that are possible.

As an example, we can consider a conceptually simple multiplex of M+M cavities, which is a sequence of M cavities with a roundtrip period equal to that of the oscillator followed by a sequence of M cavities with a roundtrip period equal to 2M oscillator periods. This

configuration can be used to stack a burst containing $4M^2$ pulses. The original burst containing $4M^2$ pulses will be stacked by the first sequence of M GTIs into a new burst containing 2M pulses, but the pulses in the new burst will now be separated in time by 2M oscillator periods. This new burst of 2M pulses will then be stacked into a single pulse by the second sequence of M cavities. Therefore, the stacked pulse from the M+M multiplex contains all the energy of the input burst of $4M^2$ pulses.

As an example, it is shown in Chapter 2 that a sequence of 4 cavities with roundtrip periods equal to the oscillator can be used to stack approximately 9 pulses. Additionally in that chapter, a 4+4 multiplex is shown which can stack approximately 81 pulses. Both examples have been experimentally demonstrated by us as described in Chapter 5. These examples demonstrate that indeed very few cavities are sufficient to achieve pulse burst durations that are necessary to extract the stored energy.

Finally it is useful to note that the sum total length of the sequence of GTIs used for pulse stacking is approximately half of the total length of the pulse burst (where the length of the pulse burst is the speed of light times the burst duration). For example for stacking 81 pulses with a total burst duration of 81ns, the total cavity length is approximately 12 meters, which as described in Chapters 4 and 5 can be folded into a very compact optical arrangement.

1.5 Other Time Domain Coherent Combining Techniques

We should note here that there are two other techniques that have been developed for time domain coherent combining. These techniques are divided pulse amplification (DPA) [22] and stack and dump (SnD) [23]. The physical implementation of each of these techniques is quite different.

Divided pulse amplification is a technique that starts with a single low energy pulse, then that single pulse is split into several polarization encoded pulse replicas through a series of polarizing beam splitters, delay lines, and wave plates. After amplification the pulse replicas are recombined using a similar arrangement of polarizing beam splitters, delay lines, and wave plates. Fig. 1.5 below demonstrates the concept of DPA.

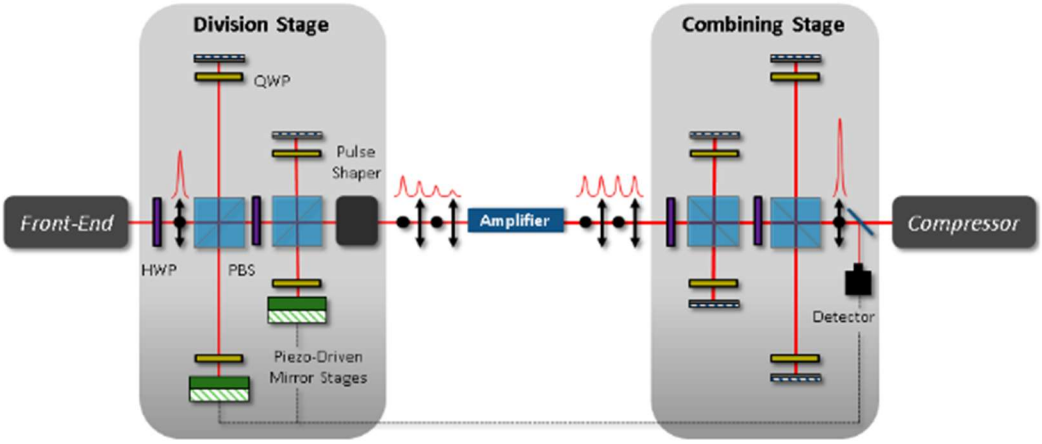

Figure 1.5: DPA setup showing the pulse replica division stages and combining stages which utilize a sequence of waveplates and polarizing beam splitters [22]

DPA in this implementation has been demonstrated with up to 4 pulse replicas, utilizing 2 delay lines. The primary limitation for scaling this method is that when going to 8 or more pulse replicas, there are not enough degrees of freedom to control the burst shape under strong amplifier saturation, unlike CPSA. Additionally, since both a splitting stage and a combining stage are required, such an arrangement is much more cumbersome compared to CPSA. Recently a modified version of DPA has been demonstrated [36], which borrowed from CPSA the concept of monolithic pulse burst formation at the beginning of the system, thus enabling all degrees of freedom required for controlling saturation and simplifying the front end. Note, however, that the only remaining principal difference between DPA and CPSA in this case is the use of linear delay lines instead of GTI interferometers. It can be easily shown that linear delay lines always require twice longer roundtrip length compared to GTI stackers, and therefore lead

to much more cumbersome stacking arrangements. Since the use of linear delay lines does not offer any interferometric alignment advantage compared to GTIs, the use of this modified DPA will provide no advantage compared to CPSA.

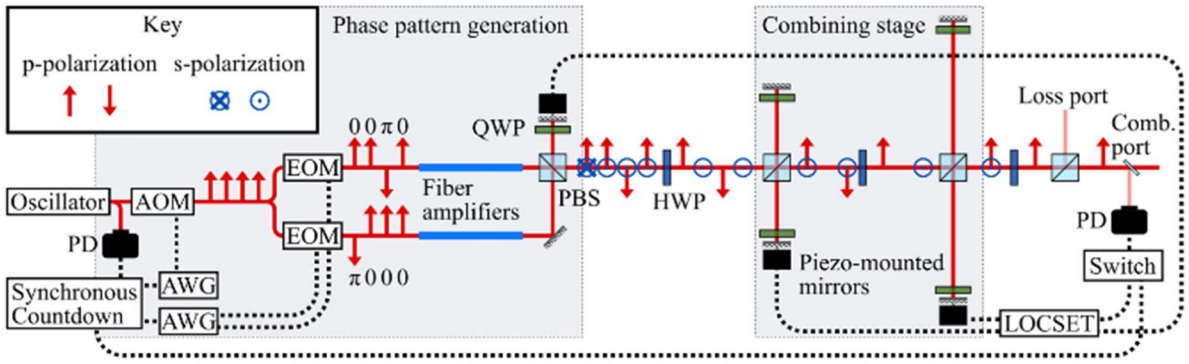

Figure 1.6: Electro-optically controlled DPA [36]

Stack and dump is a different time domain coherent combining technique that utilizes a high finesse optical cavity to build up a large intracavity pulse before switching it out as shown below in Fig. 1.7.

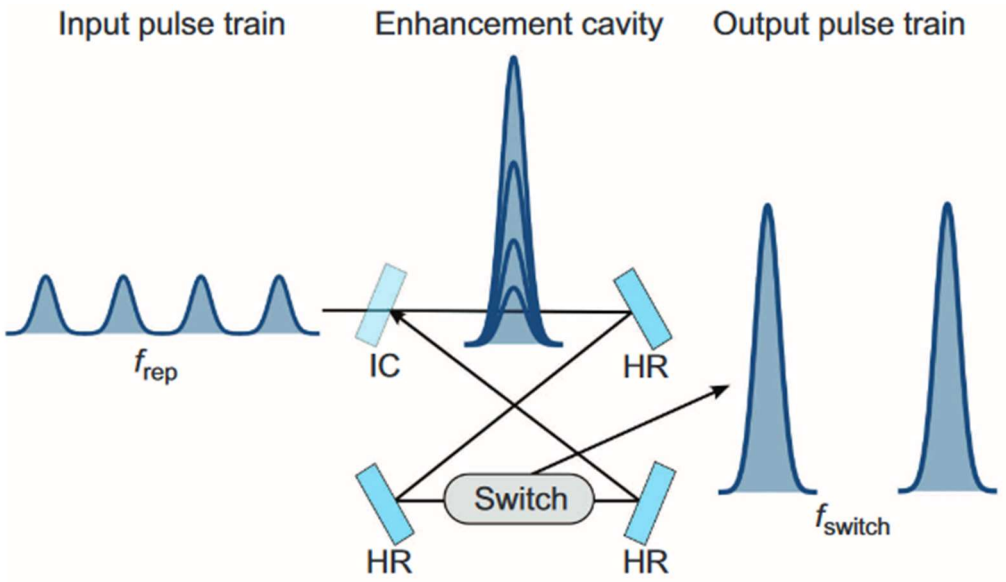

Figure 1.7: Stack and dump concept showing the buildup of a large intracavity pulse before switching it out [23]

This approach has been shown to build up an intracavity pulse that has about 60 times more energy than a single input pulse. The primary limitation of this technique is the intracavity

switch, which should be very low loss and very fast. All present implementations of stack and dump have utilized intracavity acousto-optic modulators (AOM), which will ultimately limit the maximum energy storage due to the insertion loss of the modulator as well as its finite rise time. This is due to the fact that to avoid damaging the AOM, a larger beam must be used, which will in turn reduce the AOM's switching speed. Damage of optical coatings will occur at fluences around $10J/cm^2$ for 1ns pulses [24]. So in order to achieve 10J, the beam diameter must be larger than 1cm. For a SiO_2 based AOM, this beam size will result in an AOM rise time of about 1μs, and therefore the roundtrip length of the optical cavity must be longer than 300m, which is quite challenging for a very high finesse cavity. Furthermore, insertion losses from the AOM will further limit the total number of pulses that can build up inside the cavity. A mechanical rotating optical mirror has been proposed as an all reflective optical switch for the stack and dump technique, which clearly represents a major technological hurdle, and it is unlikely that this technique could become competitive with CPSA.

Chapter 2 Analysis and Design of GTI-Based Pulse Stackers and Stackable Pulse Bursts

2.1 Introduction

As it was briefly discussed in the previous chapter, the pulse stackers used in this thesis are composed of a sequence of GTI cavities. The sequence should be designed so that it can stack a specified number of pulses with a prescribed intensity profile into a single pulse at the output. The desired burst profile in the context of high energy amplification in fibers with strong saturation is the one that minimizes the B-integral. In general, stackability of the burst is insured by applying a specific phase to each individual pulse in the burst, where the pulse phases are determined by the particular design of the stacking GTI sequence. Near complete stored energy extraction from a fiber amplifier requires long burst durations containing from ~10 to >100 pulses. However, from a practical perspective, it is desirable to accomplish this using as few cavities as possible, thus simplifying the cavity design and alignment procedure. Note that the sum total length of the cavities is fundamentally restricted to approximately half of the length of the pulse burst, which as described in section 2.5 constitutes a fundamental limit.

In general, a sequence of GTI cavities can be described by linear time invariant (LTI) system theory [26], as will be shown later in this chapter. Such an LTI system is characterized by its impulse response (i.e. its response to a single unit amplitude pulse). The system's impulse response as described in LTI theory can be calculated using a discrete-time Fourier transform or more generally a z transform [26], as described in more detail in sections 2.4 and 2.5. The impulse response for a sequence of GTIs is completely determined by the set of GTI front mirror

reflectivities, GTI cavity phases, and number of oscillator periods in each GTI. Therefore, the response of the GTI sequence to any arbitrary input can be obtained via convolution of the impulse response with the input pulse train.

An ideal sequence of pulse stackers would consist of lossless GTIs, i.e. that is GTIs with "perfect" folding mirrors which have reflectivities equal to 1 (no mirror losses). Such an ideal stacker would be completely time reversible, meaning that the time reversed (complex conjugated) impulse response incident into the stacker would produce a single output pulse. In any real stacker, the folding mirrors will have finite reflectivities less than 1, making it not strictly time reversible. However, the cavity losses are typically very small. Therefore, it is justifiable to do most of the theoretical analysis and design for ideal lossless cavities. The design of the real cavities which include finite small losses can be tweaked at the end by calculating the impulse response with the actual losses included, and then using this response to adjust the required pulse train for achieving a "perfect" stacked pulse. Furthermore, when the mirror reflectivities are not precisely the ideal calculated values (occurring due to finite precision achievable by mirror vendors), this technique of using the impulse response of the actual measured mirror reflectivities can be used to adjust the input pulse train so that it will produce "perfect" stacking for the actual set of mirrors.

Let us consider an example of a sequence of 4 lossless GTIs (each with a roundtrip period equal to that of the modelocked oscillator). This particular sequence is characterized by the following cavity mirror reflectivities $R_1 = 0.54, R_2 = 0.53, R_3 = 0.61, R_4 = 0.64$ and cavity phases (in radians) $\delta_1 = 4.66, \delta_2 = 3.15, \delta_3 = 5.46, \delta_4 = -0.01$. The blue train is the impulse response and the red train is the time reversed and complex conjugated impulse response, thus illustrating the time reversible nature of these ideal GTIs. This example illustrates that the impulse response of a

sequence of 4 cavities can be made to have 8 pulses with a controlled intensity profile (which in this example was chosen to be equal intensity). The calculation includes >20 pulses, but the all the pulses beyond the 9th have very low intensity values. Note that there are in effect about 8.6 pulses being stacked, but this is an accidental feature of this particular design. Also note that any real pulse train will have to have a finite number of pulses of the main (energy carrying) sequence plus a number of "weak" pulses at the front of the stacking burst. Such a truncation will produce some small stacked pulse "pre-pulse" error, whose magnitude and position can be controlled by choosing the length of the truncation.

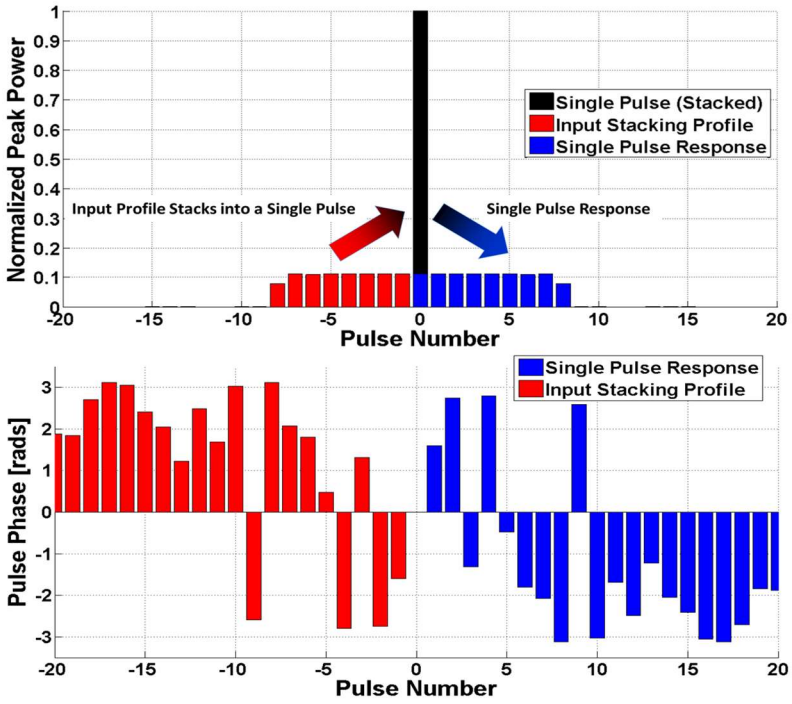

Figure 2.1: Time reversibility of the coherent pulse stacking process showing a burst of pulses with a specified phase profile being stacked into a single pulse and then that single pulse producing its impulse response. This stacking is accomplished using a sequence of 4 lossless GTIs with parameters chosen to stack a burst containing 8 equal intensity pulses. The pulse intensities are shown in the top graph and the pulse phases are shown in the bottom graph.

Since the sequence of GTIs is a linear lossless system, the amplitude spectrum of the input and output must be identical. Therefore, such a system only modifies the spectral phase of the input.

This is the necessary condition that defines a pulse burst as stackable. However, the spectral phase determines the time domain intensity profile of the stackable burst and thus must be chosen to stack the desired burst profile. It will be shown in section 2.4 how to determine the GTI parameters from such a stackable pulse burst.

This design of a sequence of GTIs for stacking equal intensity pulse bursts can be used as a building block for stacking a large number of pulses using only a few cavities. The general idea here is to do the multiplexed design on multiple different time scales using cavities containing a different number oscillator periods. The impulse response of such a design will be the convolution of the impulse responses of the different groups of cavities. There is a great variety of multiplexed configurations that exist for a specific burst intensity profile. An example of this is demonstrated in Fig. 2.6 for a 4+4 cavity multiplex for 81 pulses. It will be shown in section 2.5 that these cavities which contain more than one oscillator period can be decomposed in an equivalent sequence of cavities which contain only one oscillator period. Therefore, analyzing equal length GTI cavities is of particular fundamental importance.

Given a desired stacking pulse burst length and intensity profile, the required pulse stacker design on one hand means defining the individual GTI front mirror reflectivities, cavity phases, and number of oscillator periods in the cavities, while on the other hand it defines the individual phases of each pulse in the burst which is stackable with this particular GTI sequence. Restricting to the case of GTIs with only one oscillator period, then this design problem can be approached from two different directions. In the first approach for a desired number of pulses 2M with a prescribed intensity profile, one can find a sequence of M cavities with specified parameters that can achieve stacking of this profile. For example, it can be shown that the stacker response can be described by a system of 2M-1 higher order algebraic equations. In

principle, all of the parameters can be obtained by exact solution of the system. Note that in general such a system of equations yields more than one solution. The issue, however, is that solving this set of equations even for small M is a very difficult mathematical problem. Therefore, instead, this approach is typically accomplished using an initial Monte Carlo search over the GTI parameter space followed by a local optimization of the GTI parameters. In the second approach, we can find the stackable burst whose intensity profile is as close to the specified intensity profile as possible, and then we can extract the GTI parameters required to stack that burst from the intensities and phases of the pulses in that stackable burst. The advantage here is that this can be accomplished using an efficient phase retrieval algorithm to determine the stackable bursts followed by a local optimization of the GTI parameters. The advantage here is that one can use the vast literature on phase retrieval algorithms that allow finding solutions efficiently even for a large number of stackable pulses 2M, and stacking cavities M.

This thesis will primarily focus on using the approach of finding the best stackable burst and then extracting the GTI parameters from that burst for three reasons. The first reason is that implementing a Monte Carlo search over the GTI parameter space is quite straightforward and does not require significant explanation, except to say that a metric function (e.g. squared error between the desired burst and the stackable burst) is not a linear function of the GTI parameters, hence this type of random search is required (or potentially a more complicated nonlinear optimization routine could be applied). Indeed much of the initial designs have been obtained using the Monte Carlo search over the GTI parameter space. The second reason is that the phase retrieval algorithms used to find the stackable bursts are significantly less computationally expensive compared to Monte Carlo searches over parameter space. The third reason is that a lot

of insight can be gained by analyzing the GTI parameters that can be used to stack a specific stackable burst. In fact there are likely many potential sets of parameters that can be used, and their relationship is discussed in section 2.5.

2.2 Description of Pulse Bursts: From Continuous Time to Discrete Time

Since the coherent pulse stacking amplification technique works on real electric fields, we will start with those fields, and then make some approximations to convert the real electric fields in the continuous time domain into the more mathematically malleable form of complex electric fields in the discrete time domain. The first step is consider the form of a burst of pulses, each with the same pulse envelope and central wavelength. The form of this electric field is given in Eq. 2.1 below.

$$ {}^{in}p(t) = \sum_{n=-N}^{0} {}^{in}p_n(t) = \sum_{n=-N}^{0} {}^{in}C_n \cdot p_s(t - n \cdot \Delta T) \cdot \cos\left(\omega_0 \left(t - n \cdot \Delta T\right)\right) \tag{2.1} $$

In this equation ${}^{in}p(t)$ is the total electric field as a function of time and is comprised of N+1 pulses, with a pulse separation period of ΔT, a central frequency of ω_0, and a common pulse envelope defined by $p_s(t)$ (e.g. a Gaussian envelope). The values ${}^{in}C_n$ contain the information about the amplitude and phase of each pulse in the burst. It is valuable to first convert this expression into a complex expression, so that the analysis becomes simpler. This complex expression is given below in Eq. 2.2.

$$ {}^{in}\tilde{p}(t) = \sum_{n=-N}^{0} {}^{in}\tilde{p}_n(t) = \sum_{n=-N}^{0} {}^{in}\tilde{A}_n \cdot \tilde{p}_s(t - n \cdot \Delta T) \cdot e^{i\omega_0 (t - n \cdot \Delta T)} \tag{2.2} $$

Where in Eq. 2.2 the only thing that has appreciably changed is that ${}^{in}C_n \rightarrow {}^{in}\tilde{A}_n$, where the ~ is used to represent a complex quantity, so that the amplitudes and phases of the pulses can

be determined directly, since ${}^{in}\tilde{A}_n = \left|{}^{in}\tilde{A}_n\right| e^{i\varphi_n}$. One other small change is that the common pulse envelope is now allowed to be complex, which is just a simple generalization. Since now all of the information about the burst of pulses is contained in the ${}^{in}\tilde{A}_n$ parameters, we can work in the discrete time domain, with the time discretized by the pulse separation period ΔT. In order to separate the discrete time domain from the continuous time domain, we will also make the following notation change in order to treat the burst of pulses as a complex vector ${}^{in}\tilde{A}_n \to {}^{in}\tilde{A}[n]$, and the total burst is ${}^{in}\vec{\tilde{A}}$. This mathematical structure will be carried throughout the rest of this thesis.

2.3 Defining Stackable Bursts by Using 1D Phase Retrieval Algorithms

The first step in the design process is to determine the input pulse burst intensities and phases that can be stacked and whose intensities are closest to the designed intensity profile. Again this is accomplished by using time reversal symmetry and considering the output pulse burst that could result from a single input pulse. Mathematically we will define this impulse response as $\vec{\tilde{h}}$ and the single input pulse will be $\delta[n]$, meaning that the field is 1 at index 0 and 0 otherwise. The vector here refers to the discrete time domain (ultimately discretized by the pulse separation period), which is the framework for the majority of this analysis. Since the sequence of GTIs is linear and lossless, in the discrete Fourier domain the intensity as a function of frequency is equal before and after the GTIs (this analysis is generalizable to any linear lossless stacker). Mathematically this means $\left|\mathcal{F}\left\{\delta[n]\right\}\right|^2 = \vec{1} = \left|\mathcal{F}\left\{\vec{\tilde{h}}\right\}\right|^2$, so at all points in the frequency domain, the intensity of the impulse response in the frequency domain is equal to 1. So claiming

that a burst is stackable is equivalent to saying that the intensity of the burst in the frequency domain is equal to 1 for all frequencies.

We have now reduced the problem of finding a stackable burst to finding a burst with a designer specified intensity profile in the time domain and an algorithm specified intensity profile in the frequency domain. This is the exact situation for which phase retrieval algorithms (e.g. Gerchberg-Saxton, PhaseLift, etc.) are applicable. The Gerchberg-Saxton algorithm is an iterative phase retrieval algorithm that in our situation is used to determine the pulse phases of the impulse response in the time domain given the specified intensity profiles in the time and frequency domains [25]. Fig. 2.2 below specifies the structure of the Gerchberg-Saxton algorithm for the coherent pulse stacking amplification technique. First you start with a trial field in the time domain with phases $\vec{\varphi}_{trial}$ chosen randomly and intensities ${}^{designed}\vec{I}$ selected by the designer. Then you take the Fourier transform of that trial field, defined as ${}^{trial}\tilde{\vec{a}}$. Next you replace the amplitude of the trial field in the frequency domain $\left|{}^{trial}\tilde{\vec{a}}\right|$ with the amplitude of the target field in the frequency domain $\sqrt{{}^{target}\vec{I}} = \vec{1}$, and call the resulting expression the target field ${}^{target}\tilde{\vec{a}}$. Then you take the inverse Fourier transform of the target field in the frequency domain to obtain the target field in the time domain ${}^{target}\tilde{\vec{A}}$. Finally you replace the amplitude of the target field in the time domain with amplitude of the desired field in the time domain $\sqrt{{}^{designed}\vec{I}}$. This iterative process is repeated until the change in the target field between iterations is reduced below some specified threshold value.

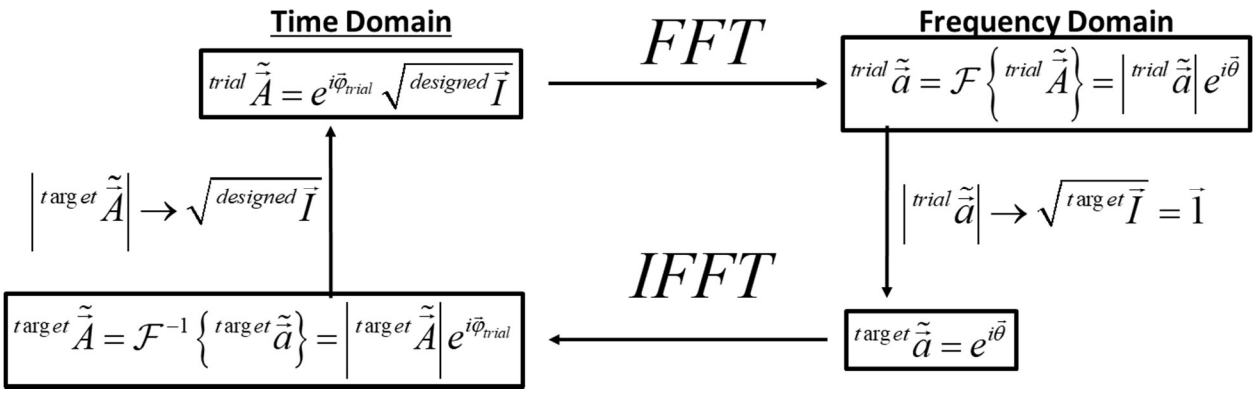

Figure 2.2: Gerchberg-Saxton Phase Retrieval Algorithm for Coherent Pulse Stacking

This phase retrieval algorithm works iteratively to determine ${}^{target}\tilde{\vec{A}}$, which is the stackable burst complex vector in the time domain. The algorithm is not guaranteed to converge to a local minimum of any metric function, so it essentially serves to determine a very good starting point for a local optimization algorithm. Further local optimization is required once the form of the pulse stackers is assumed. For instance in the case of pulse stacking using GTIs, the mirror reflectivities and cavity roundtrip lengths need to be optimized.

2.4 Determining the GTI Parameters

The next step in the design process is to determine the parameters of a sequence of GTIs that can stack the pulse burst that was found using the Gerchberg-Saxton algorithm. In order to do this, it is important to first understand how a single GTI operates in the discrete time domain. Following the formalism from Siegman [14], we denote the mirror field reflection and transmission coefficients as r and t respectively ($r = \sqrt{R}$, $t = \sqrt{1-R}$). We also define the roundtrip period of the GTI to be equal to the pulse repetition period up to a phase term, denoted as δ (henceforth called the cavity phase). Fig. 2.3 below shows a pictographic image of a GTI with the input, output, and cavity fields all defined.

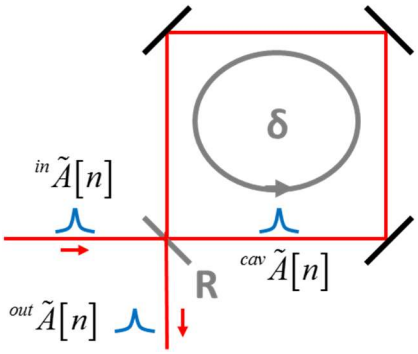

Figure 2.3: Single GTI picture with input, output, and cavity fields listed. Also shown is the mirror reflectivity (R) and cavity phase (δ)

Here we define the input field at discrete time n to be ${}^{in}\tilde{A}[n]$, the intra-cavity field at discrete time n to be ${}^{cav}\tilde{A}[n]$, and the output field at discrete time n to be ${}^{out}\tilde{A}[n]$. The relations between these fields in the discrete time domain is given below in Eq. 2.3, following the convention from Siegman [14].

$$\begin{aligned} {}^{out}\tilde{A}[n] &= {}^{in}\tilde{A}[n]r + {}^{cav}\tilde{A}[n-1]ite^{i\delta} \\ {}^{cav}\tilde{A}[n] &= {}^{in}\tilde{A}[n]it + {}^{cav}\tilde{A}[n-1]re^{i\delta} \end{aligned} \tag{2.3}$$

These equations serve as the basis for all subsequent analysis. The primary analysis tool for a set of linear difference equations, as in Eq. 2.3, is the z transform (which is essentially the discrete time version of the Laplace transform). Included below in Eq. 2.4 are the z transform properties that are required for this analysis. It should be noted that we are assuming that the fields begin at index 0, since we are concerned with finding the impulse response of the system, and the impulse is defined to be $\delta[n]$.

$$\begin{aligned} \tilde{a}(z) &= \mathcal{Z}\left\{\tilde{\tilde{A}}\right\} \equiv \sum_{n=0}^{\infty} \tilde{A}[n]z^{-n} \\ \tilde{a}(z)z^{-k} &= \sum_{n=0}^{\infty} \tilde{A}[n-k]z^{-n} \end{aligned} \tag{2.4}$$

The first equation in Eq. 2.4 is the definition of the z transform, and the second equation is the shift theorem (which can be proven quite easily). These equations allow us to re-write the difference equations from Eq. 2.3 in the z domain, which reduces them to simple algebraic equations. When re-arranged, these equations give the following result in Eq. 2.5.

$$^{out}\tilde{a}(z) = {}^{in}\tilde{a}(z) r \left[\frac{z - \frac{e^{i\delta}}{r}}{z - re^{i\delta}} \right] = {}^{in}\tilde{a}(z) T(z) \tag{2.5}$$

So in the z domain, the effect of a single GTI is to multiply the input field in the z domain by the cavity transfer function, defined as $T(z)$. Now, in order to calculate the resulting field that passes through a sequence of cavities, we need to calculate the transfer function of a sequence of cavities. In the z domain, this is trivial, since the total transfer function of the sequence is simply the product of the individual cavity transfer functions. This is written explicitly in Eq. 2.6 below.

$$^{out}\tilde{a}(z) = {}^{in}\tilde{a}(z) T_{tot}(z) = {}^{in}\tilde{a}(z) \prod_{j=1}^{M} T_j(z) = {}^{in}\tilde{a}(z) \prod_{j=1}^{M} r_j \left[\frac{z - \frac{e^{i\delta_j}}{r_j}}{z - r_j e^{i\delta_j}} \right] \tag{2.6}$$

Where here we have arbitrarily selected M total cavities, with the reflection coefficient of cavity j given by r_j and the cavity phase of cavity j given by δ_j. Now it is clear from Eq. 2.6 that for a sequence of M cavities, the transfer function in the z domain has M zeros, which are $\frac{e^{i\delta_j}}{r_j}$, and M poles, which are $r_j e^{i\delta_j}$.

The next step is to relate this information to the information we have about stackable bursts from Section 2.3. In order to do this, we need to set ${}^{out}\tilde{a}(z) = \mathcal{Z}\left\{ {}^{target}\tilde{\vec{A}} \right\}$ and ${}^{in}\tilde{a}(z) = \mathcal{Z}\{\delta[n]\} = 1$, since we know our target field in the time domain from the Gerchberg-Saxton algorithm and we defined our input field to be a unit impulse. This means that in order to determine the mirror reflectivities and cavity phases of a sequence of GTIs that will give ${}^{target}\tilde{\vec{A}}$ as the impulse response, we need to set the zeros of ${}^{out}\tilde{a}(z)$ equal to the zeros of $\mathcal{Z}\left\{ {}^{target}\tilde{\vec{A}} \right\}$, which allows ${}^{out}\tilde{a}(z)$ to approximate $\mathcal{Z}\left\{ {}^{target}\tilde{\vec{A}} \right\}$. The accuracy of this approximation increases as the length of ${}^{target}\tilde{\vec{A}}$ increases, since $\lim_{n\to 0}\left\{ {}^{target}\tilde{A}[n] \right\} \to 0$. In practice we typically choose the length of ${}^{target}\tilde{\vec{A}}$ to be twice the number of large pulses desired for the impulse response (as seen in Fig. 2.4). We also need one additional piece of information, which is that $0 < r_j < 1$, meaning that the reflectivity of each GTI front mirror is between 0 and 1. This means that the only relevant zeros of $\mathcal{Z}\left\{ {}^{target}\tilde{\vec{A}} \right\}$ are those whose magnitude is larger than 1. At this point, I should point out that $\mathcal{Z}\left\{ {}^{target}\tilde{\vec{A}} \right\}$ for a finite length ${}^{target}\tilde{\vec{A}}$ will only give poles at the origin. This is fine since from the single cavity transfer function, the zeros and poles are trivially related, meaning that we only need to find either the zeros or the poles.

Once the zeros of $\mathcal{Z}\left\{ {}^{target}\tilde{\vec{A}} \right\}$ are found and the values of r_j, δ_j, and M are determined, one further optimization step is needed. In this final step, we will locally optimize r_j and δ_j so that some measure of difference between the designed intensities and the intensities from the impulse response of the GTI sequence is minimized (e.g. sum of squared differences). The final

result will be a sequence of M GTI cavities with specified values of r_j and δ_j, along with the impulse response of that sequence of cavities (which can be simply time reversed and complex conjugated to produce a stackable burst). Fig. 2.4 below shows the flow diagram of how the full algorithm works to obtain these results.

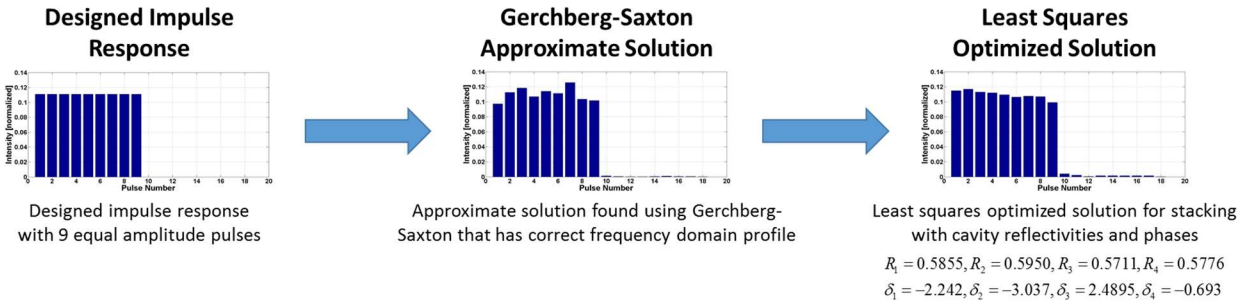

Figure 2.4: Flow diagram showing the steps to obtaining a locally optimal solution using a test case of 9 equal amplitude pulses as the impulse response, which requires 4 cavities

The scaling law for these equal length cavities is that adding an additional cavity allows us to add two additional equal amplitude pulses to the impulse response (since that additional cavity contains two degrees of freedom). So for M total cavities, the total number of "large" pulses (such as the first 9 pulses from Fig. 2.4) is given approximately by 2M. Furthermore, since M total cavities consist of M zeros in the z domain, this means that 2M pulses contain roughly M zeros in the z domain. Since it is impractical to have an experimental setup consisting of 10's or 100's of individual cavities, we must next consider using some cavities that are an integer times longer than the shortest cavity.

By using a phase retrieval algorithm to extract the approximate cavity mirror reflectivities and phases, an exponential speedup is observed compared to a Monte-Carlo search for those GTI parameters. In order to retrieve the phases for a 4M dimensional vector (as in Fig. 2.4 for M cavities), a modern phase retrieval algorithm known as PhaseLift can be shown to converge in $O\left(4M \log\left(4M\right)\right)$ calculations [35]. In order to obtain approximate cavity mirror reflectivities

and phases for M cavities using a Monte-Carlo search is expected to take $O\left(C^M\right)$ calculations (for some constant C related to the desired accuracy), which is known as the curse of dimensionality. This exponential speed improvement means that the problem of finding the cavity mirror reflectivities and phases can be solved for practically any desired impulse response function on a standard desktop computer in just a few seconds.

2.5 Multiplexing Different Length GTIs

This next section of the analysis will focus on extending the analysis from section 2.4 to include cavities that have substantially different roundtrip lengths (e.g. much larger roundtrip length difference than a single carrier wavelength). For cavities that are m times longer than the shortest cavity (where m is an integer), an extension of Eq. 2.3 can be performed, and the results are given below in Eq. 2.7.

$$\begin{aligned} {}^{out}\tilde{A}[n] &= {}^{in}\tilde{A}[n]r + {}^{cav}\tilde{A}[n-m]ite^{i\delta} \\ {}^{cav}\tilde{A}[n] &= {}^{in}\tilde{A}[n]it + {}^{cav}\tilde{A}[n-m]re^{i\delta} \end{aligned} \tag{2.7}$$

So the primary difference is that this allows the cavity to store m different cavity fields at a time, meaning in general there are m different pulses in the cavity at any time. As with the case when m=1, from section 2.4, the z transform can be used to determine the transfer function of this cavity. This transfer function is given below in Eq. 2.8.

$$T(z) = r\left[\frac{z^m - \frac{e^{i\delta}}{r}}{z^m - re^{i\delta}}\right] \tag{2.8}$$

Contrasting this result with Eq. 2.5 shows that this transfer function has m zeros, which are $\left(\frac{e^{i\delta}}{r}\right)^{1/m}$. For δ defined to be between -π and π, these zeros are all unique. Thus this single m times longer cavity with reflection coefficient r and cavity phase δ can replace a sequence of m unit length cavities with reflection coefficients all equal to $r^{1/m}$ and phases equal to $\left[\frac{\delta}{m}, \frac{(\delta+2\pi)}{m}, \cdots, \frac{(\delta+2(m-2)\pi)}{m}, \frac{(\delta+2(m-1)\pi)}{m}\right]$. A specific example illustrating this principle is given below in Fig. 2.5, which utilizes a simulation similar to Fig. 2.4, but with the reflectivities and phases slightly adjusted to show how the final two cavities can be switched out for a single cavity with the correct reflectivity and cavity phase determined by making sure the zeros of the transfer function are identical.

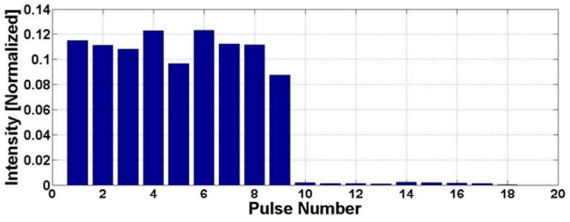

Tweaked solution for 9 pulses using 4 equal length cavities

$R_1 = 0.5855, R_2 = 0.5950, R_3 = 0.5743, R_4 = 0.5743$

$\delta_1 = -2.242, \delta_2 = -3.037, \delta_3 = 2.4486, \delta_4 = -0.693$

$m_1 = 1, \quad m_2 = 1, \quad m_3 = 1, \quad m_4 = 1$

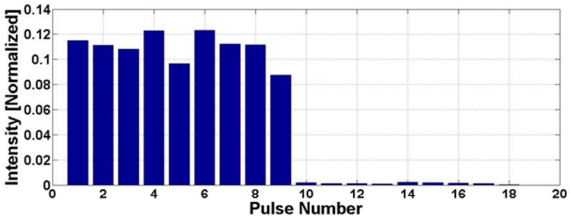

Corresponding multiplexed solution for 9 pulses using 3 unequal length cavities

$R_1 = 0.5855, R_2 = 0.5950, R_3 = 0.3299$

$\delta_1 = -2.242, \delta_2 = -3.037, \delta_3 = -1.386$

$m_1 = 1, \quad m_2 = 1, \quad m_3 = 2$

Figure 2.5: Example showing how a longer cavity can replace a sequence of shorter cavities, given that the reflectivities and phases are in the correct form. In this example, $R_3 = R_4$ and $\delta_3 = \delta_4 + \pi$, so cavities 3 and 4 from the figure on the left can be replaced by a single cavity 3 on the right, which is twice as long as cavities 1 and 2.

It is clear from Fig. 2.5 that the multiplexed solution on the right is identical to the non-multiplexed solution on the left, which must be the case since the two solutions have the same transfer function. Also comparing Fig. 2.5 with Fig. 2.4 shows that the multiplexed solution is slightly less optimal, which should be the case since the multiplexed solution has less degrees of freedom (only 3 cavities instead of 4). So ultimately, multiplexing different length cavities can

allow for less cavities overall at the cost of having less control over the impulse response profiles that are possible.

The above approach to using different length cavities works for any impulse response profile, provided the reflectivities and cavity phases have the correct form. A different approach to multiplexing when considering equal amplitude bursts of pulses has been described in sections 1.4 and 2.1. In this approach we think of having two or more sets of cavities, where the first set of cavities is taken to have unit length, and the subsequent sets of cavities are an integer times longer. Thus the impulse response from the first set of cavities is a sequence of N roughly equal amplitude pulses. Now consider a second set of cavities that are N times longer, which alone would produce a sequence of N' roughly equal amplitude pulses. Then the impulse response for the combined system of the first set of cavities followed by the second set of cavities would be NN' roughly equal amplitude pulses. This idea can be continued to an arbitrary number of sets of cavities. Fig. 2.6 below gives an example of how this idea works by considering a set of 4 cavities (identical to those in Fig. 2.4) followed by a second set of 4 cavities (same reflectivities and phases as in Fig. 2.4) that are 9 times longer than the first set.

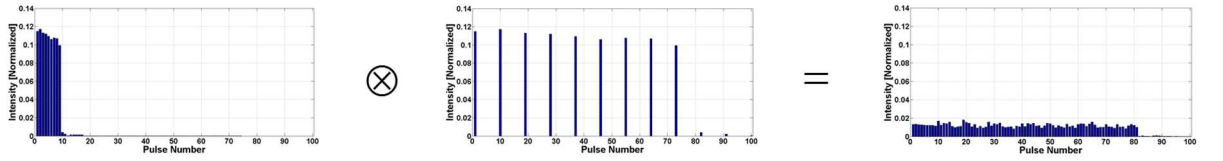

Impulse response for 4 cavities with unit length, with reflectivities and phases below

$R_1 = 0.5855, R_2 = 0.5950, R_3 = 0.5711, R_4 = 0.5776$
$\delta_1 = -2.242, \delta_2 = -3.037, \delta_3 = 2.4895, \delta_4 = -0.693$
$m_1 = 1, \quad m_2 = 1, \quad m_3 = 1, \quad m_4 = 1$

Impulse response for 4 cavities 9 times longer, with reflectivities and phases below

$R_1 = 0.5855, R_2 = 0.5950, R_3 = 0.5711, R_4 = 0.5776$
$\delta_1 = -2.242, \delta_2 = -3.037, \delta_3 = 2.4895, \delta_4 = -0.693$
$m_1 = 9, \quad m_2 = 9, \quad m_3 = 9, \quad m_4 = 9$

Impulse response for 4 cavities with unit length followed by 4 cavities 9 times longer. Total impulse response is the convolution of the individual impulse responses

Figure 2.6: (Left) Impulse response of a sequence of 4 cavities with unit length as in Fig. 2.4, (Middle) Impulse response of a sequence of 4 cavities that are 9 times longer, (Right) Impulse response of the 4 cavities with unit length followed by the 4 cavities that are 9 times longer. This impulse response is the convolution of the individual impulse responses

From Fig. 2.6, it is clear that this version of multiplexing can give an impulse response with a very long pulse train of approximately equal amplitude pulses. Further optimization of

the multiplexed reflectivities and phases can be done to achieve more desirable impulse responses, but again there is less control over the impulse response since there are fewer adjustable cavity parameters.

It is important to determine the relationship between the number and length of GTIs used and the number of pulses that such a sequence can stack in order to determine how the system complexity scales as the number of pulses in the burst increases. For a sequence of M GTIs each with a roundtrip length equal to that of the oscillator, it is clear that such a sequence contains 2M independent parameters (the front mirror reflectivities and cavity phases), therefore such a sequence can be designed to stack a burst containing approximately 2M pulses. It is also possible to use GTIs whose roundtrip period is an integer m times longer than the oscillator period. It is clear from the above analysis that these m times longer GTIs can be decomposed into an equivalent sequence of m GTIs with a roundtrip period equal to that of the oscillator. This means that for a multiplexed sequence of different length GTIs, the critical parameter that describes how many pulses such a sequence can stack is the total number of oscillator periods contained in the sequence. For example, for a sequence of cavities containing a total of q oscillator periods, a burst of approximately 2q pulses can be stacked. This leads to the scaling law that the sum total length of the sequence of GTIs used for pulse stacking is approximately (within ±1 oscillator length) half of the total length of the pulse burst (where the length of the pulse burst is the speed of light times the burst duration).

2.6 Equal Amplitude Pulse Bursts

For applications where the nonlinearity that limits energy extraction is not self-phase modulation (e.g. optical damage), the optimal impulse response design is a burst of equal

amplitude pulses. This is because a burst of equal amplitude pulses will minimize the peak power of the burst in the amplifier, thus allowing maximum energy extraction.

In addition to the examples given in Fig. 2.4 and Fig. 2.5, another example utilizing two equal length cavities is shown below in Fig. 2.7 that has an impulse response with nearly equal amplitude pulses. The choice of how many cavities to use is ultimately determined by how many pulses you want to stack and how much system complexity you can tolerate.

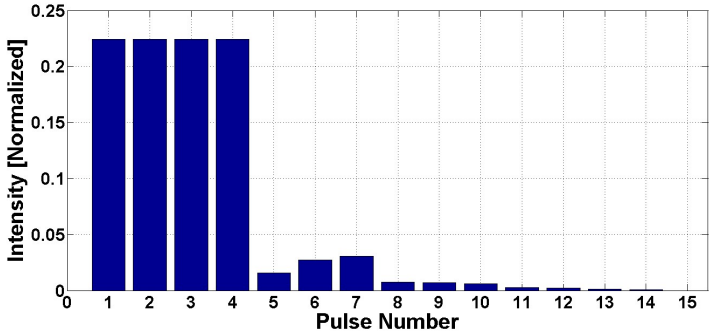

Figure 2.7: Optimized 2 cavity impulse response to create equal amplitude pulses

$$R_1 = 0.66,\ R_2 = 0.34$$
$$\delta_1 = 2.08,\ \delta_2 = 0$$
$$m_1 = 1, \qquad m_2 = 1$$

2.7 Design of Pulse Bursts with Equal Nonlinear Phase

For applications where the nonlinearity that limits energy extraction is self-phase modulation, a burst of pulses with different amplitudes may be preferred, provided that each pulse in the burst experiences the same peak nonlinear phase. It is clear that a sequence of pulses each with the same peak nonlinear phase and the same pulse envelope will have each pulse experience the same nonlinear phase as a function of time across the pulse, and this sequence will also minimize the peak nonlinear phase across the burst. The next step is to derive the burst profile required to achieve this burst of pulses with equal peak nonlinear phase.

For this analysis, we will use the Franz-Nodvic theory as it is presented in Siegman [14]. Also we will consider the burst of pulses as a single continuous pulse with the energy of the burst

of pulses equal to that of the single continuous pulse (an approximation that is valid when the pulses in the burst are sufficiently long as to be nearly overlapping). The primary formulas for this analysis are the formula for nonlinear phase due to self-phase modulation (Eq. 2.9) [12], the formula for the effective length of an amplifier in the presence of gain (Eq. 2.10) [12], and the formula for the gain as a function of time in the amplifier (Eq. 2.11) [14]. Again the goal is to find an output intensity profile that maintains an equal nonlinear phase across the pulse.

$$\phi_{NL}(t) = n_2 k_0 I_{out}(t) L_{eff}(t) \tag{2.9}$$

$$L_{eff}(t) = \frac{L}{\ln\left[G(t)\right]}\left[1 - \frac{1}{G(t)}\right] \tag{2.10}$$

$$G(t) = 1 + \left[G_0 - 1\right] e^{-\int_0^t \frac{I_{out}(t')}{U_{sat}} dt'} \approx 1 + G_0 e^{-\int_0^t \frac{I_{out}(t')}{U_{sat}} dt'} \tag{2.11}$$

Where here $\phi_{NL}(t)$ is the nonlinear phase, n_2 is the nonlinear refractive index, k_0 is the wave vector for the central frequency, $I_{out}(t)$ is the intensity profile out of the amplifier as a function of time, $L_{eff}(t)$ is the effective length of the amplifier, L is the actual length of the amplifier, $G(t)$ is the gain as a function of time, G_0 is the small signal gain of the amplifier, and U_{sat} is the saturation fluence of the amplifier. Also in Eq. 2.11, we make the approximation that $G_0 >> 1$, which is valid for most amplifiers of interest. The next step is to substitute in the formulas for $L_{eff}(t)$ and $I_{out}(t)$ (found by solving for $I_{out}(t)$ in Eq. 2.11) into Eq. 2.9, and since we want the nonlinear phase to be constant as a function of time across the pulse, we drop the time dependence on the nonlinear phase and arrive at the first order differential equation for $G(t)$ given in Eq. 2.12. The solution to this differential equation can be found analytically and

is given in Eq. 2.13 (simply make the substitution $y(t)=\ln\left[G(t)\right]$). And the final result, which is the output intensity profile as a function of time, is given in Eq. 2.14 simply by substituting Eq. 2.13 into Eq. 2.11 and solving for $I_{out}(t)$.

$$dG/dt = \frac{-\phi_{NL}}{n_2 k_0 L U_{sat}} G(t) \ln\left[G(t)\right] \tag{2.12}$$

$$G(t) = G_0^{\exp\left[\frac{-\phi_{NL}}{n_2 k_0 L U_{sat}} t\right]} \tag{2.13}$$

$$I_{out}(t) = \frac{\left\{\frac{\phi_{NL}}{n_2 k_0 L}\right\} \ln\left[G_0\right] \exp\left[\frac{-\phi_{NL}}{n_2 k_0 L U_{sat}} t\right] G_0^{\exp\left[\frac{-\phi_{NL}}{n_2 k_0 L U_{sat}} t\right]}}{G_0^{\exp\left[\frac{-\phi_{NL}}{n_2 k_0 L U_{sat}} t\right]} - 1} \tag{2.14}$$

This output intensity profile as a function of time can serve as a guide to designing the impulse response. It should be noted that the desired impulse response will be time reversed compared to Eq. 2.14. For a total burst duration τ_{burst}, the desired impulse response function is $I_{IR}(t)$ given in Eq. 2.15.

$$I_{IR}(t) = \frac{\left\{\frac{\phi_{NL}}{n_2 k_0 L}\right\} \ln\left[G_0\right] \exp\left[\frac{-\phi_{NL}}{n_2 k_0 L U_{sat}} (\tau_{burst} - t)\right] G_0^{\exp\left[\frac{-\phi_{NL}}{n_2 k_0 L U_{sat}} (\tau_{burst} - t)\right]}}{G_0^{\exp\left[\frac{-\phi_{NL}}{n_2 k_0 L U_{sat}} (\tau_{burst} - t)\right]} - 1}, \quad 0 \le t \le \tau_{burst} \tag{2.15}$$

$$I_{IR}(t) = 0, \quad t > \tau_{burst}$$

As an example, using some practical numbers for the fiber length, saturation fluence, burst duration, and nonlinear phase (the same as those in section 1.2 with the exception of the nonlinear phase), the following impulse responses can be found that correspond best to the desired impulse response.

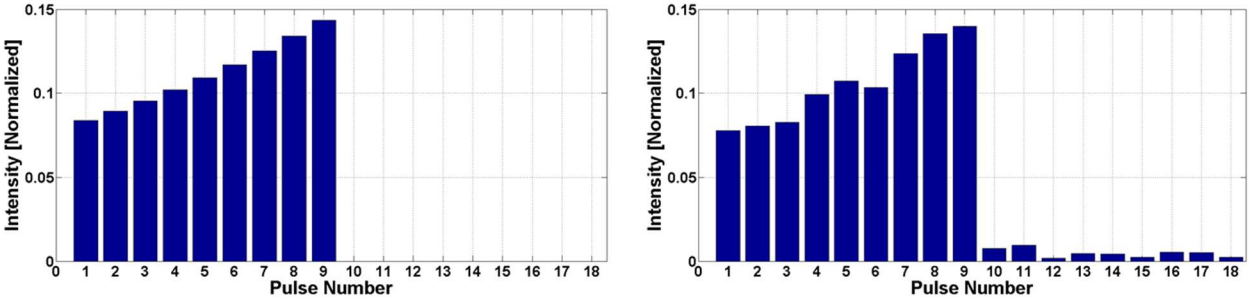

Figure 2.8: (left) Desired 9 pulse impulse response for B=10. (right) Calculated impulse response found using the algorithm from section 2.4 with the given cavity reflectivities and cavity phases below

$$R_1 = 0.53,\ R_2 = 0.58,\quad R_3 = 0.60,\quad R_4 = 0.82,\quad R_5 = 0.51$$
$$\delta_1 = 2.84,\ \delta_2 = -2.53,\ \delta_3 = -1.82,\ \delta_4 = -1.02,\ \delta_5 = 1.44$$
$$m_1 = 1,\quad m_2 = 1,\quad m_3 = 1,\quad m_4 = 1,\quad m_5 = 1$$

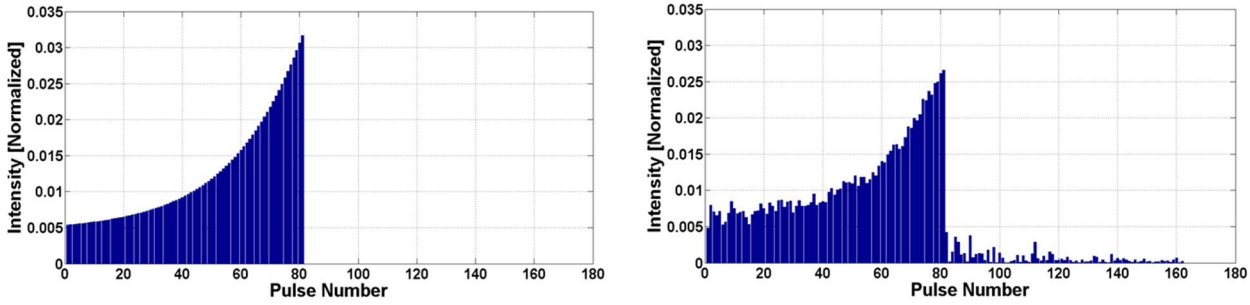

Figure 2.9: (left) Desired 81 pulse impulse response for B=5. (right) Calculated impulse response found using the algorithm from section 2.4 with the 54 cavity reflectivities and cavity phases given in the Appendix section 2.11

2.8 Stacking the Input Bursts

The next step is to analyze how the sequence of GTIs can stack these pulse bursts. Since the sequence of GTIs represents a discrete linear time invariant system, the system is completely characterized by its impulse response function. Specifically, the output resulting from an arbitrary input is given by the convolution of the input with the impulse response function as given in Eq. 2.16 [26].

$$^{out}\tilde{A}[n] = \sum_{k=0}^{n} {}^{in}\tilde{A}[k]\tilde{h}[n-k] \tag{2.16}$$

Where here $\tilde{\tilde{h}}$ is the impulse response of the sequence of GTIs, while ${}^{out}\tilde{\tilde{A}}$ and ${}^{in}\tilde{\tilde{A}}$ represent the output and input fields respectively. The index in the sum runs from 0 to n because ${}^{in}\tilde{\tilde{A}}$ starts at index 0, as does $\tilde{\tilde{h}}$.

In order to achieve pulse stacking, the input field will need to be nearly identical to the time reversed and complex conjugated impulse response. Also, since a real pulse burst has a finite number of pulses (unlike the impulse response), the output field will necessarily contain some small pre-pulses before the stacked pulse (e.g. ${}^{out}\tilde{A}[0] = {}^{in}\tilde{A}[0]\tilde{h}[0] \neq 0$). In order to minimize these pre-pulses, further optimization can be performed to adjust the input field as well as the cavity parameters.

An example is shown below in Fig. 2.10 for the 4 GTI sequence from Fig. 2.4, where the number of pulses in the burst is selected to be 9, since pulses 1 through 9 in the impulse response are more than 20 times larger than any of the subsequent pulses. The result is near perfect pulse stacking, with a pre-pulse contrast of nearly 20dB (limited by the first pre-pulse), and a stacking efficiency of nearly 99% (defined as the ratio of the stacked pulse intensity to the sum of the input pulse intensities). The stacking enhancement factor (defined as the ratio of the stacked pulse intensity to the intensity of the largest input pulse) for this profile is 8.3 times.

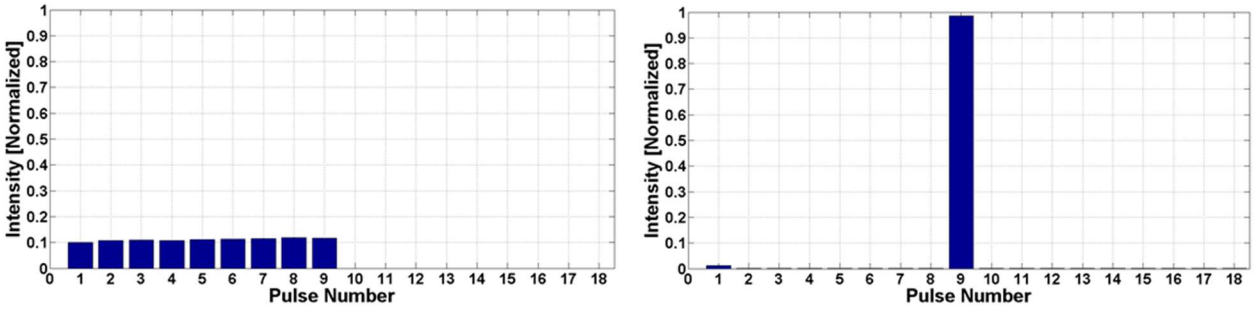

Figure 2.10: Pulse stacking of the 9 largest pulses of the impulse response from Fig. 2.4 using those same cavity parameters.

An example showing pulse stacking using the multiplexed configuration from Fig. 2.6 is show below in Fig. 2.11, where the number of pulses in this burst is selected to be 81 (since the first 81 pulses in the impulse response are much larger than the subsequent pulses). Here since the first 81 pulses of the impulse response are of nearly identical intensity, the intensities of those pulses are set to be equal in order to show that the pulse stacking is not sensitive to small changes in input pulse intensities. The result shows a pre-pulse contrast of nearly 20dB, a stacking efficiency of 96% and a stacking enhancement factor of 78.

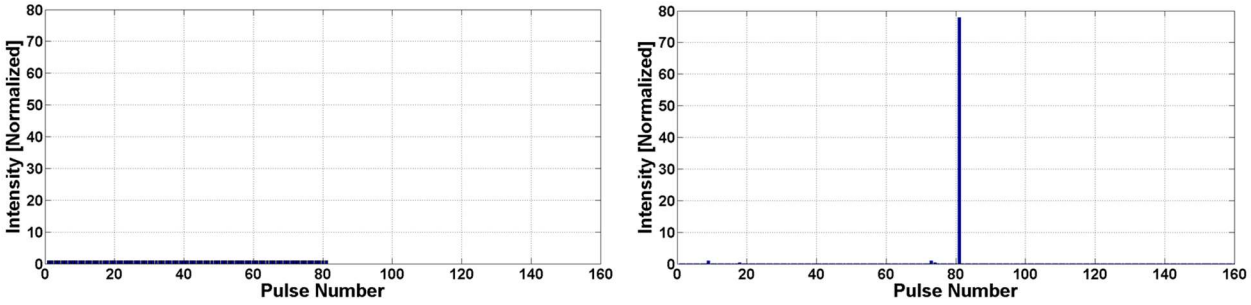

Figure 2.11: Pulse stacking of the 81 largest pulses of the impulse response from Fig. 2.6 using those same cavity parameters and with the input intensities set to be equal, thus showing the insensitivity to small changes in the input intensity profile

2.9 Pulse Stacking in the Continuous Time/Frequency Domain

Up to this point, the analysis of pulse stacking has been done primarily in the discrete time domain, which is very useful for determining the parameters for a sequence of GTIs as well as the pulse burst that can be stacked. However, since the physics that describes the operation of these GTIs is done in the continuous time domain, we need to go back to the continuous time domain to include all of the relevant physics.

In the continuous time domain, the optical pulses can be analyzed through their electric field using the carrier envelope approximation. This approximation holds for very short pulse durations, but breaks down as you approach a single cycle pulse, so all of this analysis will be relevant for ultrashort pulses where the carrier envelope approximation is still valid. In this case, we can represent the complex electric field of the burst of pulses as ${}^{in}\tilde{p}(t)$ using Eq. 2.2. Again

for now we are assuming that the envelope $\tilde{p}_s(t)$ for each pulse in the burst is identical (both in amplitude and phase). A specific situation when this assumption breaks down is for stretched ultrashort pulses when the front of the burst and the back of the burst see very different gains in the amplifier. In this case, the stretched pulses will each have different amplitude envelopes due to spectral narrowing. Also if there is self-phase modulation in this amplifier, the stretched pulses could have different phase envelopes due to each pulse in the burst acquiring a different nonlinear phase shift through the amplifier. In these extreme cases, sophisticated control algorithms should be implemented to ensure that after amplification, each pulse in the burst has the same complex envelope $\tilde{p}_s(t)$, so that the pulses only differ by their individual complex amplitudes ${}^{in}\tilde{A}_n$.

In the continuous time domain, a single GTI can be analyzed as having a transfer function in the frequency domain $T(\omega)$ given by the following formula in Eq. 2.17.

$$T(\omega) = \frac{r - \alpha e^{-i\varphi(\omega)}}{1 - r\alpha e^{-i\varphi(\omega)}} \tag{2.17}$$

Where here again r is the front mirror reflection coefficient, $\varphi(\omega)$ is the roundtrip phase as a function of frequency, and α is the roundtrip transmission coefficient for the GTI (e.g. the roundtrip power loss is $1-\alpha^2$). The reflection coefficient needs to be fixed across the frequencies of interest in order for the pulse stacking method to work optimally, and the roundtrip transmission coefficient is determined by the reflectivity of any folding mirrors in the cavity, which can have very high reflectivity across a wide spectral range. The roundtrip phase can be expanded as a Taylor series to highlight the significance of each term, which is done in Eq. 2.18.

$$\varphi(\omega) = \varphi(\omega_0) + \varphi'(\omega_0)[\omega - \omega_0] + \frac{\varphi''(\omega_0)}{2}[\omega - \omega_0]^2 + \ldots$$
$$\varphi(\omega) = \delta + \Delta T[\omega - \omega_0] + \frac{GDD}{2}[\omega - \omega_0]^2 + \ldots \quad (2.18)$$

The roundtrip phase at the carrier frequency can be identified as what has been referred to as the cavity phase $\varphi(\omega_0) = \delta$. The first derivative term is the group delay of the GTI, which must be matched to the pulse separation period, so that $\varphi'(\omega_0) = \Delta T$. The second and higher order derivative terms represent roundtrip higher order dispersion terms in the GTI (e.g. group delay dispersion, third order dispersion, fourth order dispersion, etc.). These terms should be minimized by choosing the appropriate mirrors for the GTI so that these roundtrip dispersions have a negligible impact on the pulse stacking performance.

2.10 Sensitivity of Pulse Stacking to Errors

It is important to determine the sensitivity of the pulse stacking to various errors that can arise in the system (e.g. cavity phase errors, input intensity errors, etc.). As a test bed system, we choose to use a sequence of 4 GTIs that is designed to stack a burst of 9 equal amplitude pulses. For testing the pre-pulse contrast, we use a pulse burst containing many more pulses in the tail of the impulse response, so that the pre-pulse contrast is not dominated by ${}^{out}\tilde{A}[0]$, as it is in Fig. 2.10. The critical metrics that determine how well the pulses are stacked are the peak power enhancement, pre-pulse contrast, and pulse stacking efficiency. The peak power enhancement is defined as $\eta = \frac{{}^{out}I[N]}{\max\left\{{}^{in}I[1], {}^{in}I[2], \ldots, {}^{in}I[N]\right\}}$, where ${}^{out}I[n] = \left|{}^{out}\tilde{A}[n]\right|^2$ is the intensity of the nth pulse in the output burst. The pre-pulse contrast is defined as $\chi = \frac{{}^{out}I[N]}{\max\left\{{}^{out}I[1], {}^{out}I[2], \ldots, {}^{out}I[N-1]\right\}}$, which is the intensity of the stacked pulse divided by the intensity of the largest pre-pulse. The pulse

stacking efficiency is defined as $\varepsilon = \frac{{}^{out}I[N]}{\sum_{n=1}^{N} {}^{in}I[n]}$, which is the intensity of the stacked pulse divided by the sum of the input intensities, and thus characterizes what percentage of the energy from the input burst ends up in the stacked pulse.

We simulate errors by making Gaussian random perturbations with zero mean and a specified standard deviation (σ_ϕ for the cavity phases and pulse phases and σ_I for the pulse intensities). We perturb either all the cavity phases, all the pulse phases, or all the pulse intensities using these Gaussian perturbations and then take an average over 10,000 samples of the enhancement, stacking efficiency, and pre-pulse contrast. The sensitivity of these metrics to errors is shown in Fig. 2.12 below for the test bed system with mirror reflectivities $R_1 = 0.5855,\ R_2 = 0.5950,\ R_3 = 0.5711,\ R_4 = 0.5776$ and cavity phases $\delta_1 = -2.242,\ \delta_2 = -3.037,\ \delta_3 = 2.4895,\ \delta_4 = -0.693$, with the total number of pulses in the burst chosen to be N=50.

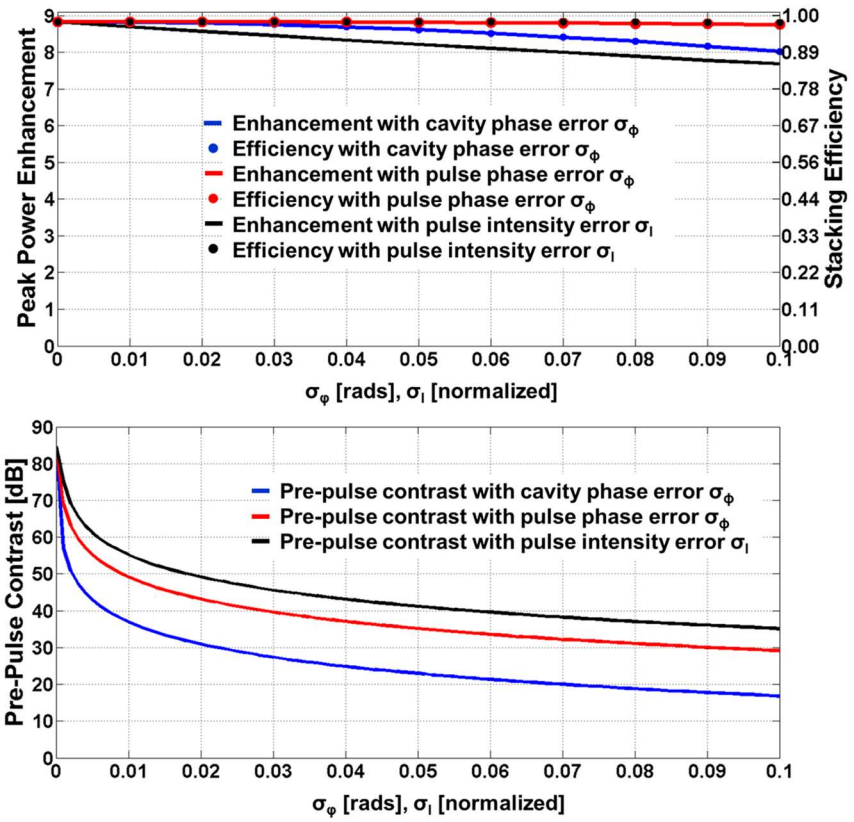

Figure 2.12: Simulations illustrating the tolerances of the coherent pulse stacking parameters for a cascade of 4 GTIs. (Top) Peak power enhancement and stacking efficiency in the presence of cavity phase errors, pulse phase errors, or pulse intensity errors. (Bottom) Pre-pulse contrast in the presence of cavity phase errors, pulse phase errors, or pulse intensity errors. Enhancement is represented by the solid lines, while efficiency is represented by the dots. Blue is for cavity phase errors, red is for pulse phase errors, and black is for pulse intensity errors. σ_φ is the standard deviation of the cavity and pulse phases in radians, while σ_I is the standard deviation in the pulse intensities as a ratio.

These simulations show that the pulse stacking is most sensitive to cavity phase errors, and that the cavity phase errors need be less than about 20mrads to achieve high fidelity pulse stacking. Another interesting feature is that the peak power enhancement is sensitive to intensity errors, while the stacking efficiency and pre-pulse contrast are not. This means that even if there are moderate intensity errors, nearly all of the input energy will end up in the stacked pulse, and thus the only concern is the peak power in the amplifier. Also it is clear that errors in mirror reflectivity will only contribute to the degradation of the enhancement since the input pulse intensity and phase profiles can always be chosen to optimize the pre-pulse contrast, thus also optimizing the stacking efficiency.

Another type of error that occurs is roundtrip loss in the GTI cavities, characterized by the roundtrip transmission coefficient α, so when $\alpha \neq 1$, the GTI has some loss (which is always the case in real experiments). The sensitivity of this same test bed system to roundtrip losses is given below in Fig. 2.13, where each GTI is assumed to have the same roundtrip loss. In addition to the 4 cavity test bed system, the loss sensitivity of the multiplexed 4+4 cavity system from Fig. 2.6 with an 81 pulse input is included.

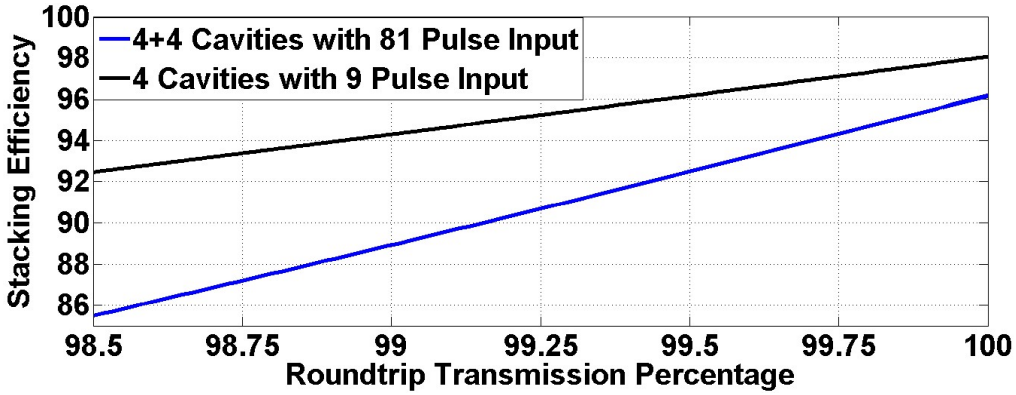

Figure 2.13: Sensitivity of the pulse stacking efficiency to roundtrip losses for both the 4 cavity case with 9 pulses and the 4+4 cavity multiplex with 81 pulses

This simulation shows that the effect of loss is linear for small losses and that very high stacking efficiencies (>95%) can be achieved with standard off the shelf mirrors with reflectivities >99.9%.

For ultrashort pulses with compressed pulse durations less than 1ps, the effect of roundtrip group delay dispersion in the GTIs as well as the effect of a carrier envelope offset frequency become important for the pulse stacking. Simulations are given below showing how these effects become more critical for shorter compressed pulse durations.

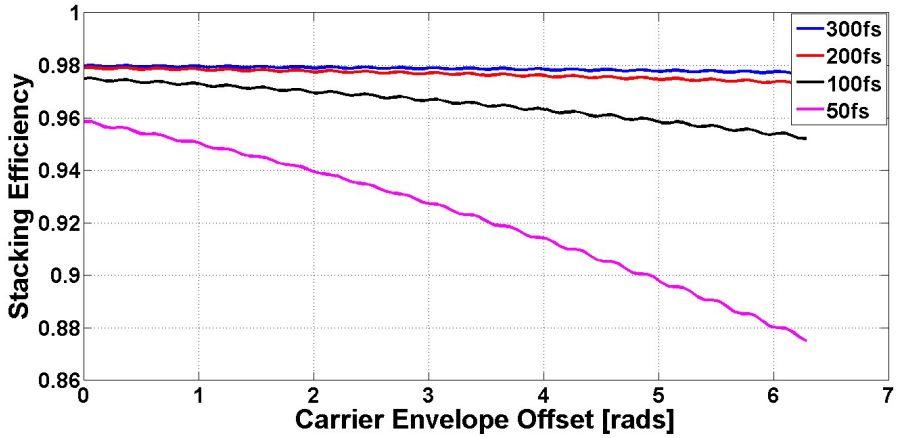

Figure 2.14: Effect of carrier envelope offset phase on the pulse stacking efficiency for the 4 cavity test case with 9 pulses

The simulation from Fig. 2.14 illustrates the effect of the carrier envelope offset (CEO) phase on the pulse stacking efficiency as the pulse duration is reduced from 300fs down to 50fs. This simulation assumes that the cavity phase is locked to the correct value, so this effect arises from the envelope of the pulse after a roundtrip not being perfectly overlapped with the envelope of the subsequent input pulse. As can be seen, this effect is effectively negligible for pulse durations longer than 200fs. As the pulse duration approaches and becomes shorter than 100fs, the carrier envelope offset becomes critical and this parameter of the laser must be actively controlled. In addition for pulse durations approaching 50fs, controlling the cavity phase by changing the roundtrip length of the cavity by a fraction of a wavelength becomes insufficient. For these very short pulse durations, the roundtrip group delay of the cavity should be controlled independently from the roundtrip phase delay of the cavity.

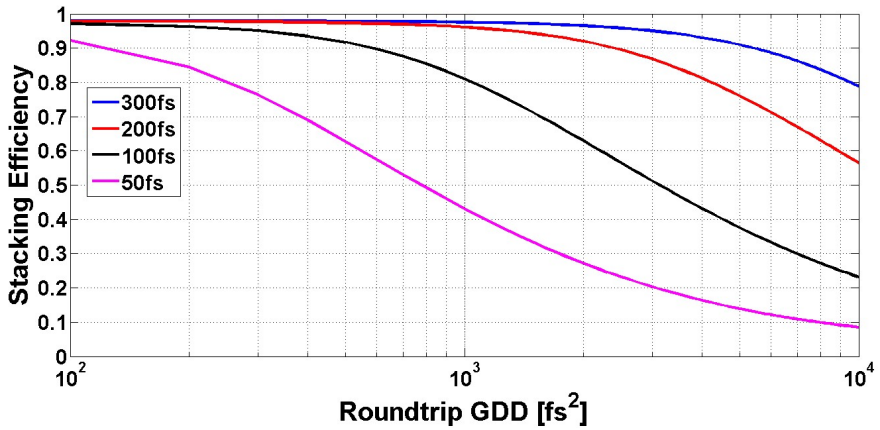

Figure 2.15: Effect of roundtrip group delay dispersion on the pulse stacking efficiency for the 4 cavity test case with 9 pulses

The simulation from Fig. 2.15 shows the effect of having a roundtrip group delay dispersion (GDD) in the cavities. This roundtrip GDD causes the pulse envelope to change upon each roundtrip of the cavity, and this envelope change will cause that pulse to not perfectly interfere with an incident pulse. For pulse durations greater than 200fs, a roundtrip GDD less than 1000fs^2 is tolerable, while for a pulse duration of 100fs, a roundtrip GDD less than 100fs^2 is required to obtain the same pulse stacking efficiency. Again for very short pulse durations approaching 50fs, the roundtrip GDD must be near 0 in order for the pulse stacking to work efficiently.

The overall message from the analysis of the effect of the carrier envelope offset phase and the roundtrip group delay dispersion is that these effects are easily managed for pulse durations longer than 200fs. For pulse durations approaching 50fs, special care must be made for both the cavities and the mode-locked oscillator to ensure that the interference of subsequent pulses is optimized.

2.11 Appendix: Reflectivities and Phases for Fig. 2.9

The cavity mirror reflectivities and cavity phases for the 54 cavities corresponding to the simulation from Fig. 2.9 are given in Table 2 and Table 3 respectively below.

Table 1: Corresponding Cavity Number

1	2	3	4	5	6	7	8	9
10	11	12	13	14	15	16	17	18
19	20	21	22	23	24	25	26	27
28	29	30	31	32	33	34	35	36
37	38	39	40	41	42	43	44	45
46	47	48	49	50	51	52	53	54

Table 2: Cavity Front Mirror Reflectivities

0.37	0.52	0.86	0.93	0.91	0.91	0.91	0.90	0.92
0.92	0.95	0.96	0.96	0.95	0.92	0.95	0.98	0.92
0.91	0.96	0.96	0.92	0.96	0.95	0.98	0.93	0.96
0.92	0.95	0.95	0.68	0.95	0.92	0.95	0.92	0.96
0.92	0.92	0.92	0.90	0.98	0.95	0.96	0.94	0.92
0.95	0.93	0.96	0.93	0.92	0.95	0.95	0.96	0.97

Table 3: Cavity Phases [rads]

2.77	-1.80	2.95	2.76	3.03	-2.86	-2.92	-3.01	-3.07
3.11	-2.77	-2.69	2.64	-2.60	2.87	2.38	-2.35	1.09
-2.19	2.19	2.09	0.86	0.94	0.66	0.49	0.35	0.26
-0.83	0.16	-2.02	-1.54	-0.70	0.09	2.00	-0.90	-0.53
0.02	-0.45	-0.26	-0.37	-1.19	-1.26	-1.93	-0.08	-0.17
-1.34	1.36	1.29	1.86	1.76	1.70	1.53	1.61	-1.73

Chapter 3 Cavity Stabilization

3.1 Introduction

Since CPSA is a time domain coherent combining technique, all the GTI pulse stacking cavities must be correctly phase stabilized with respect to the stacked output. This means that the roundtrip lengths of the Gires-Tournois interferometers (GTIs) must be kept accurate to a fraction of a wavelength in order for the pulses in the burst to interfere completely and transfer all of their energy to a single pulse. The analysis from section 2.10 showed that for the test bed system containing 4 GTIs, the roundtrip phase accuracy required was smaller than 20mrad (which is about 1/300 of a wavelength). In order to achieve such a stringent requirement in the roundtrip length of the cavities, a feedback loop is needed. The most basic requirements for a feedback loop are a metric function (which is to be maximized or minimized) and an algorithm that determines how to adjust the control variables in order to optimize the metric function. The feedback loop we chose consists of using the Stochastic Parallel Gradient Descent (SPGD) algorithm in order to optimize a peak intensity signal. The SPGD algorithm was chosen because it is essentially a model-free optimization strategy that has proven useful for coherent beam combining applications [27]. The peak intensity signal is a good choice, because when the burst of pulses are stacked into a single pulse, the peak intensity signal will be maximized.

3.2 Peak Intensity Detector for Feedback Loop

In order to stabilize the roundtrip length of the GTIs, we need a signal that is extremized when the cavity lengths are optimal for coherent pulse stacking. The signal we chose is a peak

intensity signal. Examples of peak intensity signals are a second harmonic signal (SHG) or a two photon absorption signal (TPA). Both of these signals are proportional to the square of the peak intensity, thus making them sensitive to changes in the cavity length. This is because when the cavity length is changed, the output stacking profile will change, thus changing the peak intensity seen by the detector.

A simple model for the second harmonic signal or the two photon absorption signal is as a sum of the square of the output intensities. This is because the detector integrates the squared intensity over the entire output burst. This is given explicitly by Eq. 3.1 below for the metric function denoted $J\left(\vec{\delta}\right)$, since it is a function of the cavity phases.

$$J\left(\vec{\delta}\right) = \int_{-\infty}^{\infty} {}^{out}I\left(t\right)^2 dt = \int_{-\infty}^{\infty} \left|\tilde{p}_s\left(t\right)\right|^2 dt \sum_{n=-N}^{\infty} {}^{out}I\left[n\right]^2 = \sum_{n=-N}^{\infty} {}^{out}I\left[n\right]^2 \tag{3.1}$$

In this expression, $\tilde{p}_s\left(t\right)$ represents the complex pulse envelope as in section 2.2. This complex envelope can be normalized such that $\int_{-\infty}^{\infty} \left|\tilde{p}_s\left(t\right)\right|^2 dt = 1$, which is the case in Eq. 3.1. The dependence of ${}^{out}I\left[n\right]$ on $\vec{\delta}$ is implicit here, but is obvious from Eq. 2.3 in Chapter 2.

The complete dependence of this metric function on the cavity phases is quite complicated since the dimensionality of the system grows with the number of cavities. It can be shown that this metric function is not concave as a function of the cavity phases, and as such there are local maxima to the metric function that must be accounted for.

For a specific case using two GTIs with the following reflectivities $R_1 = 0.66,\ R_2 = 0.34$ and cavity phases $\delta_1 = 2.08,\ \delta_2 = 0$, the following map of this metric signal as a function of the cavity phases can be obtained as seen in Fig. 3.1.

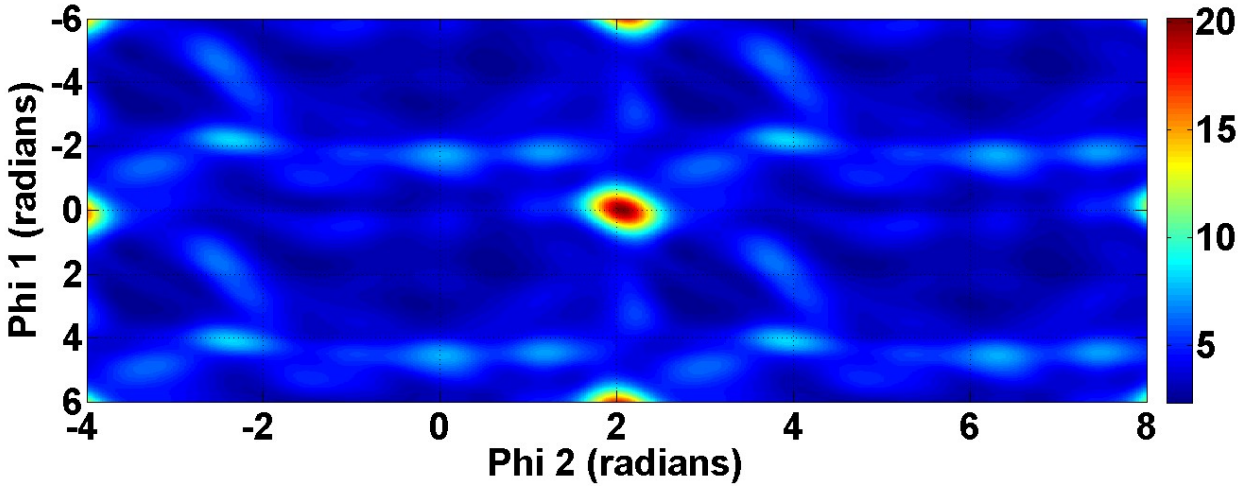

Figure 3.1: Map of SHG signal as a function of the cavity phases for the two cavity stacking scenario as in Fig. 2.7

Fig. 3.1 above illustrates some important characteristics of the landscape of this SHG or TPA signal as a function of the cavity phases. The first property is that there is a large localized peak at the ideal cavity phase values (modulo 2π). Depending on the mirror reflectivities, there may be more large peaks in the $-\pi$ to π range of the cavity phases. These other large peaks are usually the result of the mirror reflectivities being very similar in value (which is not the case for this two GTI configuration). In the degenerate case where two mirror reflectivities have exactly the same value, then the phases of those two cavities can be swapped without affecting the pulse stacking performance. Since the pulse stacking is not strongly affected by errors in the mirror reflectivity (because they essentially amount to input intensity errors as given in section 2.10), the phases from cavities with similar mirror reflectivities can be swapped with minimal negative impact on the pulse stacking (and thus also on the metric signal). Another important property of the metric function is that it contains many local maxima and saddle points (hence it is not concave). This means that before a local optimization algorithm (such as SPGD) is run, the initial cavity phase values need to be in the vicinity of the global maximum. If these initial cavity phase values are not near the global maximum, then the local optimization algorithm will fail to converge to the global maximum.

3.3 Lissajous Search for Finding Preliminary Cavity Phases

Due to the presence of undesirable local maxima in the metric function, an initial search for the approximately correct cavity phase values must be done before the SPGD algorithm can be run. This initial search is a coarse search that is intended to find the vicinity of the global maximum, so that the SPGD algorithm can simply converge to that global maximum and lock the cavity phase values to that point. We chose to do a Lissajous search for these approximately correct cavity phase values because it allows us to scan through all of the cavities at the same speed (which is not the case for a Raster scan). A Lissajous scan consists of modulating each of the cavity phases sinusoidally with a slightly different frequency. The total amount of time it takes for the Lissajous scan to return to the initial scan point is given by one divided by the greatest common factor of the scan frequencies, $T_{Lissajous} = \frac{1}{GCF\left\{\vec{f}\right\}}$.

The searching portion actually consists of doing multiple Lissajous scans since the piezo-electric transducers that control the cavity phases exhibit hysteresis. The first Lissajous scan determines the largest value of the metric function that it encountered over the course of the scan and the subsequent scan(s) repeat using the same frequencies until they find a value of the metric function that is larger than a specified tolerance (usually ~95%) of the largest value from the first scan. Once the tolerance condition is met, the Lissajous scan is stopped and the SPGD algorithm is switched on. The total scan density for the Lissajous search is determined by the frequencies used for the search, with higher frequencies with smaller greatest common factors resulting in a denser search.

3.4 Stochastic Parallel Gradient Descent Algorithm

The stochastic parallel gradient descent (SPGD) algorithm is a local optimization algorithm that seeks to "climb the hill" toward the local maximum (or minimum), and for this reason it is sometimes also referred to as a "hill climbing algorithm" [27]. The algorithm works in concept by making a small perturbation to each of the control variables, then the impact of the perturbations on the metric function is determined. If the metric function was improved by the perturbation, then the algorithm makes an adjustment to the control variables in the same direction as the perturbation; however, if the metric function was worsened, then the algorithm adjusts the control variables to move in the opposite direction. The recipe for this algorithm is given below in Fig. 3.2.

Specify "gain" g and "perturbations" ${}^{n}\Delta\vec{\delta}$

Step 1: Measure $J\left({}^{n}\vec{\delta}\right)$

Step 2: Perturb ${}^{n}\vec{\delta}$, so ${}^{n}\vec{\delta} \rightarrow {}^{n}\vec{\delta} + {}^{n}\Delta\vec{\delta}$

Step 3: Measure $J\left({}^{n}\vec{\delta} + {}^{n}\Delta\vec{\delta}\right)$

Step 4: Update $\vec{\delta}$, so ${}^{n+1}\vec{\delta} = {}^{n}\vec{\delta} + g\left[J\left({}^{n}\vec{\delta} + {}^{n}\Delta\vec{\delta}\right) - J\left({}^{n}\vec{\delta}\right)\right]{}^{n}\Delta\vec{\delta}$

Repeat Steps 1-4

Figure 3.2: Recipe for the SPGD algorithm

This recipe for the SPGD algorithm determines how to update the control variables $\vec{\delta}$ for iteration n+1 given the measurements from iteration n. It can be shown that this update formula moves on average in the direction of the gradient of J assuming the ${}^{n}\Delta\vec{\delta}$ are small independent and identically distributed (IID) random variables with zero mean and standard deviation $\Delta\delta_0$. The proof is given below in Eq. 3.2.

$$
\begin{aligned}
{}^{n+1}\vec{\delta} &= {}^{n}\vec{\delta} + g\left[J\left({}^{n}\vec{\delta} + {}^{n}\Delta\vec{\delta}\right) - J\left({}^{n}\vec{\delta}\right)\right]{}^{n}\Delta\vec{\delta} \\
J\left({}^{n}\vec{\delta} + {}^{n}\Delta\vec{\delta}\right) &\approx J\left({}^{n}\vec{\delta}\right) + \vec{\nabla}J\left({}^{n}\vec{\delta}\right)\bullet{}^{n}\Delta\vec{\delta} \\
\left\langle {}^{n+1}\vec{\delta}\right\rangle &\approx \left\langle {}^{n}\vec{\delta}\right\rangle + g\left\langle\left[\vec{\nabla}J\left({}^{n}\vec{\delta}\right)\bullet{}^{n}\Delta\vec{\delta}\right]{}^{n}\Delta\vec{\delta}\right\rangle \\
\left\langle {}^{n+1}\vec{\delta}\right\rangle &\approx \left\langle {}^{n}\vec{\delta}\right\rangle + g\vec{\nabla}J\left({}^{n}\vec{\delta}\right)\left\langle {}^{n}\Delta\vec{\delta}\bullet{}^{n}\Delta\vec{\delta}\right\rangle
\end{aligned}
\tag{3.2}
$$

This shows that for small IID perturbations, the SPGD algorithm on average takes a step in the direction of the gradient. The final step in Eq. 3.2 is possible because the perturbations are drawn from a distribution with zero mean and the perturbations for each of the control variables are independent.

3.5 SPGD Based CPSA Stabilization Performance and its Optimization

In the previous section 3.4, we showed how the SPGD algorithm works to locally optimize a function. The next step is to show how the SPGD algorithm can stabilize a system to that local optimum in the presence of noise. Furthermore, we will also determine the SPGD control parameters g and ${}^{n}\Delta\vec{\delta}$, in the presence of noise with a known magnitude, that minimize the steady state cavity phase errors.

In order to proceed, we need to make an assumption about the metric function that we are trying to stabilize. The simplest assumption is that the metric function near an optimum that we wish to stabilize to is locally parabolic. This assumption is written mathematically in Eq. 3.3.

$$
J\left({}^{n}\vec{\delta}\right) \approx J\left({}^{opt}\vec{\delta}\right) + \sum_{k=1}^{m}\frac{H_{kk}}{2}\left({}^{n}\delta_{k} - {}^{opt}\delta_{k}\right)^{2} \tag{3.3}
$$

This parabolic approximation is effectively just a Taylor series expansion of the metric function around the optimum point to second order. In this case the optimum phase values are given by

${}^{opt}\vec{\delta}$ and the second derivatives of the metric function are given by H_{kk} (which are all negative for a maximum and all positive for a minimum).

We will assume that we have a known cavity noise profile that has zero mean, a standard deviation of R_0, and no higher order moments (this is effectively an approximation that the noise magnitude is small). The cavity noise enters each time a measurement is made, and in this analysis we will assume that any measurement or system noise is negligibly small, such that the cavity noise is the dominating noise term. With these approximations on the metric function and the noise terms, Fig. 3.2 becomes Fig. 3.3 below.

Specify "gain" g and "perturbations" ${}^{n}\Delta\vec{\delta}$

Step 1: Measure $J\left({}^{n}\vec{\delta}+{}^{n}\vec{R}_1\right)$

Step 2: Perturb ${}^{n}\vec{\delta}$, so ${}^{n}\vec{\delta}\rightarrow{}^{n}\vec{\delta}+{}^{n}\Delta\vec{\delta}$

Step 3: Measure $J\left({}^{n}\vec{\delta}+{}^{n}\Delta\vec{\delta}+{}^{n}\vec{R}_1+{}^{n}\vec{R}_2\right)$

Step 4: Update $\vec{\delta}$, so ${}^{n+1}\vec{\delta}={}^{n}\vec{\delta}+{}^{n}\vec{R}_1+{}^{n}\vec{R}_2+{}^{n}\Delta\vec{\delta}\,g\sum_{k=1}^{M}\frac{H_{kk}}{2}\left[2\left({}^{n}\delta_k+{}^{n}R_{1k}-{}^{opt}\delta_k\right)\left({}^{n}\delta_k+{}^{n}R_{2k}\right)+\left({}^{n}\delta_k+{}^{n}R_{2k}\right)^2\right]$

Repeat Steps 1-4

Figure 3.3: Recipe for the SPGD algorithm in the presence of noise

So the update equation from Step 4 in Fig. 3.3 determines how the cavity phases are updated upon successive iterations of the SPGD algorithm for a parabolic metric function in the presence of cavity noise. The next step is to determine the relative magnitude of the perturbations that should be applied to each of the cavities so that the SPGD algorithm treats all of the cavities equally. This is accomplished by making a perturbation away from the optimal phase values for any of the cavities result in the same change in the metric function. The relative magnitudes of the perturbations are derived below in Eq. 3.4.

$$
\begin{aligned}
&J\left({}^{opt}\vec{\delta}+{}^{n}\Delta\delta_i\hat{i}\right)=J\left({}^{opt}\vec{\delta}+{}^{n}\Delta\delta_j\hat{j}\right)\\
&J\left({}^{n}\vec{\delta}\right)\approx J\left({}^{opt}\vec{\delta}\right)+\sum_{k=1}^{M}\frac{H_{kk}}{2}\left({}^{n}\delta_k-{}^{opt}\delta_k\right)^2\\
&H_{ii}\left({}^{n}\Delta\delta_i\right)^2=H_{jj}\left({}^{n}\Delta\delta_j\right)^2\equiv\left({}^{n}D\delta\right)^2\\
&{}^{n}\Delta\delta_i=\frac{{}^{n}D\delta}{\sqrt{|H_{ii}|}}
\end{aligned}
\tag{3.4}
$$

Now in this way, a perturbation for any cavity will result in the metric function changing by the same amount. Furthermore, although ${}^{n}D\delta$ is the same magnitude for each cavity, it is important to keep track of the cavities individually when doing the statistical analysis. For this reason, we should leave the cavity superscript on the ${}^{n}D\delta$ term to avoid confusion.

With this information in place, the next step is to look at how the mean squared error for the cavity phases evolves with successive iterations of the SPGD algorithm. Specifically we would like to derive a formula for $Err\left({}^{n}\delta_i\right)\equiv\left\langle\left({}^{n}\delta_i-{}^{opt}\delta_i\right)^2\right\rangle$, where $\langle A\rangle$ denotes the expectation value of A. With this notation, we define the following expectation values, all given below in Eq. 3.5.

$$
\begin{aligned}
&\left\langle {}^{n}D\delta_i\,{}^{m}D\delta_j\right\rangle=D\delta_0{}^{2}I_{ij}I_{nm}\\
&\left\langle {}^{n}R_{1i}\,{}^{m}R_{1j}\right\rangle=R_0{}^{2}I_{ij}I_{nm}\\
&\left\langle {}^{n}R_{2i}\,{}^{m}R_{2j}\right\rangle=R_0{}^{2}I_{ij}I_{nm}\\
&\left\langle {}^{n}R_{1i}\,{}^{m}R_{2j}\right\rangle=0
\end{aligned}
\tag{3.5}
$$

These formulas serve as the foundation for analyzing the evolution of the mean squared error. Also here I_{ij} is the identity matrix, so that it is 1 if i=j and 0 otherwise. Next we subtract ${}^{opt}\delta_i$ from both sides of the update equation from Fig. 3.3 for the ith cavity, square both sides, and then

take the expectation values. This is given below in Eq. 3.6.

$$\left\langle \left({}^{n+1}\delta_i - {}^{opt}\delta_i \right)^2 \right\rangle = \left\langle \left(\begin{array}{l} {}^{n}\delta_i - {}^{opt}\delta_i + {}^{n}R_{1i} + {}^{n}R_{2i} \\ + {}^{n}\Delta\delta_i g \sum_{k=1}^{M} \frac{H_{kk}}{2} \left[2\left({}^{n}\delta_k + {}^{n}R_{1k} - {}^{opt}\delta_k \right)\left({}^{n}\delta_k + {}^{n}R_{2k} \right) + \left({}^{n}\delta_k + {}^{n}R_{2k} \right)^2 \right] \end{array} \right)^2 \right\rangle \quad (3.6)$$

Now after multiplying out all of the terms and substituting in the relations from Eq. 3.5, we arrive at the following iterative relation for the mean squared error of the cavity phase given in Eq. 3.7.

$$Err\left({}^{n+1}\delta_i \right) = \left[\begin{array}{l} Err\left({}^{n}\delta_i \right) + \frac{g^2 D{\delta_0}^2}{\left|H_{ii}\right|} \sum_{k=1}^{M} {H_{kk}}^2 Err\left({}^{n}\delta_k \right)\left(\frac{D{\delta_0}^2}{\left|H_{kk}\right|} + {R_0}^2 \right) + \frac{2gD{\delta_0}^2 H_{ii}}{\left|H_{ii}\right|} Err\left({}^{n}\delta_i \right) \\ + \frac{g^2 D{\delta_0}^2}{\left|H_{ii}\right|} \sum_{k=1}^{M} {H_{kk}}^2 \left(\frac{2D{\delta_0}^2 {R_0}^2}{\left|H_{kk}\right|} + {R_0}^4 \right) + \frac{g^2 D{\delta_0}^2}{4\left|H_{ii}\right|} \left\{ \sum_{k=1}^{M} H_{kk} \left(\frac{D{\delta_0}^2}{\left|H_{kk}\right|} + {R_0}^2 \right) \right\}^2 \\ + \frac{4gD{\delta_0}^2 {R_0}^2 H_{ii}}{\left|H_{ii}\right|} + 2{R_0}^2 \end{array} \right] \quad (3.7)$$

The form of Eq. 3.7 is that of a linear difference equation, and combined with the equations for the mean squared error of the other cavity phases, this set of equations forms a system of linear difference equations. The general form of a system of linear difference equations is given below in Eq. 3.8.

$${}^{n+1}\vec{X} - \vec{\vec{A}} \bullet {}^{n}\vec{X} = \vec{B} \quad (3.8)$$

In this equation, ${}^{n}\vec{X}$ is the vector of state variables (e.g. cavity phases) for iteration n, while $\vec{\vec{A}}$ is a matrix that relates the vector of state variables from iteration n to those at iteration n+1, and $\vec{B}$ is a constant vector. The general solution to this type of equation is the sum of a steady state and a transient term ${}^{n}\vec{X} = \vec{X}^* + {}^{n}\vec{X}_h$. Where here $\vec{X}^*$ is the steady state term and ${}^{n}\vec{X}_h$ is the transient

term. Substituting this form of the solution into Eq. 3.8 yields the formulas for the steady state term and the transient term given in Eq. 3.9, using $\vec{\vec{I}}$ as the identity matrix.

$$\begin{aligned} \vec{X}^* &= \left(\vec{\vec{I}} - \vec{\vec{A}}\right)^{-1} \bullet \vec{B} \\ {}^n\vec{X}_h &= \vec{\vec{A}}^n \bullet {}^0\vec{X}_h \end{aligned} \tag{3.9}$$

The difficulty from this point forward is being able to derive expressions for the steady state and transient terms since this relies on being able to find a formula for the inverse of a matrix as well as a formula for a matrix raised to a power.

We will focus on solving the steady state solution, since the primary objective of this analysis was to determine the steady state error in the presence of noise. This requires us to write $\vec{\vec{A}}$ and $\vec{B}$ in terms of our SPGD parameters. This is given below in Eq. 3.10 (assuming all $H_{kk} < 0$).

$$\begin{aligned} B_i &= \frac{g^2 D\delta_0{}^2}{|H_{ii}|}\sum_{k=1}^{M} H_{kk}{}^2\left(\frac{2D\delta_0{}^2 R_0{}^2}{|H_{kk}|} + R_0{}^4\right) + \frac{g^2 D\delta_0{}^2}{4|H_{ii}|}\left\{\sum_{k=1}^{M} H_{kk}\left(\frac{D\delta_0{}^2}{|H_{kk}|} + R_0{}^2\right)\right\}^2 - 4gD\delta_0{}^2 R_0{}^2 + 2R_0{}^2 \\ A_{ij} &= \left(1 - 2gD\delta_0{}^2\right)\left\{I_{ij} + \frac{g^2 D\delta_0{}^2}{1 - 2gD\delta_0{}^2}\frac{H_{jj}{}^2}{|H_{ii}|}\left(\frac{D\delta_0{}^2}{|H_{jj}|} + R_0{}^2\right)\right\} \end{aligned} \tag{3.10}$$

This formula for A_{ij} has a special form that will allow us to find its inverse, and that is the form of a constant multiplied by the identity plus a rank 1 matrix. A formula exists for the inverse of a matrix plus a rank 1 matrix and it is given below in Eq. 3.11 [28].

$$\left(\vec{\vec{C}} + \vec{\vec{D}}\right)^{-1} = \vec{\vec{C}}^{-1} - \frac{1}{1 + Tr\left(\vec{\vec{D}}\vec{\vec{C}}^{-1}\right)}\vec{\vec{C}}^{-1}\vec{\vec{D}}\vec{\vec{C}}^{-1} \tag{3.11}$$

Where in this equation $\ddot{\vec{C}}$ is any matrix and $\ddot{\vec{D}}$ is a rank 1 matrix. So in order for us to find $\left(\ddot{\vec{I}}-\ddot{\vec{A}}\right)^{-1}$, we need to use Eq. 3.11. Fortunately for our case, the inverse of $\ddot{\vec{C}}$ can be found trivially, so finding $\left(\ddot{\vec{C}}+\ddot{\vec{D}}\right)^{-1}$ is just a matter of matrix multiplication. After substituting in all of the terms, we can arrive at a formula for the steady state mean squared error $X_i^* = Err\left(\delta_i\right)^*$ given below in Eq. 3.12.

$$X_i^* = \left\{ \begin{array}{l} \dfrac{1}{2gD\delta_0^{\,2}} \left\{ \begin{array}{l} \dfrac{g^2 D\delta_0^{\,2}}{\left|H_{ii}\right|} \displaystyle\sum_{k=1}^{M} H_{kk}^{\,2} \left(\dfrac{2D\delta_0^{\,2} R_0^{\,2}}{\left|H_{kk}\right|} + R_0^{\,4} \right) + \dfrac{g^2 D\delta_0^{\,2}}{4\left|H_{ii}\right|} \left\{ \displaystyle\sum_{k=1}^{M} H_{kk} \left(\dfrac{D\delta_0^{\,2}}{\left|H_{kk}\right|} + R_0^{\,2} \right) \right\}^2 \\ -4gD\delta_0^{\,2} R_0^{\,2} + 2R_0^{\,2} \end{array} \right\} \\ + \left(\dfrac{\dfrac{1}{4D\delta_0^{\,2}\left|H_{ii}\right|}}{1 - \dfrac{g}{2} \displaystyle\sum_{k=1}^{M} \left|H_{kk}\right| \left(\dfrac{D\delta_0^{\,2}}{\left|H_{kk}\right|} + R_0^{\,2} \right)} \right) \left[\displaystyle\sum_{j=1}^{M} \left(\dfrac{D\delta_0^{\,2}}{\left|H_{kk}\right|} + R_0^{\,2} \right) \left[\begin{array}{l} \left|H_{jj}\right| g^2 D\delta_0^{\,2} \displaystyle\sum_{k=1}^{M} H_{kk}^{\,2} \left(\dfrac{2D\delta_0^{\,2} R_0^{\,2}}{\left|H_{kk}\right|} + R_0^{\,4} \right) \\ + \dfrac{\left|H_{jj}\right| g^2 D\delta_0^{\,2}}{4} \left\{ \displaystyle\sum_{k=1}^{M} H_{kk} \left(\dfrac{D\delta_0^{\,2}}{\left|H_{kk}\right|} + R_0^{\,2} \right) \right\}^2 \\ -4gD\delta_0^{\,2} R_0^{\,2} H_{jj}^{\,2} + 2R_0^{\,2} H_{jj}^{\,2} \end{array} \right] \right] \end{array} \right\} \quad (3.12)$$

This formula contains the majority of the information needed to optimize the SPGD parameters g and $D\delta_0$. Determination of these optimal parameters requires defining a metric function to optimize, and an obvious choice is the metric function used in the SPGD algorithm $J\left(\vec{\delta}\right)$. Using Eq. 3.4, it is clear that under the parabolic approximation the average value of $J\left(\vec{\delta}\right)$ is linearly related to $Err\left(\vec{\delta}\right)$, and this is given explicitly below in Eq. 3.13.

$$
\begin{aligned}
J\left({}^{n}\vec{\delta}\right) &\approx J\left({}^{opt}\vec{\delta}\right)+\sum_{k=1}^{M}\frac{H_{kk}}{2}\left({}^{n}\delta_k-{}^{opt}\delta_k\right)^2 \\
\left\langle J\left({}^{n}\vec{\delta}\right)\right\rangle &\approx \left\langle J\left({}^{opt}\vec{\delta}\right)\right\rangle+\sum_{k=1}^{M}\frac{H_{kk}}{2}\left\langle\left({}^{n}\delta_k-{}^{opt}\delta_k\right)^2\right\rangle \\
\left\langle J\left({}^{n}\vec{\delta}\right)\right\rangle &\approx \left\langle J\left({}^{opt}\vec{\delta}\right)\right\rangle+\sum_{k=1}^{M}\frac{H_{kk}}{2}Err\left({}^{n}\delta_k\right)
\end{aligned}
\tag{3.13}
$$

By using Eq. 3.12, the optimal values of g and $D\delta_0$ can be found numerically that optimize $J\left(\vec{\delta}\right)$. Before optimization, it is also useful to look at Eq. 3.12 to see that it does contain a singularity for specific values of $g, D\delta_0, R_0,$ and H_{kk}. This singularity occurs when the following relation holds in Eq. 3.14.

$$
\frac{g}{2}\sum_{k=1}^{M}\left|H_{kk}\right|\left(\frac{D\delta_0{}^2}{\left|H_{kk}\right|}+R_0{}^2\right)=1 \tag{3.14}
$$

As the term on the left hand side of Eq. 3.14 gets larger and approaches 1, the SPGD algorithm approaches the singularity and prediction of the steady state mean squared error becomes less reliable (since the metric function $J\left(\vec{\delta}\right)$ will in general contain higher order terms than those included in the parabolic approximation). When the term on the left hand side of Eq. 3.14 is equal to or greater than 1, all predictive power is lost since the algorithm will be operating in an unstable regime.

Although in general a numerical solution is required to find the optimal values of g and $D\delta_0$, in the situation where all of the second derivatives are equal (i.e. $H_{kk}=\bar{H}$ for all k), an analytical solution can be derived for g and $D\delta_0$. In this situation, Eq. 3.12 can be simplified to Eq. 3.15 below.

$$X_i^* = \left\{ \begin{array}{l} \dfrac{1}{2gD\delta_0^{\,2}} \left\{ \begin{array}{l} \dfrac{g^2 D\delta_0^{\,2}}{|\bar{H}|} \bar{H}^2 M \left(\dfrac{2D\delta_0^{\,2} R_0^{\,2}}{|\bar{H}|} + R_0^{\,4} \right) + \dfrac{g^2 D\delta_0^{\,2}}{4|\bar{H}|} \bar{H}^2 M^2 \left(\dfrac{D\delta_0^{\,2}}{|\bar{H}|} + R_0^{\,2} \right)^2 \\ -4gD\delta_0^{\,2} R_0^{\,2} + 2R_0^{\,2} \end{array} \right\} \\ + \left(\dfrac{\dfrac{1}{4D\delta_0^{\,2}|\bar{H}|}}{1 - \dfrac{g}{2}|\bar{H}| M \left(\dfrac{D\delta_0^{\,2}}{|\bar{H}|} + R_0^{\,2} \right)} \right) \left[M \left(\dfrac{D\delta_0^{\,2}}{|\bar{H}|} + R_0^{\,2} \right) \left[\begin{array}{l} |\bar{H}|^3 g^2 D\delta_0^{\,2} M \left(\dfrac{2D\delta_0^{\,2} R_0^{\,2}}{|\bar{H}|} + R_0^{\,4} \right) \\ + \dfrac{|\bar{H}|^3 g^2 D\delta_0^{\,2}}{4} M^2 \left(\dfrac{D\delta_0^{\,2}}{|\bar{H}|} + R_0^{\,2} \right)^2 \\ -4gD\delta_0^{\,2} R_0^{\,2} \bar{H}^2 + 2R_0^{\,2} \bar{H}^2 \end{array} \right] \right] \end{array} \right\} \tag{3.15}$$

From Eq. 3.15, the optimal values for g and $D\delta_0$ can be numerically solved. Then an approximately optimal value for $D\delta_0$ can be found by fitting the numerical results. This fit value for $D\delta_0$ can then be plugged into Eq. 3.15, and that equation can be analytically optimized for g by setting $\dfrac{\partial X_i^*}{\partial g} = 0$. Finally the approximately optimal values for g and $D\delta_0$ can be plugged back into Eq. 3.15 to yield an estimate of the steady state error (which can be simplified by assuming M is large). All of these optimized values are given below in Eq. 3.16.

$$\begin{aligned} & D\delta_{0\ optimal} \approx 2R_0 \sqrt{|\bar{H}|} \\ & g_{optimal} \approx \frac{5M - \sqrt{\left(M\left[75M - 8 \right] \right)}}{M\bar{H}R_0^{\,2}\left(25M - 4 \right)} \approx \frac{-0.15}{M\bar{H}R_0^{\,2}} \\ & Err\left(\delta_i \right)^*_{\ optimal} \approx 3.42MR_0^{\,2} \\ & \left\langle J\left(\vec{\delta} \right) \right\rangle^* \approx J\left({}^{opt}\vec{\delta} \right) - 1.71|\bar{H}| M^2 R_0^{\,2} \end{aligned} \tag{3.16}$$

These formulas from Eq. 3.16 provide important insight into how the steady state errors scale with the number of cavities and with the noise magnitude. The formulas also show that the

steady state error $Err\left(\delta_i\right)^*_{optimal}$ is not dependent on the metric function chosen for the optimization, since it is only a function of the number of cavities and the noise magnitude.

Furthermore, in order to utilize SPGD in practice, typically the update equation from Step 4 of Fig. 3.2 is normalized with respect to the metric function so that ${}^{n+1}\vec{\delta} = {}^{n}\vec{\delta} + g\frac{J\left({}^{opt}\vec{\delta}\right)}{J\left({}^{n}\vec{\delta}\right)}\left[J\left({}^{n}\vec{\delta} + {}^{n}\Delta\vec{\delta}\right) - J\left({}^{n}\vec{\delta}\right)\right]{}^{n}\Delta\vec{\delta}$. In this case, all of the preceding equations hold to lowest order and $J\left({}^{opt}\vec{\delta}\right)$ is the value that is calculated during simulation. This allows all of the formulas from Eq. 3.16 to be used simply from the simulated values, since the update equation is now scaled correctly.

To illustrate the effectiveness of this analysis, the formulas were compared to simulations using the SPGD algorithm for cavity stabilization. The first simulation uses a constant g and $D\delta_0$ to show how the cavity steady state error and the metric function (SHG signal) change as the noise magnitude is increased in the case of 4 cavity stacking as in Fig. 2.3. These are shown below in Fig. 3.4 and includes the location of the singularity around 0.0145 radians. This figure shows the accuracy of the formula for small noise values, as well as that the parabolic approximation breaks down for noise values approaching the singularity (greater than about 0.01 radians), and how the steady state noise becomes unpredictable beyond the singularity.

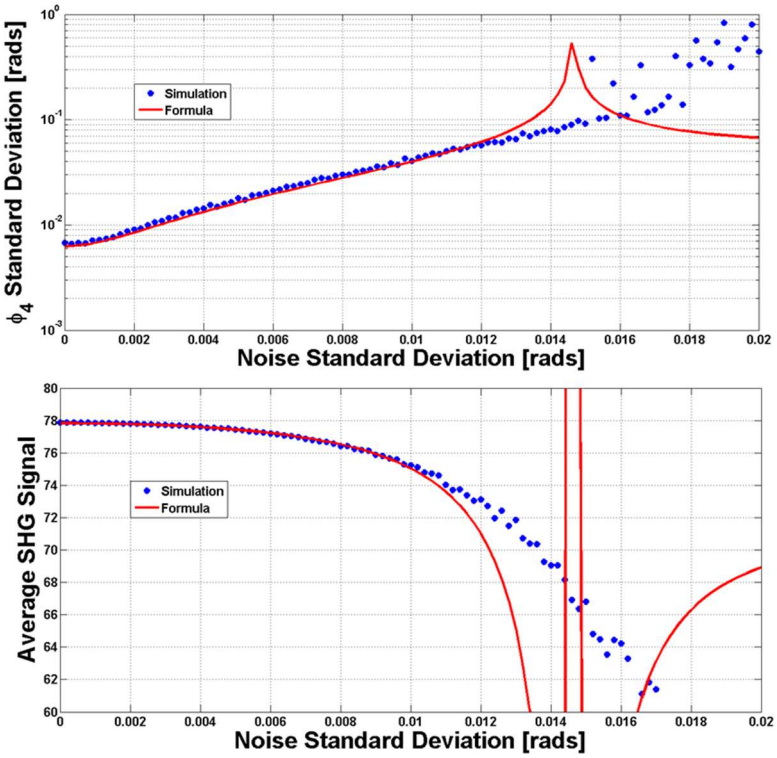

Figure 3.4: (top) Cavity phase error for cavity 4 using the SPGD algorithm with non-optimal parameters. (bottom) Average SHG signal for the case of 4 cavity stacking in the presence of noise with non-optimal SPGD parameters

The next simulation now uses the optimized values for g and $D\delta_0$ from Eq. 3.16 as the noise magnitude is increased and is shown below in Fig. 3.5. This simulation again shows very good agreement of the calculated formula values compared with the simulated values as well as how the parabolic approximation breaks down for noise values beyond about 0.025 radians. This is now a property of the specific metric function used (rather than a property of the SPGD algorithm).

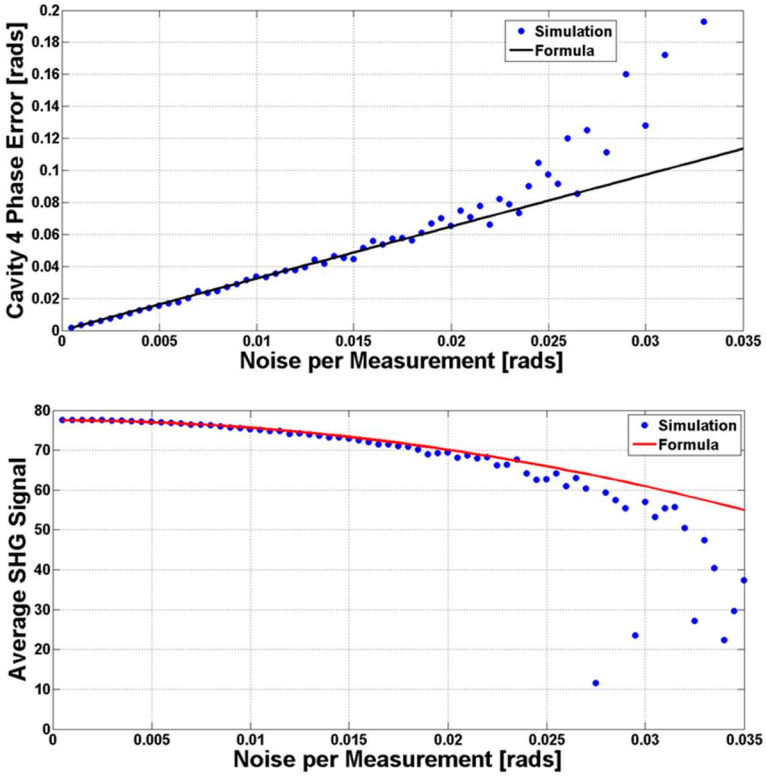

Figure 3.5: (top) Cavity phase error for cavity 4 using the SPGD algorithm with optimal parameters. (bottom) Average SHG signal for the case of 4 cavity stacking in the presence of noise with optimal SPGD parameters

3.6 Conclusions of SPGD

Given the analysis presented in section 3.5, all of the necessary SPGD parameters can be determined from the known metric function. This analysis also gives the performance of the SPGD algorithm in terms of the steady state error as a function of the noise per measurement in the system. This information can be used to obtain arbitrary stability by combining this analysis with a measurement of the noise magnitude at various loop speeds in order to determine how fast the feedback loop needs to be in order to achieve the prescribed stability.

Chapter 4 GTI-Based Pulse Stacking Arrangements

4.1 Introduction

When considering interferometer designs for the GTI pulse stackers, there are three primary considerations; those are the sensitivity of the interferometers to perturbations, the energy/power handling of the design, and the total size of the pulse stacking layout. This chapter will first introduce some general considerations on interferometer stability, then it will discuss specific GTI designs based on flat mirror cavities as well as Herriott cell folded cavities, and finally conclusions will be presented giving some basic guidelines on which interferometer design to use based on the energy handling and compactness requirements. This chapter will also make use of much of the results from Chapter 2 on general GTI pulse stacking theory.

Since the goal of the GTI pulse stackers is to transfer nearly all of the energy from a burst of pulses into a single pulse, care must be taken to ensure that the interference of the spatial beams is sufficient to produce a high fidelity pulse stacking result. This can be accomplished using many different GTI cavity configurations; however, we will focus on only two cavity configurations that have advantageous properties for coherent pulse stacking. The first configuration is a travelling wave cavity containing only flat optical mirrors. This flat mirror cavity is best for short or medium length cavities and the interference properties as well as the energy/power handling will get better as the beam size increases (need the Rayleigh range of the beam to be much larger than the cavity length). The second configuration is a travelling wave cavity containing a Herriott cell, which acts as an optical relay with unit magnification. This

Herriott cavity is primarily useful for long cavities, since long optical distances can be folded into a very compact arrangement (good when the Rayleigh range of the beam is comparable to the total cavity length), but the energy/power handling does not scale as well as the flat mirror cavities.

4.2 General Considerations of Interferometer Stability

Before looking at specific cavity arrangements, it is important to introduce the general types of errors that can occur in optical cavities and analyze the impact of these errors in the simple case of two beam interference, since that is the type of interference that occurs at the partial reflector interface. The most basic type of error that can occur in an optical cavity is a tip/tilt error of one of the cavity mirrors. This basic error gives rise to multitude of issues that will limit or degrade interference, and these will be discussed in more detail in subsequent paragraphs. Another type of error that can occur in an optical cavity is a beam size error related to imperfect mode matching with the cavity. An imperfect mode matching will result in the beam not being perfectly spatially overlapped after a roundtrip through the cavity, which will degrade the interference quality. For all errors considered, only the lowest order Taylor expansion will be taken, implying that these are small errors.

The first error to be analyzed as a result of a tip/tilt error in one of the cavity mirrors is a roundtrip phase error that results from the pivot of the mirror mount not being located at the center of the mirror (where the beam presumably hits). Fig. 4.1 below shows a schematic of a commercially available Thorlabs Polaris series mirror mount (similar to those used in the experiments in Chapter 5) with the vertical distance from the pivot to the center of the mirror denoted as y_p.

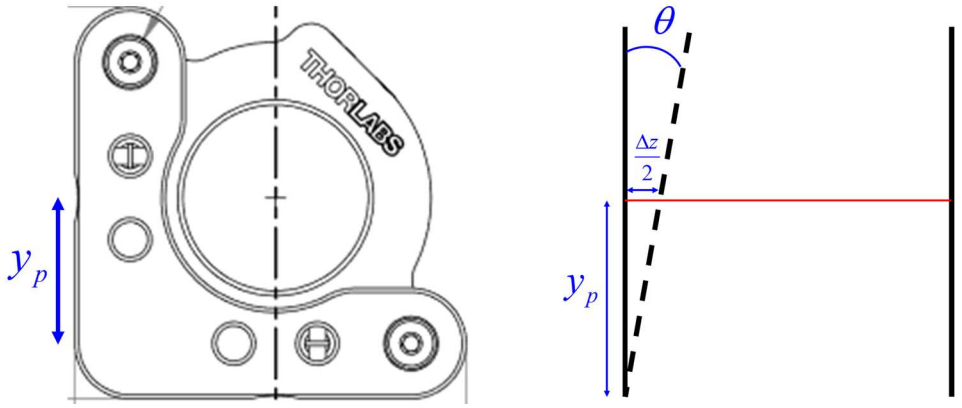

Figure 4.1: (left) Thorlabs Polaris mirror mount with vertical distance to pivot labelled. (right) Two mirror interferometer showing the piston error of a mirror rotation by angle θ about the pivot.

If this mirror rotates about its vertical pivot by an angle θ, that will cause the roundtrip optical path of the simple interferometer from Fig. 4.1 to change by an amount $\Delta z \approx 2 y_p \theta$ for small angles due to the resulting piston error. The resultant roundtrip phase change is then given by $\Delta\delta = k_0 \Delta z \approx \frac{4\pi y_p \theta}{\lambda}$. As a quick check on the requirement for the mirror tip/tilt angle, we can plug in some standard numbers such as $y_p \approx 1cm$, $\lambda \approx 1\mu m$ along with a phase tolerance from section 2.10 of $\Delta\delta \approx 0.02$ to see that the tolerance on the tip/tilt angle is $\theta \leq 0.1 \mu rads$.

Another roundtrip phase error that can result from the tip/tilt error is due to the total roundtrip path length changing because the beam now follows a different trajectory. This effect is illustrated below in Fig. 4.2.

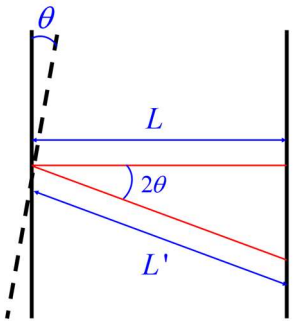

Figure 4.2: Two mirror interferometer showing the path length error due to the beam following a different trajectory

The change in the roundtrip optical path between the two mirrors can be examined by looking at the difference $\frac{\Delta z}{2} \approx L' - L \approx L\theta^2$. The resultant roundtrip phase error is again $\Delta\delta = k_0 \Delta z \approx \frac{4\pi L\theta^2}{\lambda}$. Again plugging in some approximate numbers such as $L \approx 1m$, $\lambda \approx 1\mu m$, and $\Delta\delta \approx 0.02$ yields an angular requirement of $\theta \leq 40\mu rads$. This error due to the different beam trajectories is much less sensitive than the error due to the pivot point not being in the center of the mirror, and as such can typically be neglected.

At this point it is important to quantify the effect of a phase error on the quality of interference between two optical beams. Consider the situation below in Fig. 4.3 which shows two beams being combined at a partially reflecting mirror with a reflectivity of R=0.5. By using the analysis of the partial reflector as a 4 port device as is done in Siegman [14], the output electric fields can be specified as a function of the input electric fields. This analysis is similar to that given from Eq. 2.3.

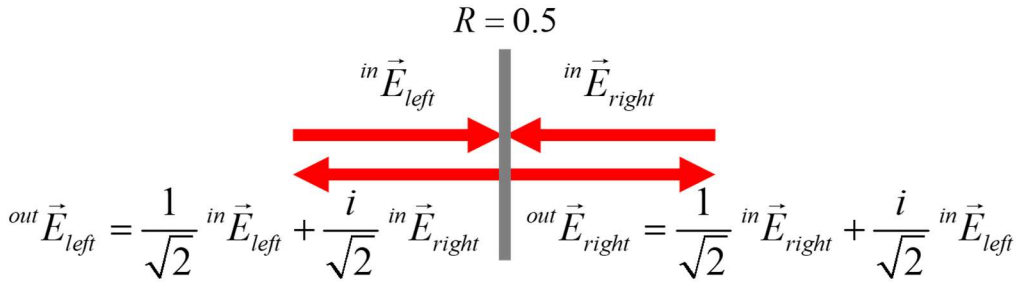

Figure 4.3: R=0.5 partially reflecting mirror as a 4 port device with electric fields specified

With this toy configuration, it is possible to analyze the effect of various small errors on the interference of two optical beams. The first thing to notice is that in order to achieve perfectly constructive interference for ${}^{out}\vec{E}_{right}$, you must have ${}^{in}\vec{E}_{right} = i\,{}^{in}\vec{E}_{left}$ and any deviation from that will result in imperfect interference. The previous paragraphs of this section have analyzed the effect mirror tip/tilt errors on the relative phase between the two beams, so if we assume a phase error of $\Delta\delta$, then we will have ${}^{in}\vec{E}_{right} = i\,{}^{in}\vec{E}_{left}e^{i\Delta\delta}$. Now what we really want to know is what fraction of the input power is combined to form the output beam propagating to the right, and in order to do this, we must make some assumptions on the beam profile. For this we will assume a Gaussian beam profile with a beam radius of w_0 so that ${}^{in}\vec{E}_{left} = \hat{x}E_0 e^{-\frac{\left(x^2+y^2\right)}{w_0^2}} e^{-ikz}$ and ${}^{in}\vec{B}_{left} = \hat{y}\frac{E_0}{c} e^{-\frac{\left(x^2+y^2\right)}{w_0^2}} e^{-ikz}$, and that the location of the partially reflecting mirror is $z = 0$ (which is where the interference takes place). Then it can be shown that the total average power in such a beam is:

$$
\begin{aligned}
{}^{in}P_{left} &= \frac{1}{2\mu_0}\mathbb{R}\left\{\int_{-\infty}^{\infty}\int_{-\infty}^{\infty} dxdy\left({}^{in}\vec{E}_{left}(x,y)\times {}^{in}\vec{B}^{*}_{left}(x,y)\right)\cdot\hat{z}\right\} \\
{}^{in}P_{left} &= \frac{1}{2c\mu_0}\mathbb{R}\left\{\int_{-\infty}^{\infty}\int_{-\infty}^{\infty} dxdy\left({}^{in}\vec{E}_{left}(x,y)\times\hat{z}\times {}^{in}\vec{E}^{*}_{left}(x,y)\right)\cdot\hat{z}\right\} \\
{}^{in}P_{left} &= \frac{{E_0}^2}{2c\mu_0}\int_{-\infty}^{\infty}\int_{-\infty}^{\infty} dxdy e^{-\frac{2\left(x^2+y^2\right)}{{w_0}^2}} = \left(\frac{{E_0}^2}{2c\mu_0}\right)\frac{\pi {w_0}^2}{2}
\end{aligned}
\tag{4.1}
$$

Now then it is clear that the total power of all the input beams is ${}^{in}P_{tot} = {}^{in}P_{left} + {}^{in}P_{right} = \left(\frac{{E_0}^2}{2c\mu_0}\right)\pi {w_0}^2$. And if we still assume ${}^{in}\vec{E}_{right} = i\,{}^{in}\vec{E}_{left}e^{i\Delta\delta}$, then the output power to the right along with the beam combining efficiency can be calculated from Eq. 4.2 below.

$$
\begin{aligned}
{}^{out}P_{right} &= \frac{1}{2\mu_0}\mathbb{R}\left\{\int_{-\infty}^{\infty}\int_{-\infty}^{\infty} dxdy\left({}^{out}\vec{E}_{right}(x,y)\times {}^{out}\vec{B}^{*}_{right}(x,y)\right)\cdot\hat{z}\right\} \\
{}^{out}P_{right} &= \frac{1}{2c\mu_0}\mathbb{R}\left\{\int_{-\infty}^{\infty}\int_{-\infty}^{\infty} dxdy\left({}^{in}\vec{E}_{left}(x,y)\times\hat{z}\times {}^{in}E^{*}{}_{left}(x,y)\right)\cdot\hat{z}\left[\frac{1+e^{i\Delta\delta}}{\sqrt{2}}\right]\left[\frac{1+e^{-i\Delta\delta}}{\sqrt{2}}\right]\right\} \\
{}^{out}P_{right} &= \left(\frac{{E_0}^2}{2c\mu_0}\right)\frac{\pi {w_0}^2}{2}\left[1+\cos(\Delta\delta)\right] \approx \left(\frac{{E_0}^2}{2c\mu_0}\right)\frac{\pi {w_0}^2}{2}\left[2-\frac{\Delta\delta^2}{2}\right] \\
\eta_{bc} &= \frac{{}^{out}P_{right}}{{}^{in}P_{tot}} \approx 1-\frac{\Delta\delta^2}{4}
\end{aligned}
\tag{4.2}
$$

This formula for the combined output power is given assuming a small phase error and this formula can be useful since it allows us to relate known cavity phase error tolerances to the tolerances in other parameters through this beam combining efficiency η_{bc}. While other types of combining errors will not manifest themselves in exactly the same manner as cavity phase errors with regards to coherent pulse stacking amplification, this type of back of the envelope calculation can be useful to obtain order of magnitude estimates on the requirements for these other errors.

The next type of error that can result from tip/tilt errors is a beam overlap error as is evident from Fig. 4.2 since the beam location on the right hand mirror is shifted. For this we will assume that the input beam from the right is shifted by a distance x_0, so that ${}^{in}\vec{E}_{right}\left(z=0\right)=\hat{x}E_0 e^{-\frac{\left((x-x_0)^2+y^2\right)}{{w_0}^2}}$. The following formulas can then be easily calculated for the output power and the combining efficiency given in Eq. 4.3.

$$
\begin{aligned}
{}^{out}P_{right} &= \frac{1}{2\mu_0}\mathbb{R}\left\{\int_{-\infty}^{\infty}\int_{-\infty}^{\infty} dxdy\left({}^{out}\vec{E}_{right}\left(x,y\right)\times {}^{out}\vec{B}^{*}_{right}\left(x,y\right)\right)\cdot\hat{z}\right\} \\
{}^{out}P_{right} &= \frac{1}{2c\mu_0}\mathbb{R}\left\{\int_{-\infty}^{\infty}\int_{-\infty}^{\infty} dxdy\left({}^{in}\vec{E}_{left}\left(x,y\right)\times\hat{z}\times {}^{in}E^{*}_{left}\left(x,y\right)\right)\cdot\hat{z}\left[\frac{1+e^{\frac{2xx_0-{x_0}^2}{{w_0}^2}}}{\sqrt{2}}\right]^2\right\} \\
{}^{out}P_{right} &= \left(\frac{{E_0}^2}{2c\mu_0}\right)\frac{\pi{w_0}^2}{2}\left[1+e^{-\frac{{x_0}^2}{2{w_0}^2}}\right]\approx\left(\frac{{E_0}^2}{2c\mu_0}\right)\frac{\pi{w_0}^2}{2}\left[2-\frac{{x_0}^2}{2{w_0}^2}\right] \\
\eta_{bc} &= \frac{{}^{out}P_{right}}{{}^{in}P_{tot}}\approx 1-\frac{\left(\frac{x_0}{w_0}\right)^2}{4}
\end{aligned}
\tag{4.3}
$$

This formula can be easily related to the combining efficiency formula from Eq. 4.2. This comparison suggests that the ratio of the beam offset to the beam radius produces a roughly equal effect to a cavity phase error so that $\frac{x_0}{w_0}\approx 0.02$ is a good target for high quality stacking. If the beam offset is caused by a mirror tip/tilt error so that $x_0\approx 2L\theta$, then to be roughly equivalent to $\Delta\delta=0.02$, you would like $\theta\le\frac{0.01w_0}{L}\approx 10\mu rads$ for a beam radius of $w_0\approx 1mm$ and $L\approx 1m$.

The final type of tip/tilt related error to be analyzed occurs due to having imperfect interference between two optical beams that are not exactly collinear. This effect can be analyzed by first considering the electric field of a beam in a rotated reference frame so that ${}^{in}\vec{E}_{right}\left(x',y',z'\right)=\hat{x}'e^{-\frac{\left(x'^2+y'^2\right)}{w_0{}^2}}e^{-ikz'}$, where these rotated coordinates are chosen so that $x'=x,\ y'=y\cos\psi+z\sin\psi,\ z'=-y\sin\psi+z\cos\psi$. This allows the field in the original coordinates to be written as ${}^{in}\vec{E}_{right}\left(x,y,z=0\right)=\hat{x}e^{-\frac{\left(x^2+y^2\cos^2\psi\right)}{w_0{}^2}}e^{iky\sin\psi}$. Thus after interfering with the original field from the left, the following formula for the combined power and the combining efficiency can be obtained as in Eq. 4.4.

$$
\begin{aligned}
{}^{out}P_{right}&=\frac{1}{2\mu_0}\mathbb{R}\left\{\int_{-\infty}^{\infty}\int_{-\infty}^{\infty}dxdy\left({}^{out}\vec{E}_{right}\left(x,y\right)\times{}^{out}\vec{B}^{*}_{right}\left(x,y\right)\right)\cdot\hat{z}\right\}\\
{}^{out}P_{right}&\approx\left(\frac{E_0{}^2}{2c\mu_0}\right)\frac{\pi w_0{}^2}{4}\left[2+\frac{\left[1+\cos\psi\right]\sqrt{2}}{\sqrt{\cos^2\psi+1}}e^{-\frac{k^2w_0{}^2\sin^2\psi}{4\left(\cos^2\psi+1\right)}}\right]\approx\left(\frac{E_0{}^2}{2c\mu_0}\right)\frac{\pi w_0{}^2}{2}\left[2-\frac{k^2w_0{}^2\psi^2}{8}\right]\\
\eta_{bc}&=\frac{{}^{out}P_{right}}{{}^{in}P_{tot}}\approx1-\frac{\left(\frac{kw_0\psi}{2}\right)^2}{4}
\end{aligned}
\qquad (4.4)
$$

This result is given in terms of the angle between the beams, but this angle can be related to the mirror tip/tilt angle as seen in Fig. 4.2 by $\psi=2\theta$. Now again a comparison can be made between this error and that due to an error in cavity phase. Again for a cavity phase error of $\Delta\delta=0.02$, the corresponding mirror tip/tilt angle should be $\theta\le\frac{0.01\lambda}{\pi w_0}\approx3\mu rads$ for $\lambda\approx1\mu m,\ w_0\approx1mm$.

The effect of diffraction on the interference between two optical beams can also be considered for a general interferometer. The simple two beam interference is analyzed using

Gaussian beams where each Gaussian beam has travelled a different distance from the focal point. The formula for a Gaussian beam that has travelled a distance z from its focal point is given below in Eq. 4.5 [14].

$$\vec{E}(x,y,z) = \hat{x}E_0 \frac{w_0}{w(z)} e^{-\frac{x^2+y^2}{w^2(z)}} e^{-i\frac{k\left[x^2+y^2\right]}{2R(z)}} e^{i\psi(z)} e^{-ikz}$$
$$w(z) = w_0\sqrt{1+\left(\frac{z}{z_R}\right)^2},\ R(z) = z\left[1+\left(\frac{z}{z_R}\right)^2\right],\ \xi(z) = \tan^{-1}\left(\frac{z}{z_R}\right), z_R = \frac{\pi w_0^{\,2}}{\lambda} \tag{4.5}$$

Now we can use the formulas from Eq. 4.5 to analyze the interference between a Gaussian beam that has travelled a distance z_1 from its focal point and a Gaussian beam that has travelled a distance z_2 from its focal point (neglecting the e^{-ikz} phase terms, since that overall phase can be corrected before interference) in the same manner as was done in section 4.1. Again the total power in each beam is ${}^{in}P_{left} = {}^{in}P_{right} = \left(\frac{E_0^{\,2}}{2c\mu_0}\right)\frac{\pi w_0^{\,2}}{2}$. The total output combined power along with the combining efficiency is given below in Eq. 4.6.

$$
\begin{aligned}
{}^{out}P_{right} &= \frac{1}{2\mu_0}\mathbb{R}\left\{\int_{-\infty}^{\infty}\int_{-\infty}^{\infty} dxdy\left({}^{out}\vec{E}_{right}(x,y)\times {}^{out}\vec{B}^{*}_{right}(x,y)\right)\cdot\hat{z}\right\} \\
{}^{out}P_{right} &= \left(\frac{{E_0}^2}{2c\mu_0}\right)\frac{\pi {w_0}^2}{2}\left[1+\frac{2}{w(z_1)w(z_2)}\left\{\frac{\left[\frac{1}{w^2(z_1)}+\frac{1}{w^2(z_2)}\right]\cos\left(\xi(z_1)-\xi(z_2)\right)+\frac{k}{2}\left[\frac{1}{R(z_1)}-\frac{1}{R(z_2)}\right]\sin\left(\xi(z_1)-\xi(z_2)\right)}{\left[\frac{1}{w^2(z_1)}+\frac{1}{w^2(z_2)}\right]^2+\frac{k^2}{4}\left[\frac{1}{R(z_1)}-\frac{1}{R(z_2)}\right]^2}\right\}\right] \\
{}^{out}P_{right} &\approx \left(\frac{{E_0}^2}{2c\mu_0}\right)\frac{\pi {w_0}^2}{2}\left[2-\frac{1}{4}\left[\frac{z_1-z_2}{z_R}\right]^2\right] \\
\eta_{bc} &= \frac{{}^{out}P_{right}}{{}^{in}P_{tot}} \approx 1-\frac{\left(\frac{z_1-z_2}{z_R\sqrt{2}}\right)^2}{4}
\end{aligned}
\tag{4.6}
$$

This result shows how the combining efficiency depends on the difference between distance propagated from the focal point for two beams, assuming that distance is much smaller than the Rayleigh range $z_1, z_2 \ll z_R$. Again a comparison can be made to the case of cavity phase errors, which shows that in order to be similar to a cavity phase error of $\Delta\delta = 0.02$, the propagation distance must be $|z_1 - z_2| \le 0.03 z_R \approx 9cm$ assuming $\lambda \approx 1\mu m,\ w_0 \approx 1mm$.

In this section, it is clear that in most situations, the sensitivity of interference to mirror tip/tilt errors is dominated by the piston error resulting from the pivot of the mirror not being at the center of the mirror. This error can potentially be mitigated by using a gimballed mirror mount. The only error not related to mirror tip/tilt errors analyzed in this section was the one due to optical diffraction, which will also be furthered analyzed in subsequent sections for the specific cavity designs.

4.3 Flat Mirror GTI Pulse Stackers

The simplest travelling wave GTI cavity arrangement can be configured using 3 or more flat mirrors so that the beam returns to its initial trajectory after a single roundtrip. For cavities with an odd number of mirrors, the beam will be inverted upon a roundtrip, so the beam must be inversion symmetric (like an LP_{01} mode) in order for these cavities to be applicable. Additionally for cavities with an odd number of mirrors, due to the inversion property, the polarization must be either horizontal or vertical to avoid polarization errors. For cavities with an even number of mirrors, the beam will not be changed upon a roundtrip, so the only consideration for these cavities is effects due to diffraction.

Assuming that the primary concern for the flat mirror travelling wave GTI is diffraction, beam propagation simulations must be done to determine how the stacking fidelity (pre-pulse contrast, stacking efficiency, etc.) depends on the input beam size. The beam propagation can be easily performed in the spatial frequency domain using the Fresnel approximation to the transfer function of free space as given below in Eq. 4.7.

$$H\left(k_x, k_y, L\right) = e^{iL\sqrt{k_0{}^2 - k_x{}^2 - k_y{}^2}} \approx e^{iLk_0} e^{-iL\left(\frac{k_x{}^2 + k_y{}^2}{2k_0}\right)} \tag{4.7}$$

Where here L is the roundtrip length of the GTI, k_0 is the wave vector of the central frequency, and k_x and k_y are the components of the wave vector in the x and y direction respectively.

In order to take into account the effect of the GTI as well, after a single roundtrip the electric field inside the GTI is added coherently to the input field to create a new intra-cavity field as well as an output field from the cavity using a modified version of Eq. 2.3. This process is repeated for each pulse in the burst to determine the total output field as a function of space

and time. The modified equations to include the spatial beam propagation are given below in Eq. 4.8.

$$
\begin{aligned}
{}^{out}\tilde{A}(x,y)[n] &= {}^{in}\tilde{A}(x,y)[n]r + \mathcal{F}^{-1}\left\{ e^{-iL\left(\frac{k_x^2+k_y^2}{2k_0}\right)} \mathcal{F}\left\{ {}^{cav}\tilde{A}(x,y)[n-1] \right\} \right\} ite^{i\delta} \\
{}^{cav}\tilde{A}(x,y)[n] &= {}^{in}\tilde{A}(x,y)[n]it + \mathcal{F}^{-1}\left\{ e^{-iL\left(\frac{k_x^2+k_y^2}{2k_0}\right)} \mathcal{F}\left\{ {}^{cav}\tilde{A}(x,y)[n-1] \right\} \right\} re^{i\delta}
\end{aligned}
\tag{4.8}
$$

As a specific example, this process is performed for the test bed system of 4 GTIs from Fig. 2.4. The graph showing the dependence of the pre-pulse contrast and the stacking efficiency on the beam size is given below in Fig. 4.4. This system is assuming a central wavelength of 1.04μm, and it is assumed that the spacing between the cavities is negligibly small, although that can also be easily taken into account by using a separate transfer function with a different length between the cavities in the simulation. The results are plotted with respect to $\frac{z_R}{L}$ since that is the dependence we expect due to Eq. 4.6.

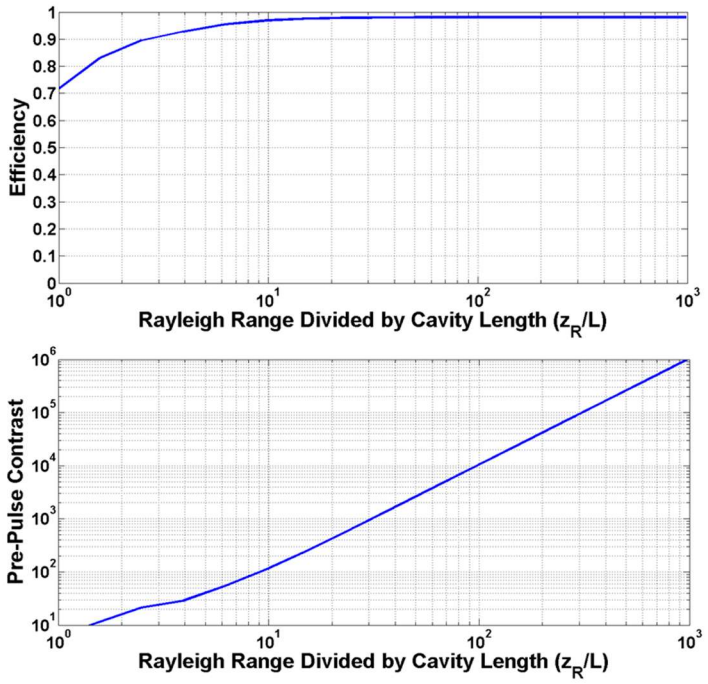

Figure 4.4: (top) Stacking efficiency as a function of beam size for the 4 cavity system as a function of the Rayleigh range divided by the cavity length (bottom) Pre-pulse contrast as a function of beam size for that same system

The results from Fig. 4.4 tell the cavity lengths needed to obtain a specified stacking efficiency and pre-pulse contrast. The result from Eq. 4.6 yielded a prediction of ~30dB pre-pulse contrast when $L \approx 30 z_R$, which indeed agrees with the detailed simulation in Fig. 4.4.

It is quite straightforward to determine the energy/power handling of these flat mirror GTIs since the beam size must change negligibly upon a roundtrip in order to have good interference. This means that in order to accommodate larger energies, the beam size must increase, which actually will improve the interference quality. For most optical mirrors, damage occurs at a specified fluence value F, usually measured in $\frac{J}{cm^2}$. State of the art high reflectivity mirrors can have damage thresholds of around $F_{damage} \approx 10 \frac{J}{cm^2}$ for 1ns pulses at 1μm wavelength. This damage threshold typically scales as

$F_{damage}(\lambda,\tau) \approx F_{damage}(\lambda_{ref},\tau_{ref})\left[\sqrt{\frac{\lambda}{\lambda_{ref}}}\right]\left[\sqrt{\frac{\tau}{\tau_{ref}}}\right]$ for wavelength λ and pulse duration τ compared to a reference wavelength λ_{ref} and reference pulse duration τ_{ref} [24]. In order to handle a final stacked 1ns pulse at 1μm wavelength with an energy of 10J, a beam radius of $w_0 \geq 6mm$ is required. Since these flat mirror GTIs can have arbitrarily high energy handling capabilities, it is desirable to have flat mirror GTIs be the final cavities in the system, since that is where the shortest effective pulse duration occurs.

Overall the flat mirror GTIs provide a lot flexibility with how to arrange the cavities as a path to scaling to high energy, since increasing the beam size improves the stacking performance. An example of using all flat mirror GTIs for a 4+4 multiplexed GTI sequence where the first set of 4 GTIs have a roundtrip length of 30cm and the second set of 4 GTIs have a roundtrip length of 2.7m is shown compactly arranged below in Fig. 4.5. The complete arrangement can fit in an area of 1m x 1m.

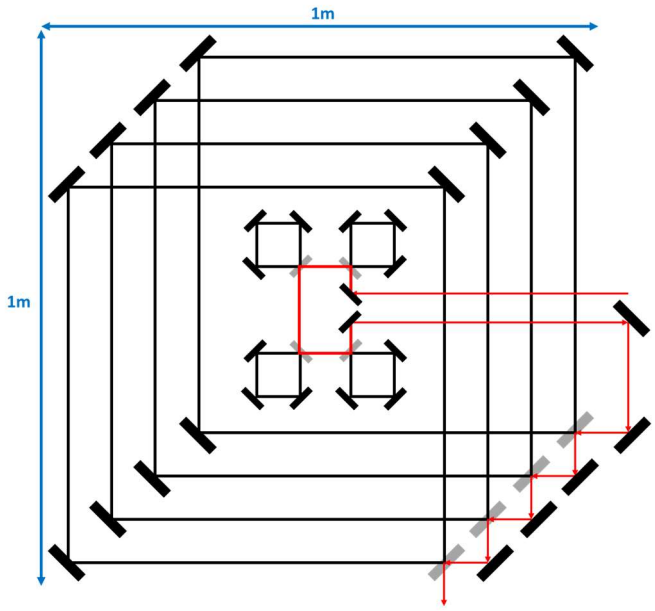

Figure 4.5: Potential compact arrangement of 4+4 GTI multiplex with flat mirror cavities

4.4 Herriott Cell Folded GTI Pulse Stackers

A GTI cavity containing a Herriott cell can be very useful for creating optical cavities that contain long propagation lengths, while also fitting in a small area. The analysis of diffraction effects for these Herriott cavities is very similar to the analysis for the flat mirror cavities from the previous section 4.3. In addition to the diffraction analysis, a more basic understanding of how the Herriott cells act as an optical relay with unit magnification is needed for design purposes.

A Herriott cell is an arrangement of two mirrors, with at least one of the mirrors being concave, with a specified separation such that a specified optical ray will exactly reproduce itself after making an integer number of passes between the mirrors [29], as shown in Fig. 4.6. The condition that the ray exactly reproduce itself is referred to as the re-entrant condition. Another important property of the Herriott cell is that if a Gaussian beam is co-linear with the optical ray that satisfies this re-entrant condition, then that Gaussian beam will reproduce its initial size and curvature after making the specified number of passes between the mirrors (in the paraxial approximation) [30]. This self-imaging property of the Herriott cell is due to the fact that the ray analysis for the re-entrant condition is done using the ABCD matrix formalism, which is also applicable to the propagation of Gaussian beams.

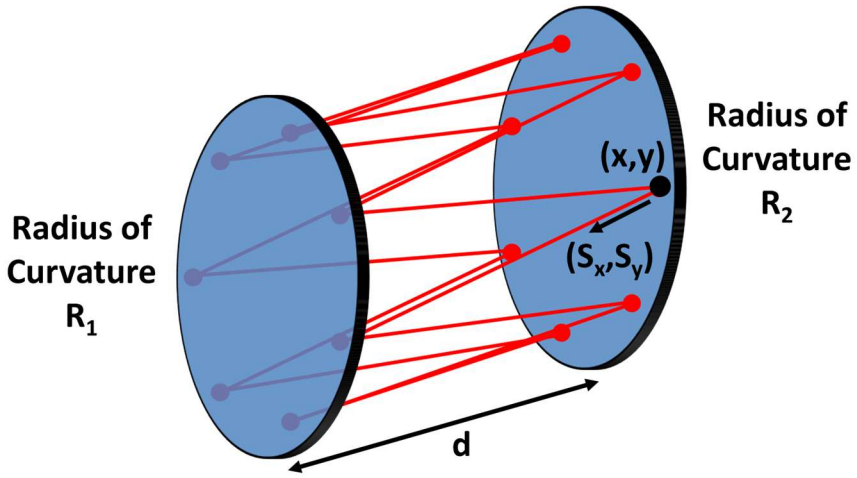

Figure 4.6: Herriott cell diagram

The ABCD ray matrix analysis of the Herriott cell starts with defining the optical ray as a vector as follows in Eq. 4.9:

$$\vec{r} = \begin{bmatrix} x \\ S_x \\ y \\ S_y \end{bmatrix} \tag{4.9}$$

where here x and y are the position coordinates of the ray and S_x and S_y are the slopes in the x and y direction respectively. In addition to the ray vector, we also need the transfer matrix for a curved mirror as well as the transfer matrix for free space propagation, both of which are given below in Eq. 4.10.

$$\text{Curved mirror transfer matrix} = T(R) = \begin{bmatrix} 1 & 0 & 0 & 0 \\ \frac{-2}{R} & 1 & 0 & 0 \\ 0 & 0 & 1 & 0 \\ 0 & 0 & \frac{-2}{R} & 1 \end{bmatrix} \tag{4.10}$$

$$\text{Free space transfer matrix} = T(d) = \begin{bmatrix} 1 & d & 0 & 0 \\ 0 & 1 & 0 & 0 \\ 0 & 0 & 1 & d \\ 0 & 0 & 0 & 1 \end{bmatrix}$$

Here R is the radius of curvature of the mirror and d is the distance travelled through free space. Since the x and y components of the transfer matrices do not couple, the analysis can be done more easily by only considering either the x or y components, thus reducing the size of the ray vector to 2x1 and the transfer matrices to 2x2. The next step is to calculate the transfer matrix for a full roundtrip between the two mirrors, which consists of propagating the distance between the mirrors twice and hitting each mirror once. This roundtrip transfer matrix is given below in Eq. 4.11.

$$T_{roundtrip} = T(R_2)T(d)T(R_1)T(d) = \begin{bmatrix} 1 & 0 \\ \frac{-2}{R_2} & 1 \end{bmatrix}\begin{bmatrix} 1 & d \\ 0 & 1 \end{bmatrix}\begin{bmatrix} 1 & 0 \\ \frac{-2}{R_1} & 1 \end{bmatrix}\begin{bmatrix} 1 & d \\ 0 & 1 \end{bmatrix}$$

$$T_{roundtrip} = \begin{bmatrix} 1-\frac{2d}{R_1} & 2d-\frac{2d^2}{R_1} \\ \frac{4d}{R_1R_2}-\frac{2}{R_1}-\frac{2}{R_2} & 1+\frac{4d^2}{R_1R_2}-\frac{2d}{R_1}-\frac{4d}{R_2} \end{bmatrix} = \begin{bmatrix} A & B \\ C & D \end{bmatrix} \tag{4.11}$$

Where here the components of the transfer matrix are simply denoted as A, B, C, and D. The next step is to determine what the transfer matrix is after n roundtrips through the Herriott cell, which can be analyzed after doing an eigenvalue decomposition on the transfer matrix. The eigenvalues for a general 2x2 matrix are given below in Eq. 4.12.

$$\lambda_{\pm} = \frac{A+D}{2} \pm \sqrt{\left(\frac{A+D}{2}\right)^2 - \left(AD - BC\right)} \tag{4.12}$$

Where the two eigenvalues are given by $\lambda_{\pm}$. The next step is to simplify the expression for the eigenvalues by using some specific properties of the roundtrip transfer function. The first property is that we require Herriott cell to be stable, which means we need $\left|\frac{A+D}{2}\right| \leq 1$. The second property is that for the form of $T_{roundtrip}$ given in Eq. 4.5, $\left(AD - BC\right) = 1$. Then we can make the following substitution $\frac{A+D}{2} = \cos\left(\theta\right)$ and simplify Eq. 4.6 to the following Eq. 4.13.

$$\lambda_{\pm} = e^{\pm i\theta} \tag{4.13}$$

This special form for the eigenvalues is only possible because of the special form of $T_{roundtrip}$. Now the goal is to use this in order to find the transfer function after n roundtrips, which when written in the eigenvalue decomposition is the following formula Eq. 4.14.

$$\left(T_{roundtrip}\right)^n = S\Lambda^n S^{-1} \tag{4.14}$$

In this equation, Λ is the matrix of eigenvalues, and S is the matrix containing the eigenvectors, so that if $\vec{v}_+, \vec{v}_-$ are the eigenvectors corresponding to λ_+, λ_-, then $S = \left[\vec{v}_+, \vec{v}_-\right]$. The equation for S is given below in Eq. 4.15.

$$S = \frac{1}{B\left(B - C\right)}\begin{bmatrix} B & B \\ -\left(A - e^{i\theta}\right) & -\left(A - e^{-i\theta}\right) \end{bmatrix} \tag{4.15}$$

The final step is to substitute everything in to Eq. 4.14 and simplify the result, which is given below in Eq. 4.16.

$$\left(T_{roundtrip}\right)^n = \begin{bmatrix} \frac{(A-D)}{2}\frac{\sin(n\theta)}{\sin(\theta)} + \cos(n\theta) & B\frac{\sin(n\theta)}{\sin(\theta)} \\ C\frac{\sin(n\theta)}{\sin(\theta)} & -\frac{(A-D)}{2}\frac{\sin(n\theta)}{\sin(\theta)} + \cos(n\theta) \end{bmatrix} = \begin{bmatrix} 1 & 0 \\ 0 & 1 \end{bmatrix} \tag{4.16}$$

Now in order to satisfy the re-entrant condition, we require that after the n roundtrips the total transfer function be equal to the identity matrix (as already given in Eq. 4.16). This puts the following constraint on the parameter θ.

$$n\theta = m\pi \tag{4.17}$$

Where here we require that m be an even integer. This is the condition required for the ray to exactly reproduce itself after n roundtrips between the Herriott cell mirrors.

It is clear from this analysis that after n roundtrips between the mirrors, the ray has travelled a total distance of $L_{tot} = 2dn$. The condition from Eq. 4.17 then puts the following constraint on the mirror curvatures, given in Eq. 4.18.

$$R_1 = \frac{\left(\frac{L_{tot}}{n}\right)^2 - \frac{2R_2 L_{tot}}{n}}{\frac{2L_{tot}}{n} - 2R_2\left(1-\cos\left(\frac{m\pi}{n}\right)\right)} \tag{4.18}$$

Furthermore, in the case that $R_2 = \infty$, which means that the mirror is flat, Eq. 4.18 can be simplified to the following form given in Eq. 4.19.

$$R_1 = \frac{L_{tot}}{n\left(1-\cos\left(\frac{m\pi}{n}\right)\right)} \tag{4.19}$$

The next step is to determine a desirable input optical ray for the Herriott cell. Since typically the mirrors in the optical setup will be circular, it would be advantageous if the beam traced out a

circular pattern across the mirrors as it propagates between them. This circular pattern can be achieved for the following input optical ray given in Eq. 4.20.

$$\vec{r}_0 = \begin{bmatrix} x_0 \\ \frac{x_0}{2B}(D-A) \\ 0 \\ \frac{x_0 \sin(\theta)}{B} \end{bmatrix} \tag{4.20}$$

Where here $\vec{r}_0$ is the input optical ray and x_0 defines the radius of the circle that will be traced out on each mirror. The even integer m also serves an important role in this analysis, which is to specify how many full circles the beam makes on the mirrors (e.g. m=2 gives one full circle, m=4 gives two full circles, etc.). Since we will be putting these Herriott cells inside GTIs, typically we would like the beam to only make one full circle (corresponding to m=2), since we will need to get the beam into the Herriott cell as well as extract it.

An important consideration for these Herriott cells is how stable they are to various errors that could occur. A first order perturbation analysis can be done on the Herriott cell consisting of one flat and one curved mirror in order to determine the total transfer function in the presence of potential errors in the mirror radius of curvature $R = R_{opt} + \Delta R$ and in the mirror separation $d = d_{opt} + \Delta d$. This first order analysis results in the following perturbed total transfer function given below in Eq. 4.21.

$$\left(T_{roundtrip}\right)^{n}_{ij}\left(R,d\right)\approx\left\{\begin{array}{l}\left(T_{roundtrip}\right)^{n}_{ij}\left(R_{opt},d_{opt}\right)\\+\Delta R\dfrac{\partial}{\partial R}\left[\left(T_{roundtrip}\right)^{n}_{ij}\right]\left(R_{opt},d_{opt}\right)\\+\Delta d\dfrac{\partial}{\partial d}\left[\left(T_{roundtrip}\right)^{n}_{ij}\right]\left(R_{opt},d_{opt}\right)\end{array}\right\}$$

$$\left(T_{roundtrip}\right)^{n}\approx\begin{bmatrix}1 & nd_{opt}\left[\dfrac{\Delta d}{d_{opt}}-\dfrac{\Delta R}{R_{opt}}\right]\\ \dfrac{-n}{R_{opt}-d_{opt}}\left[\dfrac{\Delta d}{d_{opt}}-\dfrac{\Delta R}{R_{opt}}\right] & 1\end{bmatrix} \tag{4.21}$$

The next step is to examine the effect of this total transfer function on a Gaussian beam using the ABCD matrix formalism. This is done using the Gaussian beam q parameter, where we will assume that before the Herriott cell the q parameter is $q_0 = iz_R = i\dfrac{\pi w_0^{\,2}}{\lambda}$, then after the Herriott cell the q parameter is given below in Eq. 4.22.

$$q' = \frac{iz_R + nd_{opt}\left[\dfrac{\Delta d}{d_{opt}}-\dfrac{\Delta R}{R_{opt}}\right]}{-iz_R\dfrac{n}{R_{opt}-d_{opt}}\left[\dfrac{\Delta d}{d_{opt}}-\dfrac{\Delta R}{R_{opt}}\right]+1} \tag{4.22}$$

This formula in Eq. 4.22 can be used to extract the information about the perturbed radius of curvature R' and the perturbed Gaussian beam radius w' using the formulas given below in Eq. 4.23.

$$\begin{aligned}\frac{1}{R'} &= \mathrm{Re}\left\{\frac{1}{q'}\right\}\\ \frac{-\lambda}{\pi w'^{2}} &= \mathrm{Im}\left\{\frac{1}{q'}\right\}\end{aligned} \tag{4.23}$$

These formulas can be solved keeping only the lowest order terms and the results are given below in Eq. 4.24.

$$\begin{aligned}\frac{1}{R'} &\approx nd\left[\frac{1}{z_R{}^2}-\frac{1}{d_{opt}\left[R_{opt}-d_{opt}\right]}\right]\left[\frac{\Delta d}{d_{opt}}-\frac{\Delta R}{R_{opt}}\right]\\ \frac{w'^2}{w_0{}^2} &\approx 1+n^2 d_{opt}{}^2\left[\frac{1}{z_R{}^2}-\frac{1}{d_{opt}\left[R_{opt}-d_{opt}\right]}\right]\left[\frac{\Delta d}{d_{opt}}-\frac{\Delta R}{R_{opt}}\right]^2\end{aligned} \tag{4.24}$$

These equations are quite interesting, because they show that the Herriott cell is most stable when the Rayleigh range of the input beam is close to that of the eigenbeam of the two mirror system which occurs for $z_R = z_{HC} = \sqrt{d_{opt}\left[R_{opt}-d_{opt}\right]}$, and is when the Gaussian beam q-parameter reproduces itself after every roundtrip between the two mirrors. They also suggest that a manufacturing error in the radius of curvature of the curved mirror can be compensated to lowest order by slightly changing the mirror separation.

Now in order to use this type of Herriott cell in a GTI, there is typically some length L_{input} both before and after the Herriott cell. When analyzing the full GTI including this extra length, it is important to determine the eigenbeam for the GTI, since this is the beam that will be exactly reproduced after a full roundtrip through the GTI. This analysis can also be done using the ABCD matrices and the transfer function for the GTI is given below in Eq. 4.25.

$$\begin{aligned}T_{GTI} &= \begin{bmatrix}1 & L_{input}\\ 0 & 1\end{bmatrix}\begin{bmatrix}\cos(n\theta) & B\dfrac{\sin(n\theta)}{\sin(\theta)}\\ C\dfrac{\sin(n\theta)}{\sin(\theta)} & \cos(n\theta)\end{bmatrix}\begin{bmatrix}1 & L_{input}\\ 0 & 1\end{bmatrix}\\ T_{GTI} &= \begin{bmatrix}\cos(n\theta)-\dfrac{L_{input}\sin(n\theta)}{\sqrt{d\left[R_1-d\right]}} & \sqrt{d\left[R_1-d\right]}\sin(n\theta)+2L_{input}\cos(n\theta)-\dfrac{L_{input}{}^2\sin(n\theta)}{\sqrt{d\left[R_1-d\right]}}\\ \dfrac{-\sin(n\theta)}{\sqrt{d\left[R_1-d\right]}} & \cos(n\theta)-\dfrac{L_{input}\sin(n\theta)}{\sqrt{d\left[R_1-d\right]}}\end{bmatrix}\end{aligned} \tag{4.25}$$

This transfer function can be used to determine the Gaussian beam q parameter for the eigenbeam of the GTI q_{eigen}, which can in turn be used to determine the beam radius for the eigenbeam w_{eigen}. The formulas for each of these quantities are given below in Eq. 4.26.

$$q_{eigen} = \frac{i\pi w_{eigen}^{\ 2}}{\lambda} = i\sqrt{2L_{input}\sqrt{d\left[R_1 - d\right]}\frac{\cos\left(n\theta\right)}{\sin\left(n\theta\right)} + d\left[R_1 - d\right] - L_{input}^{\ 2}}$$
$$w_{eigen} = \sqrt{\frac{\lambda}{\pi}}\left[2L_{input}\sqrt{d\left[R_1 - d\right]}\frac{\cos\left(n\theta\right)}{\sin\left(n\theta\right)} + d\left[R_1 - d\right] - L_{input}^{\ 2}\right]^{\frac{1}{4}} \tag{4.26}$$

Mode matching the GTI is necessary in order to avoid imperfect interference resulting from the GTI not perfectly reproducing the beam after a single roundtrip.

A GTI containing a Herriott cell can suffer from many of the same mirror tip/tilt errors as a flat mirror cavity. The most severe error resulting from the mirror tip/tilt errors analyzed in section 4.1 was the cavity phase error resulting from the mirror pivot not being in the center of the mirror. Since a Herriott cell includes multiple bounces between two mirrors, this type of error can be magnified. Fig. 4.7 below shows both a front view and a side view of one of the Herriott cell mirrors for a Herriott cell with n=4 and m=2.

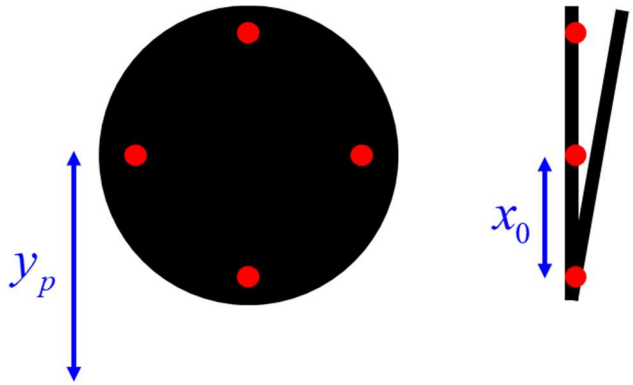

Figure 4.7: (left) Front view of a Herriott cell mirror for n=4, m=2. (right) Side view of that same mirror along with a tilted version of that mirror showing how each spot experiences a different length error

As can be seen from Fig. 4.7, each roundtrip pass through the Herriott cell experiences a different length error based on the location of where the spot hits the mirror. The total path length error for propagation through the Herriott cell is simply the sum of the individual errors. This means if one of the mirrors in the Herriott cell is tilted by an angle θ, then the total cavity phase error will be $\Delta\delta_{tot} = k_0 \Delta z_{tot} \approx \frac{4\pi n y_p \theta}{\lambda}$. Note that for every spot a distance x above the center of the mirror, there is another spot a distance x below the center of the mirror, so the choice of x_0 does not affect the total cavity phase error to lowest order.

Up to this point, we have used ray optics to only describe how a ray propagates in a Herriott cell. The next step is to again use Fresnel diffraction to determine beam size requirements for the beam into the GTI that contains the Herriott cell. A figure showing the Herriott cavity is given below in Fig. 4.8 with the various cavity parameters specified.

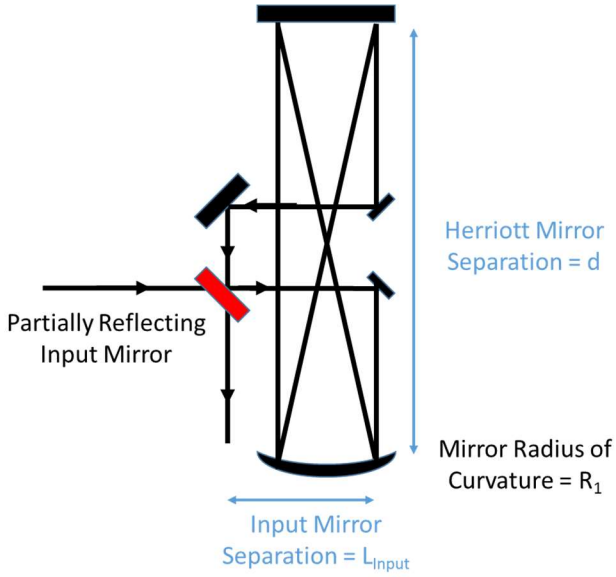

Figure 4.8: GTI containing a Herriott cell

This GTI cavity has a total roundtrip length given by $L_{roundtrip} = 2L_{input} + 2dn$. The beam propagation for a single roundtrip through the GTI can be performed using Fresnel diffraction and transfer functions. The transfer function for free space propagation is given in the spatial

frequency domain by Eq. 4.7. The transfer function for the curved mirror is given in the spatial domain by the following Eq. 4.27.

$$T_{CM}\left(x,y,R_1\right)=e^{-ik_0\frac{x^2+y^2}{R_1}} \tag{4.27}$$

The propagation for a single roundtrip through the Herriott cell is given by the same sequence of transfer functions as was used in Eq. 4.11. The only difference is that now these transfer functions are in the spatial or spatial frequency domain. The transfer function for a single roundtrip is given below in Eq. 4.28.

$$T_{H\_rt}\left\{\tilde{A}\left(x,y\right)\right\}=e^{-ik_0\frac{x^2+y^2}{R_2}}\mathcal{F}^{-1}\left\{e^{-id\left(\frac{k_x{}^2+k_y{}^2}{2k_0}\right)}\mathcal{F}\left\{e^{-ik_0\frac{x^2+y^2}{R_1}}\mathcal{F}^{-1}\left\{e^{-id\left(\frac{k_x{}^2+k_y{}^2}{2k_0}\right)}\mathcal{F}\left\{\tilde{A}\left(x,y\right)\right\}\right\}\right\}\right\} \tag{4.28}$$

This transfer function can be used n times for propagating n roundtrips through the Herriott cell. In order to complete the cavity to obtain the full GTI roundtrip transfer function, we also need to include the free space propagation before and after the Herriott cell. This full GTI roundtrip transfer function is written out in Eq. 4.29.

$$T_{GTI\_rt}\left\{\tilde{A}\left(x,y\right)\right\}=\mathcal{F}^{-1}\left\{e^{-iL_{input}\left(\frac{k_x{}^2+k_y{}^2}{2k}\right)}\mathcal{F}\left\{T_{H\_rt}{}^{n}\left\{\mathcal{F}^{-1}\left\{e^{-iL_{input}\left(\frac{k_x{}^2+k_y{}^2}{2k}\right)}\mathcal{F}\left\{\tilde{A}\left(x,y\right)\right\}\right\}\right\}\right\}\right\} \tag{4.29}$$

So in order to analyze the effect of the beam size on this GTI, we need to create a set of equations that takes into account this propagation effect. Similar to Eq. 4.8, the GTI equations are given below in Eq. 4.30.

$$\begin{aligned}{}^{out}\tilde{A}\left(x,y\right)\left[n\right]&={}^{in}\tilde{A}\left(x,y\right)\left[n\right]r+T_{GTI\_rt}\left\{{}^{cav}\tilde{A}\left(x,y\right)\left[n-1\right]\right\}ite^{i\delta}\\{}^{cav}\tilde{A}\left(x,y\right)\left[n\right]&={}^{in}\tilde{A}\left(x,y\right)\left[n\right]it+T_{GTI\_rt}\left\{{}^{cav}\tilde{A}\left(x,y\right)\left[n-1\right]\right\}re^{i\delta}\end{aligned} \tag{4.30}$$

Similar to section 4.2, we can now analyze the effect of the beam size, along with the mirror radius of curvature, the input mirror separation, and the Herriott mirror separation on the pulse stacking fidelity. Simulations have been done for the 4 cavity pulse stacking with 9 pulses for the following set of Herriott cavity parameters that accurately represent experimental conditions: $R_1 = 1m,\ R_2 = \infty,\ L_{roundtrip} = 2.75m,\ L_{input} = 0.05m,\ n = 7,\ m = 2$.

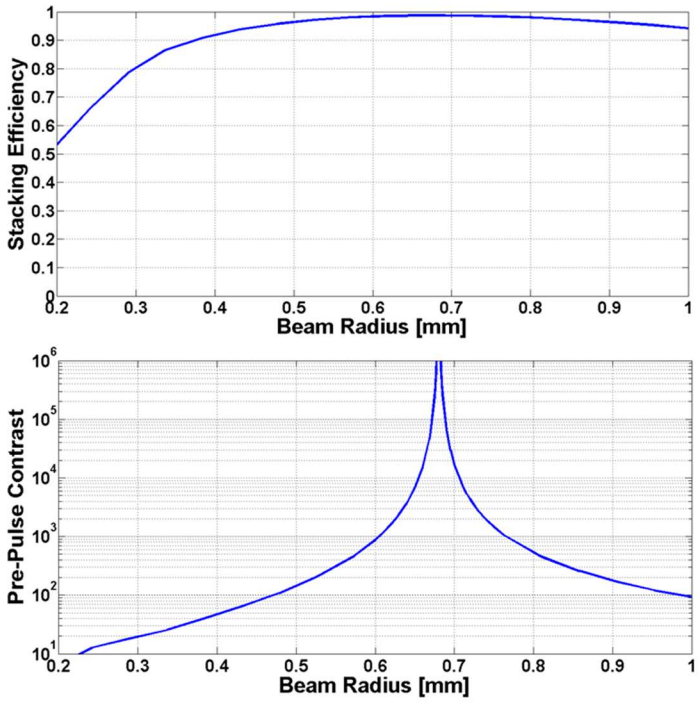

Figure 4.9: (top) Stacking efficiency as a function of beam size for the 4 cavity system from Fig. 2.4 for 2.75m roundtrip length Herriott cavities with $L_{input} = 0.05m$. (bottom) Pre-pulse contrast as a function of beam size for that same system

As can be seen from Fig. 4.9, this Herriott cavity configuration requires a beam radius of $w_0 \approx 0.68mm$ to achieve perfect interference. For deviations from that ideal beam radius, the stacking efficiency and pre-pulse contrast both decrease. To maintain a pre-pulse contrast better than 30dB, the beam radius should be between 0.6mm and 0.75mm (roughly a $\pm 5\%$ tolerance) for this specific configuration.

Additionally we can also analyze the limiting case for this Herriott cavity when $L_{input} = 0$, which is when the whole GTI is a Herriott cell. For example, this can be accomplished by drilling a hole in one of the Herriott cell mirrors and inserting the partial reflector in that location. The pre-pulse contrast simulation for 4 cavities stacking 9 pulses is shown below for $R_1 = 1.044m,\ R_2 = \infty,\ L_{roundtrip} = 2.75m,\ L_{input} = 0m,\ n = 7,\ m = 2$. In this simulation all of the ideal values were used for the Herriott cell; therefore, this simulation simply shows the numerical error of the computation.

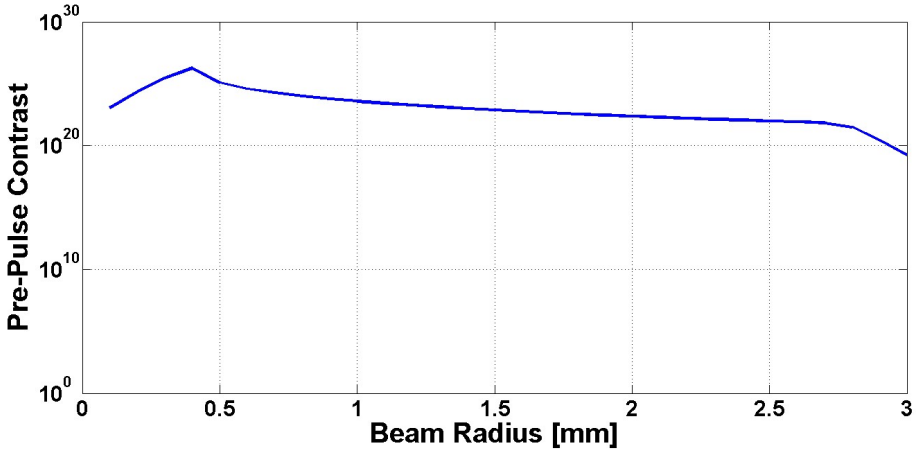

Figure 4.10: Pre-pulse contrast as a function of beam size for the 4 cavity system from Fig. 2.4 for 2.75m roundtrip length Herriott cavities with $L_{input} = 0$.

The next step is to analyze the energy/power handling of these Herriott cavities. This analysis will be based on the Herriott cavity from Fig. 4.8 with $L_{input} = 0$. For this type of cavity it was shown that the most robust operation to perturbations occurs when the input Rayleigh range $z_R = z_{HC} = \sqrt{d_{opt}\left[R_{opt} - d_{opt}\right]}$. When the input beam has this Rayleigh range, the beam not only reproduces itself after n roundtrips through the Herriott cell, but it also reproduces itself after every roundtrip through the Herriott cell. This property makes it rather straightforward to analyze the energy/power handling for a Herriott cavity of this type, since the beam size is

roughly the same size every time the beam hits one of the mirrors in the cavity. The expanded formula for the Rayleigh range of this Herriott cell eigenbeam is given below in Eq. 4.31.

$$z_{HC}{}^2 = d_{opt}\left[R_{opt} - d_{opt}\right]$$
$$z_{HC}{}^2 = \frac{L_{tot}}{2n}\left[\frac{L_{tot}}{n\left[1-\cos\left(\frac{m\pi}{n}\right)\right]} - \frac{L_{tot}}{2n}\right] \tag{4.31}$$

We are most interested in using these Herriott cells to make very compact GTIs, which is most effectively accomplished by having a large number of roundtrips (large n) through the Herriott cell. Furthermore, it is clear from Eq. 4.31 that when n=m, $z_{HC}{}^2 = 0$. Then for values n>m, the value of $z_{HC}{}^2$ asymptotically converges to $\frac{L_{tot}{}^2}{m^2\pi^2}$ as $n \to \infty$. The derivation for this is given below in Eq. 4.32.

$$\lim_{n\to\infty}\left\{z_{HC}{}^2\right\} = \lim_{n\to\infty}\left\{\frac{L_{tot}{}^2}{2n^2\left[1-\cos\left(\frac{m\pi}{n}\right)\right]} - \frac{L_{tot}{}^2}{4n^2}\right\}$$
$$\lim_{n\to\infty}\left\{z_{HC}{}^2\right\} = \lim_{n\to\infty}\left\{\frac{L_{tot}{}^2}{2n^2\left[1-\left(1-\frac{m^2\pi^2}{2n^2}\right)\right]}\right\} \tag{4.32}$$
$$\lim_{n\to\infty}\left\{z_{HC}{}^2\right\} = \frac{L_{tot}{}^2}{m^2\pi^2}$$

This derivation shows that if a large number of roundtrips is desired, then in order to have the largest Rayleigh range (and therefore the largest beam size) in the cavity, it is best if m is small, and since we have required that m be an even integer, it is clear that under these conditions, m=2 is optimal. The goal of this portion of the analysis was to derive a formula for the beam size in a

Herriott cavity so as to determine the energy/power handling of such a cavity. Now, by using Eq. 4.32, it is clear that the beam size in the Herriott cavity of this type will be approximately $w_{HC} \approx \sqrt{\frac{\lambda z_{HC}}{\pi}} \approx \sqrt{\frac{\lambda L_{tot}}{m\pi^2}} \approx \sqrt{\frac{\lambda L_{tot}}{2\pi^2}}$. With this beam size, the fluence of a laser pulse with energy E is given by $F_{laser} \approx \frac{E}{\pi w_{HC}^2} \approx \frac{2\pi E}{\lambda L_{tot}}$. Using the same laser damage threshold of $F_{damage} \approx 10\frac{J}{cm^2}$, then for 1μm wavelength laser pulse with 1ns pulse duration and a cavity roundtrip length of $L_{tot} = 2.75m$, this Herriott cavity has a beam size of $w_{HC} \approx 0.37mm$ and can handle a laser pulse energy up to $E \leq 40mJ$. Since the Herriott cavity cannot handle as large energies as the flat mirror cavities, the Herriott cavities should precede the flat mirror cavities in the optical layout since the effective pulse durations are longer there.

This analysis of the damage considerations for the Herriott cell was focused on the Herriott cell with 1 flat mirror and 1 curved mirror (which is what was used in the experiments). However, it is possible that other Herriott cell designs consisting of 2 curved mirrors could yield better energy/power handling performance.

4.5 Cavity Design Conclusions

There are many different potential cavity designs that can be beneficial for pulse stacking. The flat mirror cavity designs will typically be most useful when the Rayleigh range of the beam is much larger than the cavity length ($z_R \gg L$), which is the case for short cavities with moderate beam sizes and medium length cavities with large beam sizes (e.g. high energy beams). The Herriott cavity designs will be more appropriate when the Rayleigh range of the beam is comparable to the cavity length ($z_R \approx \frac{L}{6}$), which is the case for medium length cavities with moderate beam sizes (e.g. moderate energy beams) as well as for extremely long cavities

where it becomes impractical to have such large beams. These are the takeaway conclusions for choosing the cavity design for a specific application.

Chapter 5 Experimental Systems and Experimental Results

5.1 Overview

Several different proof-of-principle experiments have been done to illustrate the efficacy of coherent pulse stacking amplification, and those experiments have been accompanied by several different experimental setups. These experiments span the range of using 1 cavity to stack a burst of 5 pulses at low energies to using a multiplexed 4+4 cavity design to stack a burst of 81 pulses with a total energy in the multi-mJ range. This chapter will contain the experimental systems as well as the corresponding experimental results for each pulse stacking experiment that has been done. The finer details concerning the specific components used for each of these experiments as well as the experimental alignment techniques are located in the Appendix section 5.8.

5.2 One Cavity Experiment

The first proof-of-principle experiments on coherent pulse stacking amplification were accomplished using a single GTI cavity [31]. A benefit of initially using a single GTI cavity is that the mathematics for a single cavity are analytically solvable. This makes it easy to compare the theoretical formulas with the experimental results. We performed two sets of experiments using a single cavity. The first of those experiments utilized a CW laser, where the burst of pulses was carved out of the CW signal using an amplitude electro-optic modulator. The second experiment used a mode-locked laser as the seed and the stacking burst was formed by

modulating the amplitudes of the pulses from that laser after stretching. The experimental systems for the single GTI cavity experiments are shown below in Fig. 5.1.

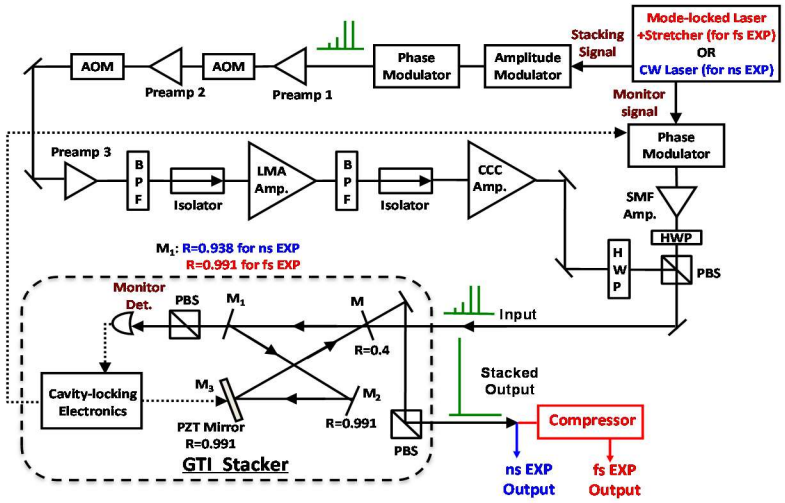

Figure 5.1: Experimental coherent pulse stacking amplification system with a single GTI

This experimental system starts out with either a CW laser or a mode-locked laser (both operating at a central wavelength near 1060nm) followed by a grating based pulse stretcher to stretch the 300fs pulses from the oscillator to 600ps. Those output pulses then proceed through an amplitude electro-optic modulator (EOM) followed by a phase electro-optic modulator. These devices serve to create the correct burst intensity and phase profile after amplification. The pulses then travel through a series of Yb-doped fiber amplifiers and acousto-optic modulators (AOM) in order to increase the energy of the pulses. The final amplifier is a 55µm core diameter chirally coupled core (CCC) fiber that can increase the burst energy up to 1.2mJ at a repetition rate of 10kHz. After amplification the pulses enter the GTI, as shown in Fig. 5.1, which utilizes a 40% reflectivity front mirror, which was chosen since it provides nearly the maximum peak power enhancement for a single cavity. The GTI is different for each of the seed sources, since the CW laser has a burst of pulses created at a repetition rate of 200MHz and the modelocked laser is operating with a repetition rate of 122MHz. For the case with the CW laser, all of the mirrors in the GTI are flat and the input beam size was chosen to have a 2.3mm radius

to make the effect of diffraction negligible. However for the mode-locked laser, mirror M_2 has a radius of curvature of 1.5m, and thus the input beam size was matched to the stable cavity mode with a beam radius of 0.7mm. The results of these experiments are shown below in Fig. 5.2.

In addition to the beam containing the pulses, an orthogonally polarized reference beam was used in the GTI cavity in order to stabilize its roundtrip length using the Pound-Drever-Hall technique (PDH) [32]. A portion of the beam was leaked through mirror M_1 in order to create the feedback signal for the PDH feedback electronics, which controlled the piezo-electric actuated mirror M_3.

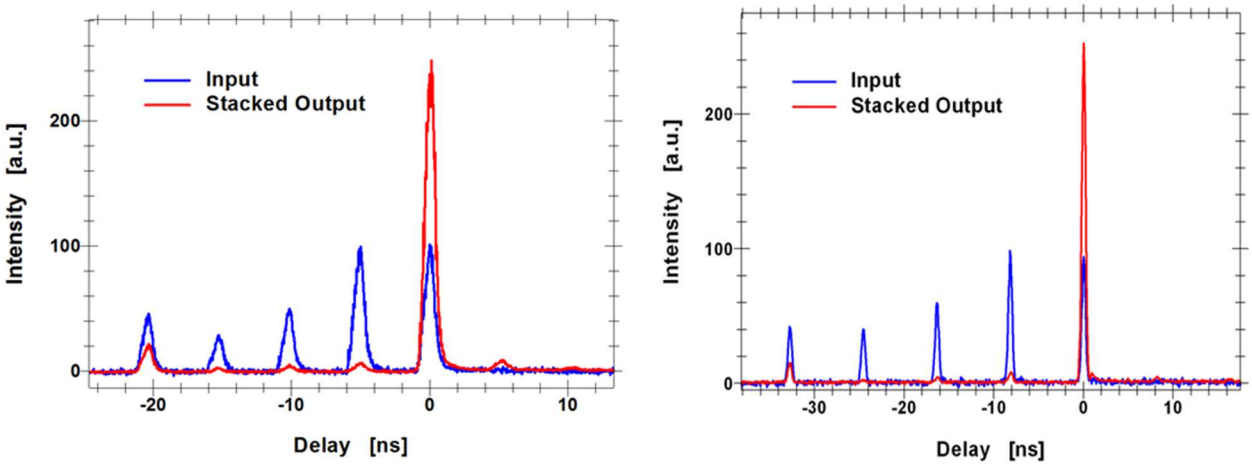

Figure 5.2: (left) Nanosecond single cavity pulse stacking experiment (right) Femtosecond single cavity pulse stacking experiment

This input pulse burst electric field profile can be derived for the given mirror reflectivity using the following formulas for a single cavity given in Eq. 5.1 for a burst containing 5 pulses [31]. Note that the minus sign for the final pulse means that a π phase shift is required from the phase modulator for that pulse.

$$ {}^{in}\vec{\tilde{A}} = \left[\frac{r^3}{\alpha^4}, (1-r^2)\frac{r^2}{\alpha^3}, (1-r^2)\frac{r}{\alpha^2}, (1-r^2)\frac{1}{\alpha}, -r \right] \tag{5.1} $$

As can be seen from Fig. 5.2, the pulse stacking for both the nanosecond pulses and the stretched femtosecond pulses resulted in an output stacked pulse with nearly all of the energy of

the input pulse burst. In the case of the nanosecond pulses, the pre-pulse contrast was measured to be better than 16dB and the stacking efficiency was measured to be 92%, which was limited by the finite mirror reflectivies in the cavity. In the case of the stretched femtosecond pulses, the pre-pulse contrast was measured to be better than 15dB and the stacking efficiency was measured to be 97%, again limited by the finite mirror reflectivities. For the femtosecond pulse stacking experiment, the autocorrelation trace was measured both before and after stacking. This autocorrelation trace is shown below in Fig. 5.3 and shows a 700fs pulse (with a 4nm bandwidth), with very little distortions introduced by the pulse stacking. No relevant energy scaling was performed using just a single cavity.

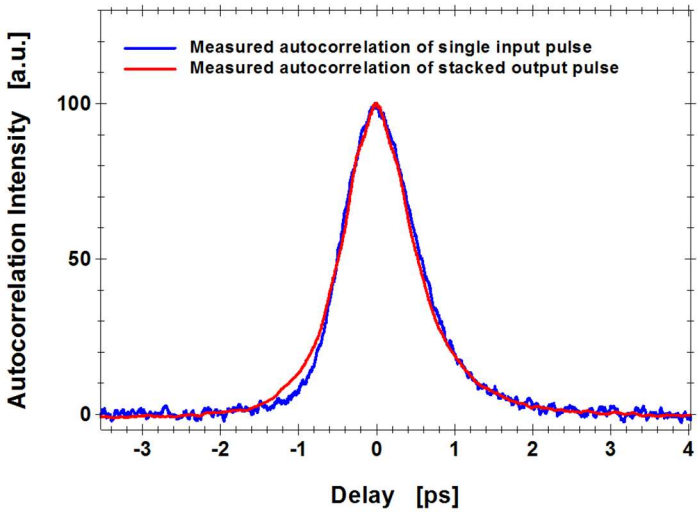

Figure 5.3: Autocorrelation trace before and after stacking for the femtosecond pulses

5.3 Two Cavity Experiment

After the initial proof-of-principle experiments with a single cavity, we moved to the first cascading experiments using two cavities. We again performed two sets of experiments using two cavities. The first of these experiments used the same 122MHz modelocked oscillator from the single cavity experiment [33], while the second used a 1GHz modelocked oscillator. The transition to the 1GHz oscillator allowed those cavities to be much shorter than for the 122MHz

experiment. The experimental systems for both the 122MHz experiment and the 1GHz experiment are shown below in Fig. 5.4.

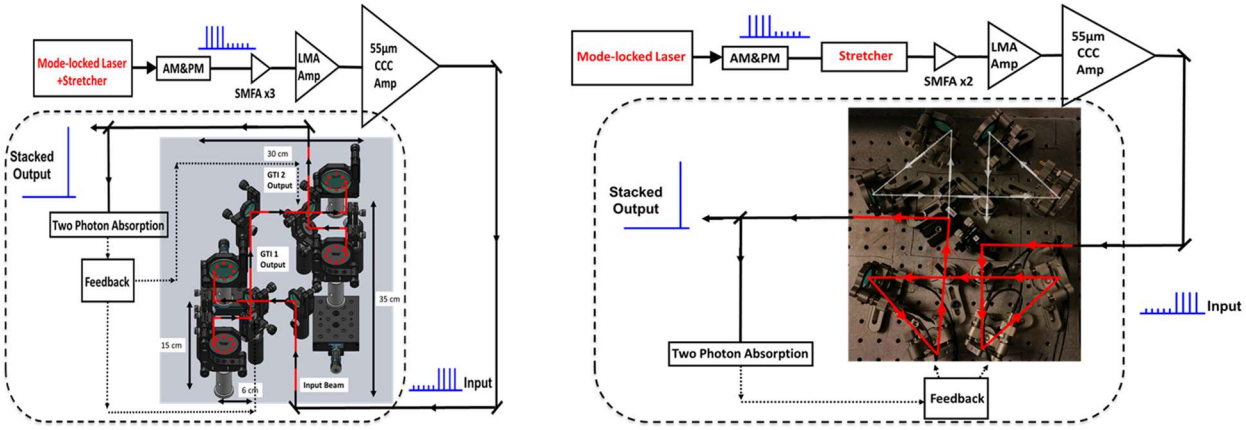

Figure 5.4: (left) Experimental system for the 122MHz oscillator, with the two GTIs represented using a 3D rendering of the actual setup. (right) Experimental system for the 1GHz oscillator, with the beam path through the actual GTIs used shown in the photograph

The experimental systems for the 122MHz and the 1GHz oscillator are very similar. The system for the 122MHz oscillator starts with the modelocked oscillator followed by the grating based stretcher and then the electro-optic modulators. For the 1GHz oscillator system, the electro-optic modulators come before the stretcher because once the pulses are stretched to around 600ps, as in the experiment, there is not enough time in between pulses to change the voltage value to the modulators. This is because the modulators are driven using arbitrary waveform generators (AWG), which have a bandwidth of 4GHz. The pulse bursts from each system then proceed through a series of Yb-doped fiber amplifiers and AOMs (not shown) before finally reaching the GTI pulse stackers. The GTIs for the 122MHz oscillator are arranged as Herriott cavities as in Fig. 5.4. The Herriott cell in the cavity consists of one flat mirror and one mirror with a radius of curvature of 1m. The mirror separation is 15cm and the beam hits each mirror of the Herriott cell 8 times before exiting. The GTIs for the 1GHz oscillator are arranged as triangular cavities with a roundtrip length of 30cm.

These GTIs were stabilized using a technique known as LOCSET (Locking of Optical Coherence via Single detector Electronic frequency Tagging) [34]. The LOCSET technique was implemented by measuring a signal sensitive to the peak intensity, which in this case was a two photon absorption signal (TPA). Each of the cavities was dithered at a specific frequency using the PZTs, and by mixing the TPA signal with one of those frequencies, a feedback signal for that specific cavity was generated, which was used to stabilize the roundtrip length of that cavity.

The simulated experimental input pulse burst for a cascade of two equal length GTIs is shown below in Fig. 5.5 along with the calculated pulse stacking output profile for that burst.

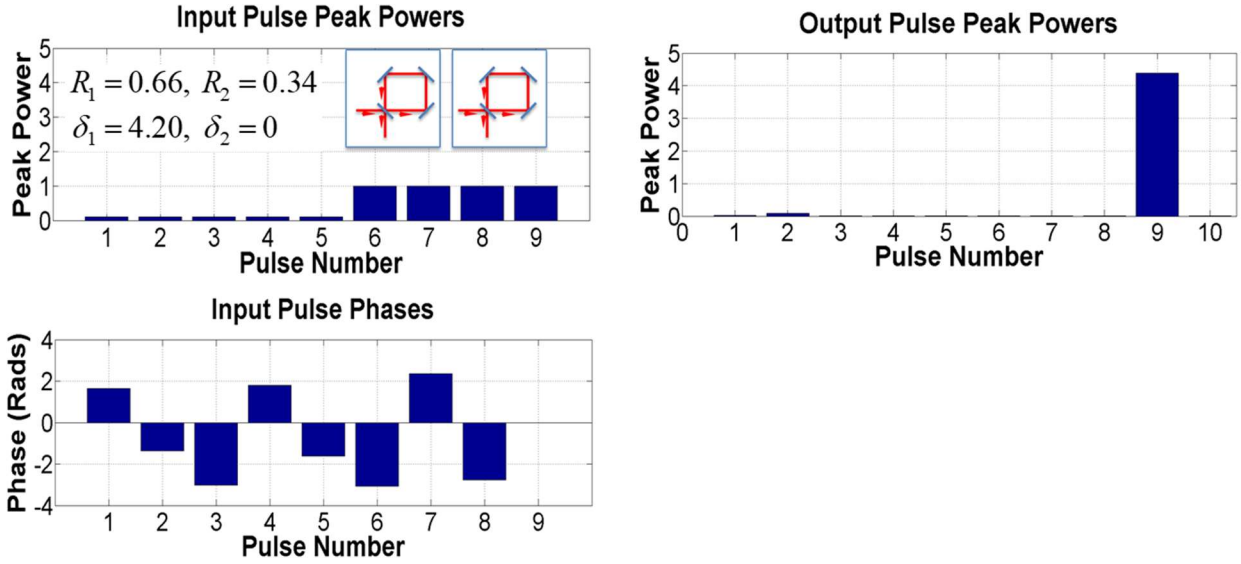

Figure 5.5: Simulated two cavity experimental pulse stacking

This simulation shows how a burst of 9 pulses with the final 4 pulses having equal intensity can be stacked into a single pulse, and this is the experiment that was performed. The experimental results for both the 122MHz oscillator stacking experiment and the 1GHz oscillator stacking experiment are shown below in Fig. 5.6.

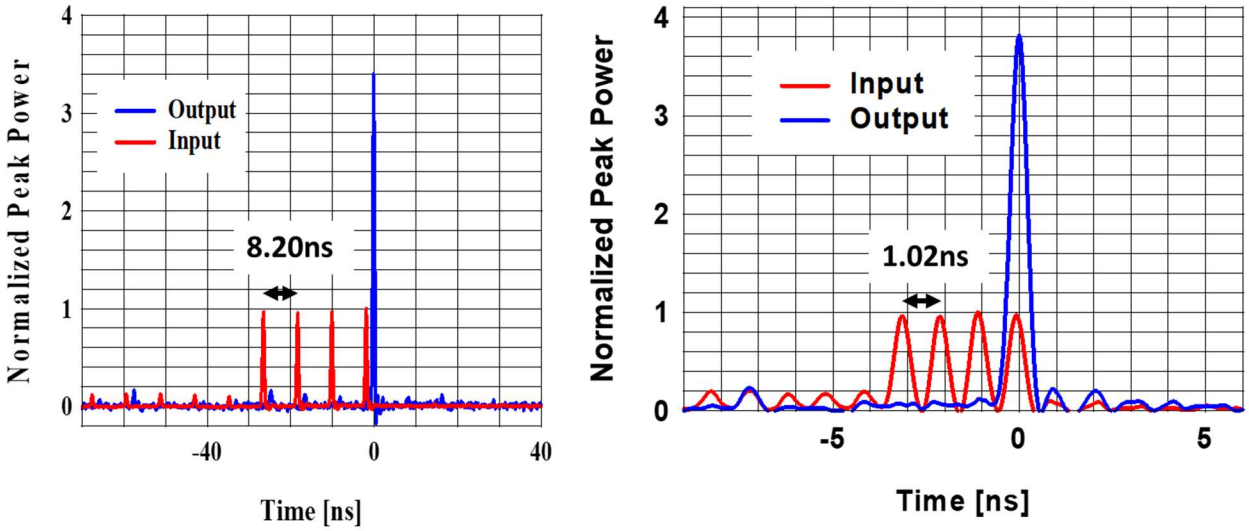

Figure 5.6: (left) Experimental results for the 122MHz pulse stacking using two cascaded Herriott cavities. (right) Experimental results for the 1GHz pulse stacking using two cascaded triangular cavities

These results show good agreement with the simulations and exhibit a reasonable pulse stacking fidelity. For the 122MHz experiment the pre-pulse contrast is measured to be better than 13dB with a pulse stacking efficiency of 75%. The stacking efficiency is limited in combination by the roundtrip loss through the Herriott cavities (since there are 19 mirror hits per roundtrip through the cavity) and by the imperfect pulse stacking (represented by the presence of pre-pulses and post-pulses). For the 1GHz experiment the pre-pulse contrast is measured to be better than 13dB as well with a pulse stacking efficiency of 85%. Since there are much fewer mirror hits in the 1GHz experiment, the average power through the system is much higher (95% power transmission), which contributes to the increased stacking efficiency. No energy scaling experiments were done with this two cavity configuration.

5.4 Four Cavity Experiment

The four cavity experiment was one of the key experiments performed, since pulse stacking using four cavities allows 9 approximately equal intensity pulses to be stacked, which is the backbone for proceeding further to 4+4 multiplexing experiments. The experimental system

for the four cavity experiment is shown below in Fig. 5.7 along with the arrangement of the 4 GTIs.

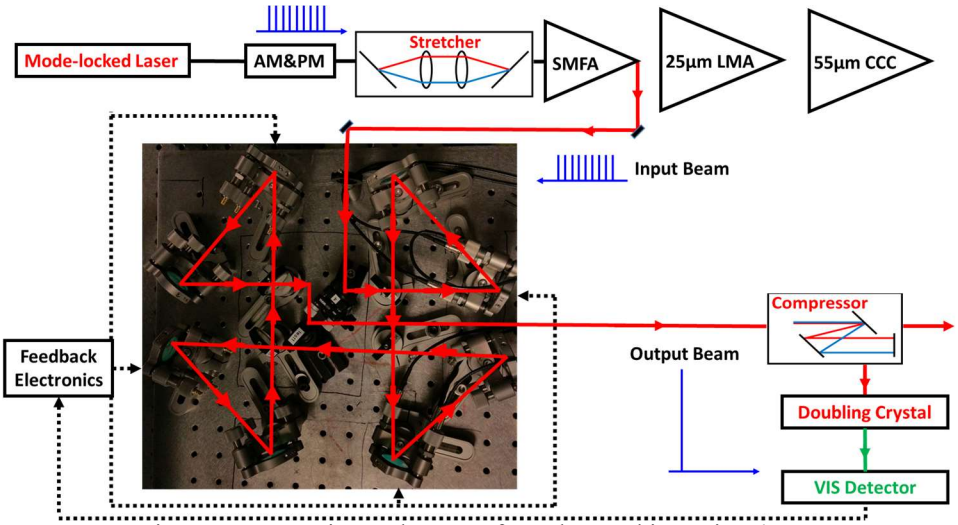

Figure 5.7: Experimental system for pulse stacking using 4 GTIs

The experimental system used for the four cavity pulse stacking experiments is very similar to the 1GHz experiments using two cavities. The system starts out with a 1GHz oscillator, and the pulse burst is immediately created by using the amplitude and phase modulators before being stretched by a grating based stretcher. The pulse burst then proceeds only through single mode fiber amplifiers, since this was designed as a proof-of-principle experiment, rather than an energy scaling one. The pulses are then stacked using the sequence of 4 triangular 0.3m long GTIs shown in Fig. 5.7 before being compressed. A fraction of the beam is taken from the compressor and used for second harmonic generation (SHG) in order to create a feedback signal to stabilize the roundtrip length of the cavities through the use of PZTs. The pulse stacking results can be seen below in Fig. 5.8 along with the simulated experimental conditions.

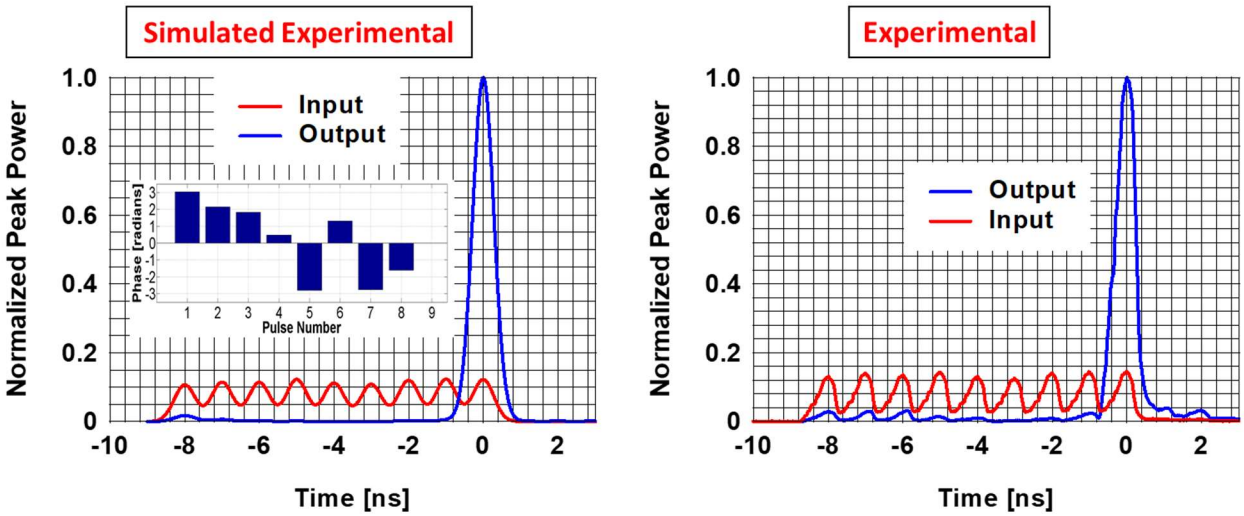

Figure 5.8: (left) Simulated experimental conditions for the input pulse intensity and phase profile for pulse stacking using 4 GTIs with reflectivities R_1=0.59, R_2=0.59, R_3=0.69, R_4=0.69 as measured along with optimal cavity phases of δ_1=4.66, δ_2=3.15, δ_3=5.46, δ_4=0

The pulse stacking result from Fig. 5.8 is in very good agreement with the simulated experimental conditions. The results show a pre-pulse contrast better than 16dB and a normalized stacking efficiency of 85%. Where the normalized stacking efficiency does not consider the average power loss through the cavities, which was measured to be 92%, and was dominated by the finite cavity mirror reflectivities. The small pre-pulses in Fig. 5.8 can most likely be attributed to an imperfect input phase profile. The autocorrelation trace both before and after pulse stacking was again measured for this cavity experiment and can be seen below in Fig. 5.9. These autocorrelation traces again show a negligible impact of the pulse stacking on the compressed pulse shape and duration. The deconvolved pulse duration for this autocorrelation trace is 330fs for the 7nm bandwidth measured spectrum.

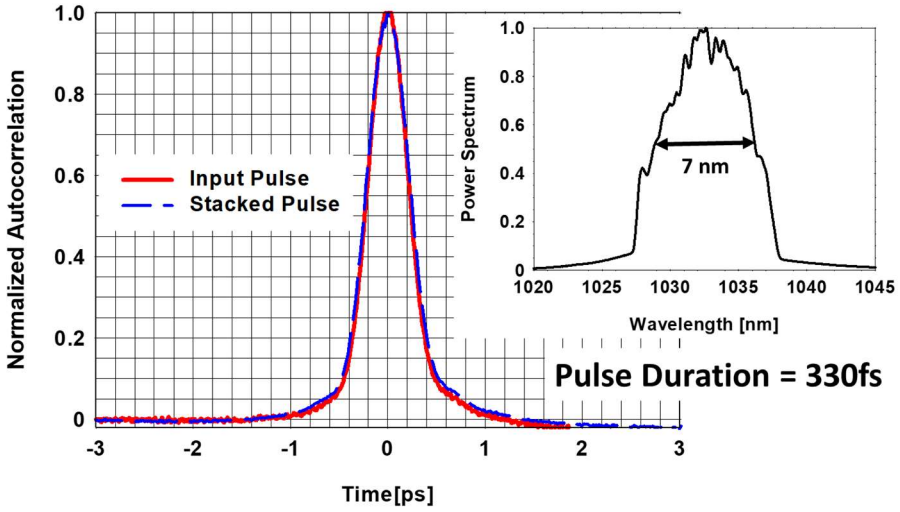

Figure 5.9: Autocorrelation traces before and after stacking using four cavities along with the power spectrum and the deconvolved pulse duration

These GTIs were stabilized using stochastic parallel gradient descent (SPGD), as discussed in Chapter 3, which was implemented using hardware from National Instruments. The stability of the pulse stacking was measured using the SHG signal, and was found to be stable for over one hour (only limited by stopping the measurement at that time). The stability results are shown below in Fig. 5.10 for a 15 minute measurement window. These results show that the SHG signal has a standard deviation of 3%, corresponding to a standard deviation in the stacked pulse intensity of only 1.5%.

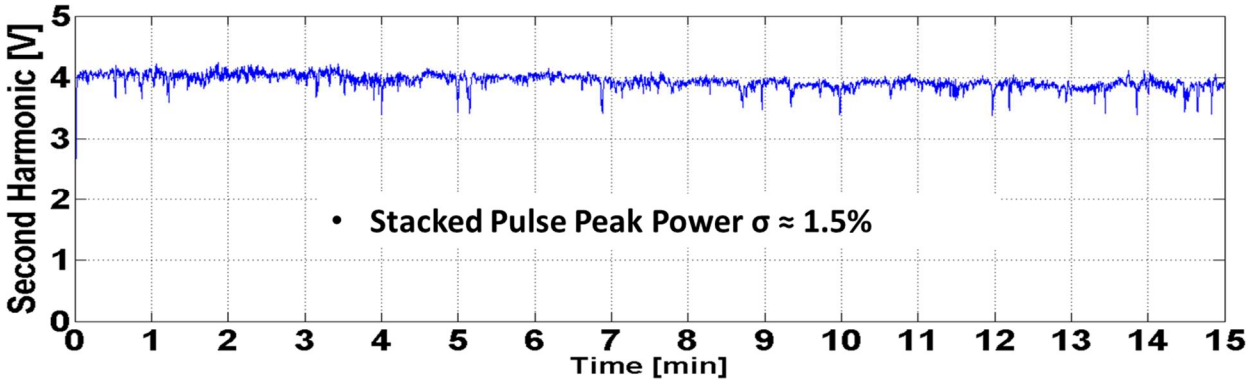

Figure 5.10: Four cavity pulse stacking stability test

5.5 Four + One Cavity Multiplexing Experiment

The next experiment performed used the same four cavities from section 5.4 and added an additional 9 times longer Herriott cavity onto the end in order to test multiplexing. Adding the additional cavity now allowed 27 nearly equal intensity pulses to be stacked. The experimental system for the four + one cavity multiplexing experiment is shown below in Fig. 5.11.

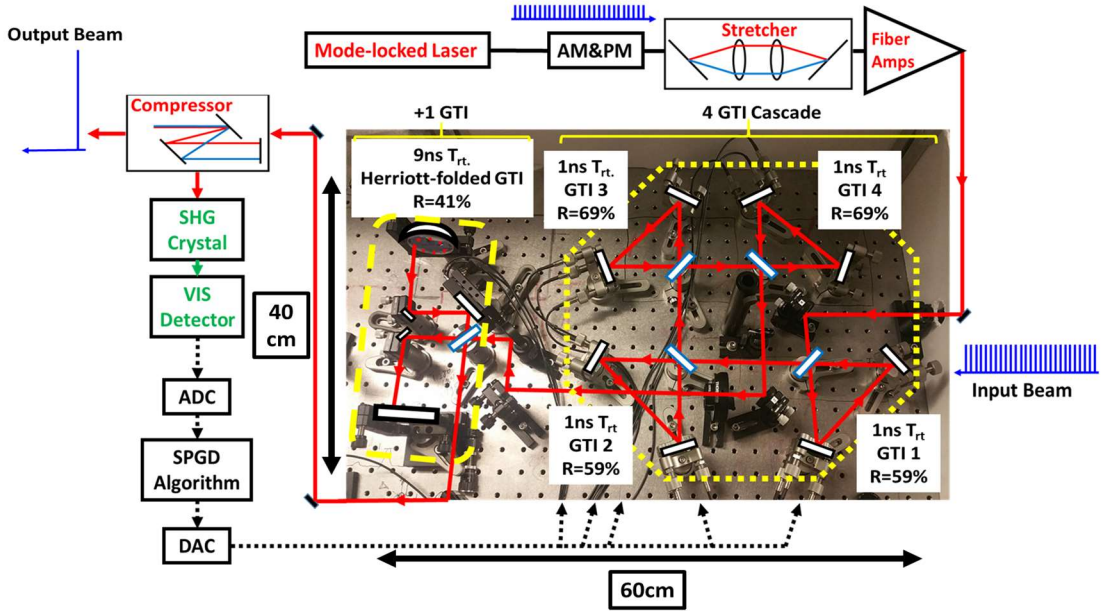

Figure 5.11: Four + one cavity multiplexing experimental setup

The experimental setup for the four + one cavity multiplexing experiment is nearly identical to that for the four cavity experiment, with the exception that an additional 2.7m long Herriott cavity is added to the end of the four cavity sequence. The Herriott cell in the cavity consists of one flat mirror and one mirror with a radius of curvature of 1m. The mirror separation is 18.7cm and the beam hits each mirror of the Herriott cell 7 times before exiting. The pulses from the 1GHz oscillator are phase and amplitude modulated, stretched, then amplified before being stacked by the configuration shown in Fig. 5.11 and compressed. SPGD based stabilization was set up, but not attempted on this configuration. The results from this

experiment are shown below in Fig. 5.12, which were optimized not by stabilizing, but simply through the Lissajous scan (discussed in section 3.3).

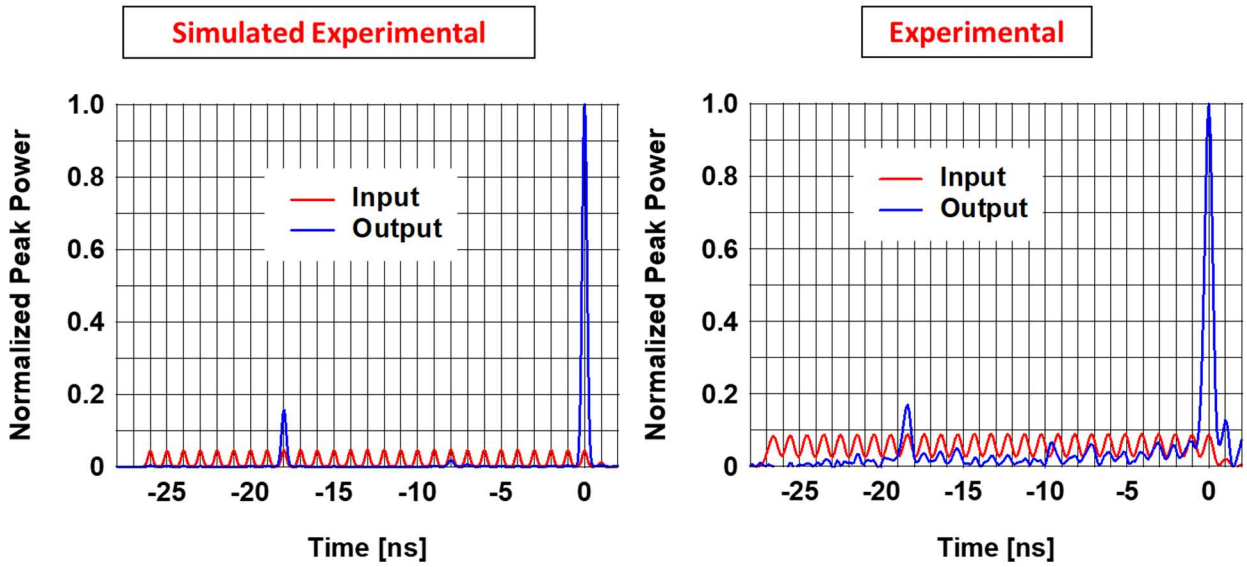

Figure 5.12: (left) Simulated experimental conditions for the input pulse intensity and phase profile for pulse stacking using the 4+1 cavity multiplex. (right) Experimental pulse stacking results for the 4+1 cavity multiplex

These results show good qualitative agreement between the simulated experiment and the measured results. The results show a pre-pulse contrast of 8dB, which is dominated by the large 9^{th} pulse in the output profile seen in both the simulation and in the experiment. The normalized stacking efficiency is roughly 50%, which is a result of not having the optimal cavity phase values, since stabilization was not performed. This experiment served simply as the first proof-of-principle demonstration of the concept of multiplexing different length GTIs in order to be able to stack much longer pulse bursts.

5.6 Four + Four Cavity Multiplexing Experiment

The final pulse stacking experiment performed used the same four 0.3m triangular cavities from section 5.3 and added an additional set of four 2.7m long Herriott cavities, whose Herriott cells are identical to the Herriott cell from the four + one cavity experiment from section

5.3. This configuration can allow 81 nearly equal intensity pulses to be stacked, as in Fig. 2.11. The experimental setup is shown below in Fig. 5.13.

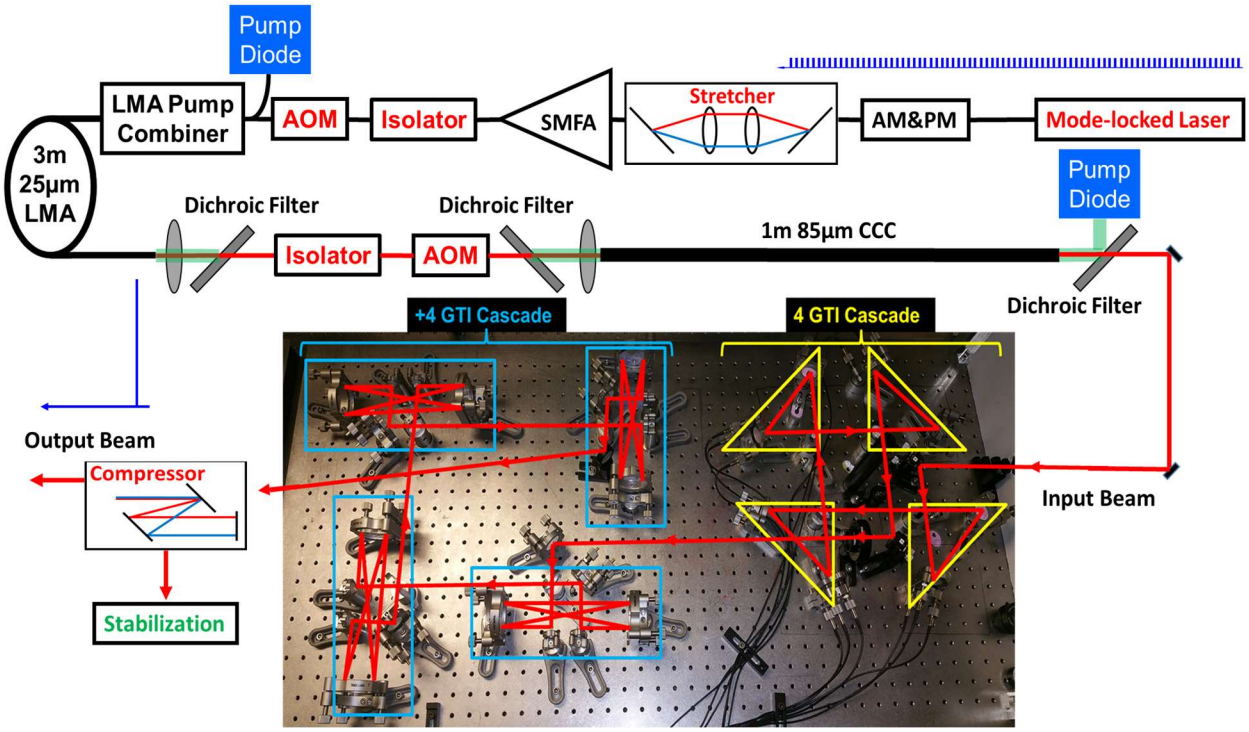

Figure 5.13: Four + four cavity multiplexing experimental setup

This experimental setup starts with the 1GHz oscillator, whose pulses are phase and amplitude modulated, stretched, amplified, stacked, and compressed. The power amplifier in this sequence consists of a 1 meter long 85µm core diameter CCC fiber which has a mode field diameter of roughly 40µm. The photograph in Fig. 5.13 shows the actual pulse stacking arrangement used for these experiments. SPGD based stabilization was attempted, but has been unsuccessful thus far in stabilizing these cavities. It is unclear what the primary reason for the failure of stabilization is, but at this time we believe it is most likely due to drift of the carrier frequency of the oscillator between pulse bursts. The experimental results are shown below in Fig. 5.14 for a low energy experiment done at a 1MHz repetition rate and in Fig. 5.15 for a multi-mJ experiment done at a 1kHz repetition rate, which were again optimized using the Lissajous scan and each result is accompanied by a simulation of the experimental conditions.

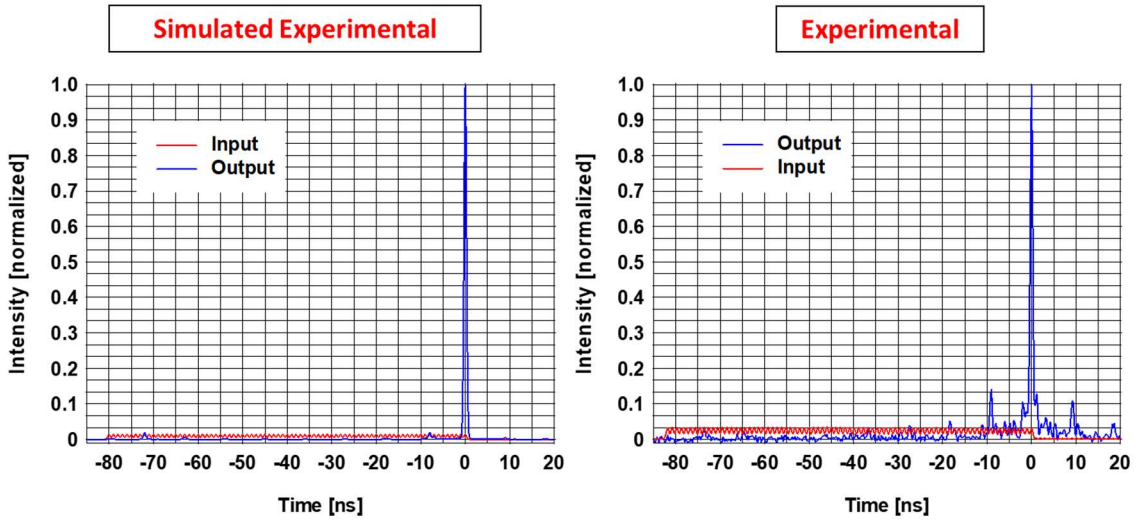

Figure 5.14: (left) Simulated experimental conditions for the input pulse intensity and phase profile for pulse stacking using 4+4 GTIs with reflectivities R1=0.59, R2=0.59, R3=0.69, R4=0.69, R5=0.59, R6=0.59, R7=0.69, R8=0.69 as measured along with optimal cavity phases of δ_1=4.66, δ_2=3.15, δ_3=5.46, δ_4=0, δ_5=4.66, δ_6=3.15, δ_7=5.46, δ_8=0. (right) Experimental pulse stacking results using 4+4 GTIs at 1MHz with low energy

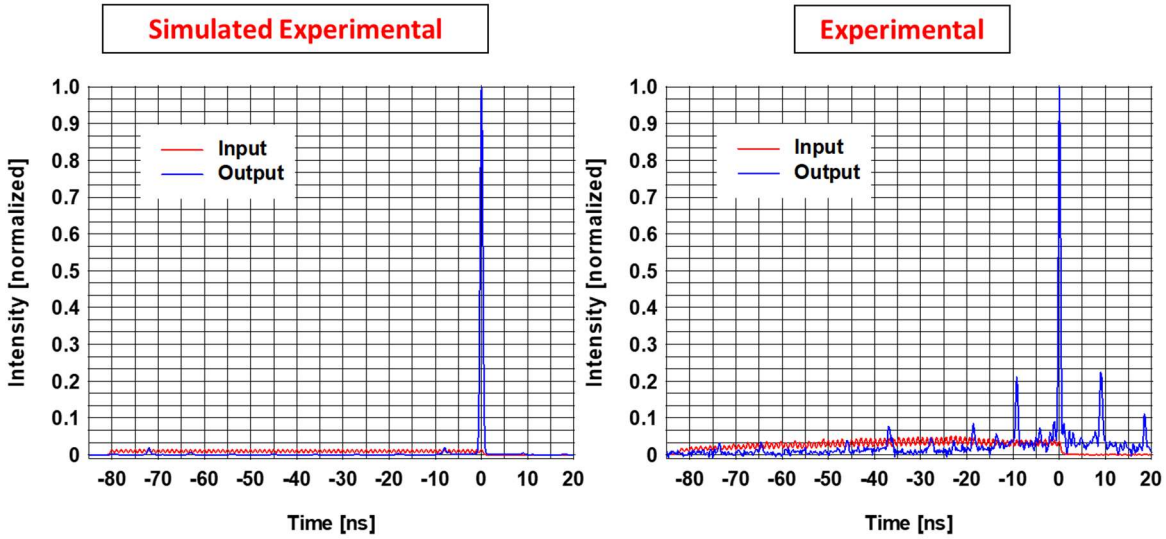

Figure 5.15: (left) Simulated experimental conditions for the input pulse intensity and phase profile for pulse stacking using 4+4 GTIs with reflectivities R_1=0.59, R_2=0.59, R_3=0.69, R_4=0.69, R_5=0.59, R_6=0.59, R_7=0.69, R_8=0.69 as measured along with optimal cavity phases of δ_1=4.66, δ_2=3.15, δ_3=5.46, δ_4=0, δ_5=4.66, δ_6=3.15, δ_7=5.46, δ_8=0. (right) Experimental pulse stacking results using 4+4 GTIs at 1kHz with 2mJ total burst energy

These results show quite good qualitative agreement between the simulated experimental conditions and the experimental results. In the case of the 1MHz stacking, a pre-pulse contrast of 9dB and a normalized stacking efficiency of 37% is measured. For the 1 kHz stacking with 2mJ of energy, a pre-pulse contrast of 7dB and a normalized stacking efficiency of 35% is measured. These results are primarily limited by the lack of stabilization, since the pulse

stacking is very sensitive to errors in the cavity phase as seen in Fig. 2.12. For pulse stacking in the mJ range at 1kHz, experiments were also done at 1mJ and 3mJ of total burst energy, with a negligible difference in the stacking fidelity noticed for those energies.

5.7 Energy Extraction Experiment

In addition to pulse stacking, several experiments were performed to characterize the maximum energy extractable from the 85µm CCC fibers used. The characterization relied on measuring the small signal gain at various pump power levels as well as measuring the total output energy as a function of the input energy at those same pump power levels. This data was used in combination with the Franz-Nodvick theory in order to determine the saturation energy of the amplifier. The results of this analysis are shown below in Fig. 5.16, which predict a saturation energy of 1mJ for this fiber amplifier.

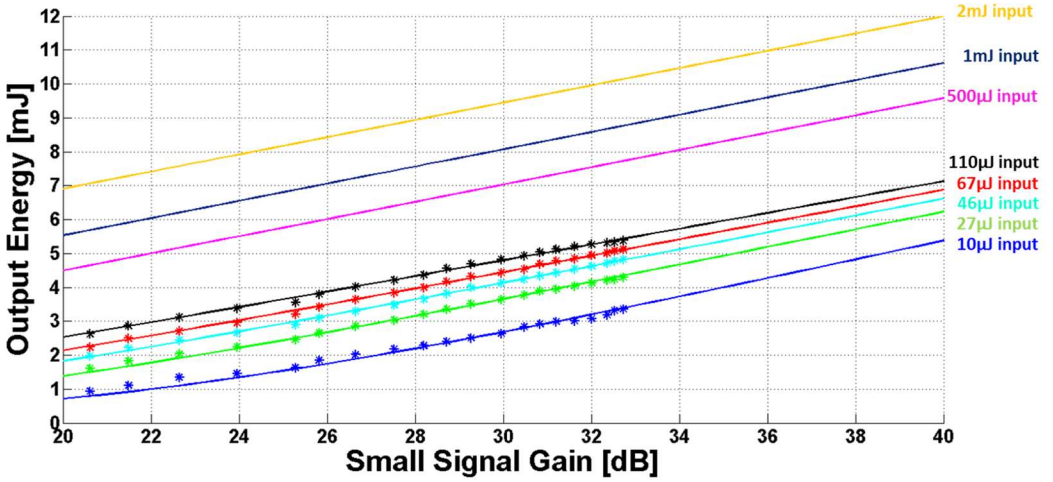

Figure 5.16: 85µm core diameter 1m long CCC fiber energy extraction with measured data shown as asterisks and calculations using Franz-Nodvick theory with a 1mJ saturation energy shown as solid lines

These results show good agreement between the measured data and the predictions from the Franz-Nodvick theory assuming a saturation energy of 1mJ. Predictions for the required input energy in order to achieve more output energy are also included in Fig. 5.16. Further energy extraction experiments were also performed using a different 1.2 meter long 85µm core

diameter CCC fiber to show that energies up to 10mJ can be obtained using these fibers as seen in Fig. 5.17.

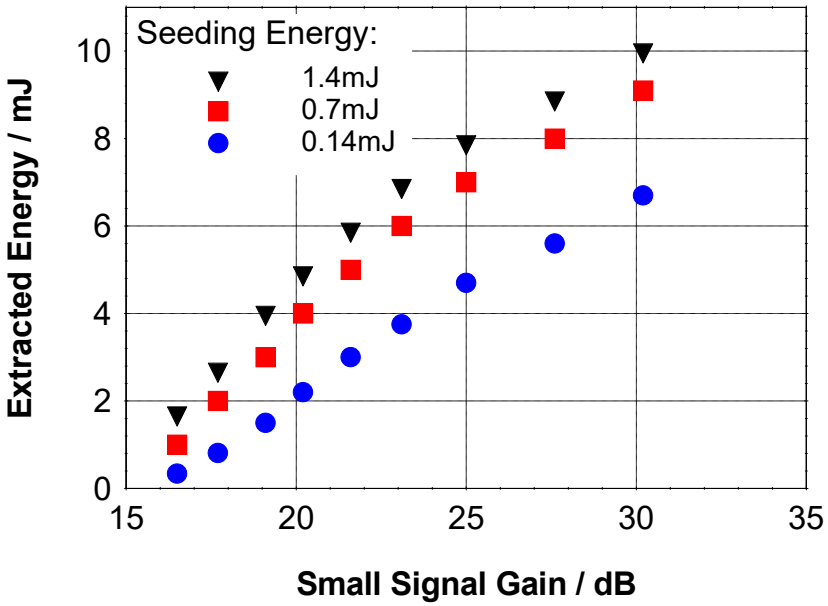

Figure 5.17: 85µm core diameter 1.2m long CCC fiber energy extraction data

Additionally the input and output 81 pulse bursts were measured to show the effect of saturation on the burst profile. The input pulse bursts were tailored so that the output pulse burst would have a shape that has a nearly constant peak nonlinear phase across the burst, as discussed in section 2.7. These input and output bursts are shown below in Fig. 5.18 along with the target burst shape for 10mJ output energy calculated using Eq. 2.14 assuming a mode field diameter of 40µm (similar to what was measured for this fiber).

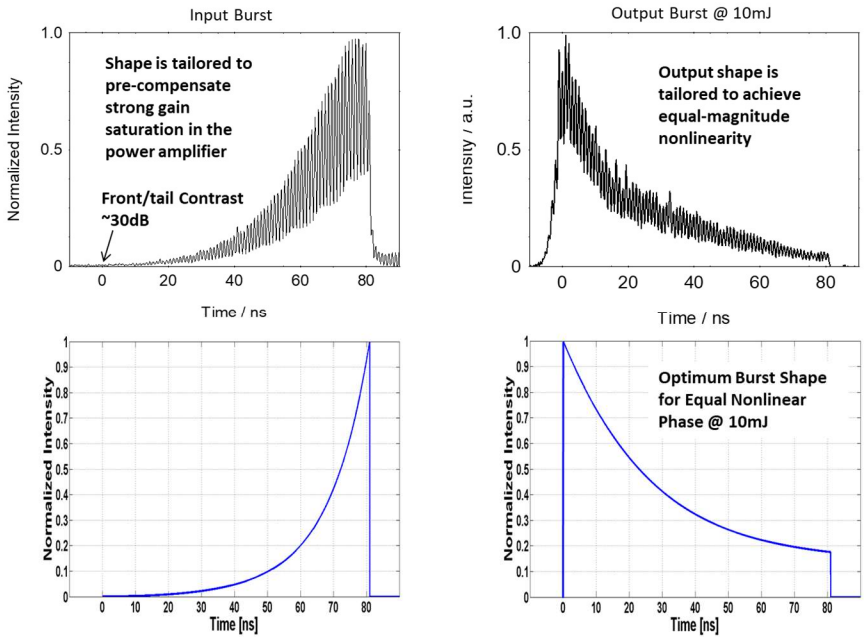

Figure 5.18: (top left) Measured input burst profile designed to compensate the gain saturation by having the first pulse in the burst have 1000 times less energy than the final pulse. (top right) Measured output burst profile with 10mJ of energy tailored to achieve a constant nonlinear phase across the burst. (bottom left) Calculated optimal input burst profile (bottom right) Calculated optimal output burst profile with 10mJ of energy to achieve a constant nonlinear phase across the burst of 5 radians

These results show that a pulse burst with a total energy of 10mJ can be created. The burst is designed to have an equal nonlinear phase, and further experiments are needed to confirm that this is indeed the case.

5.8 Appendix: Experimental Components Details and Alignment Techniques

The details about the experimental components used for the experiments performed are included in this section. Additionally a description of the spatial and temporal alignment techniques for the interferometers is described.

There were three laser sources used in the various pulse stacking experiments, and those were the CW laser, a 122MHz modelocked laser, and a 1GHz modelocked laser. The CW laser was a Toptica DL 100 tunable single frequency diode laser with a central wavelength of 1064nm. The 122MHz modelocked laser was modelocked using a semiconductor saturable absorber mirror (SESAM) and was based on diode pumped Nd:glass in order to produce 300fs pulses with

a bandwidth of 4.5nm at a central wavelength of 1054nm. The 1GHz modelocked fiber laser relied on nonlinear polarization evolution (NPE) in order to generate slightly chirped 146fs output pulses with a bandwidth of 20nm.

For the electro-optic modulators used in these experiments, more care needed to be taken with the amplitude modulator, and the phase modulator only needed a sufficient bandwidth to be able to modulate each pulse individually (>1GHz). The phase modulator was a 10GHz fiber coupled electro-optic modulator from EOSpace, and was thus sufficient. The amplitude modulator needed to not only have a sufficient bandwidth, but also be arranged as a push-pull Mach-Zehnder interferometer so as not to imprint an amplitude dependent phase on the pulse burst. The amplitude modulator also required a bias voltage to be applied, and ideally this bias voltage would be controlled with a feedback loop since it does drift slowly over time. For these experiments the Jenoptik AM1064 was used and provided sufficient extinction (>30dB).

The amplitude and phase electro-optic modulators were each driven by a separate arbitrary waveform generator (AWG). An AWG was required because the amplitude and phase profiles needed were quite complicated and individual control over the values for each pulse was necessary. The AWGs used were from Chase Scientific and were the da14000 for the amplitude modulator and the dax14000 for the phase modulator and each allowed for generation of new data points at 4 Giga samples per second. It should also be noted that an advanced timing system was developed for these components, since synchronization with the laser pulses was critical to their operation.

The two photon absorption (TPA) detector and the visible detector were each based on GaAsP photodiodes. These diodes were chosen due to the fact that they have a strong response near 500nm and also they have a sharp cutoff in the photosensitivity near 700nm, and thus will

not produce a signal for the 1μm laser pulses unless it is a TPA signal. In order to generate the TPA signal, the GaAsP photodiodes were used without biasing and thus had rise times longer than the burst duration and so effectively integrated the TPA signal over the duration of the burst. When used to detect the second harmonic signal, the diodes were biased, but still the rise time was much longer than the burst duration (rise time >1μs). Also in order to generate the second harmonic signal, a barium beta borate (BBO) crystal was used.

In order to stabilize the roundtrip length of the cavities, piezo-actuated mirror mounts were used. The mirror mounts used were the piezo-actuated Polaris series mirror mounts from Thorlabs, which were calculated to have sufficient bandwidth (~1kHz) for the small distance changes (<1μm) that were required.

Interferometric alignment of the GTIs was needed both spatially and temporally. The tools used to accomplish this task were a pair of CCD cameras, an iris, a 10GHz photodiode, and a 40GHz oscilloscope. A schematic of a typical setup for this alignment is given below in Fig. 5.19.

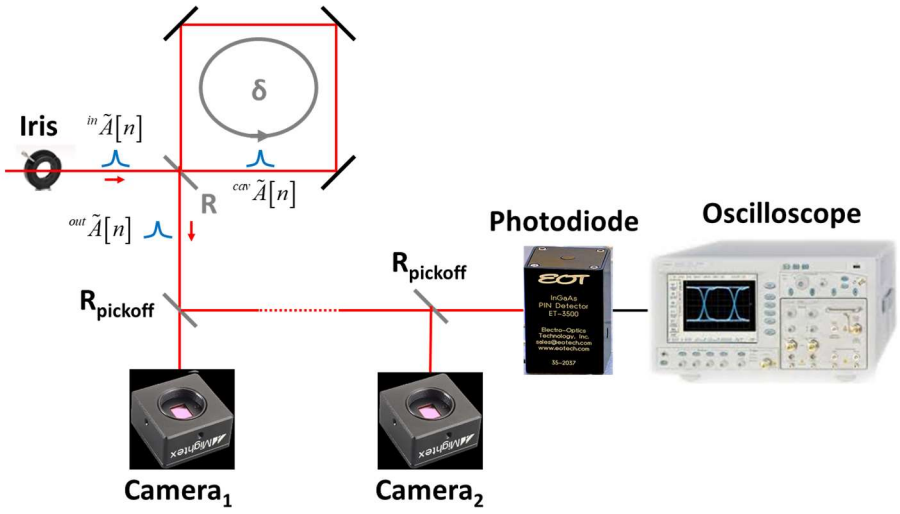

Figure 5.19: Interferometric alignment setup for spatial and temporal alignment. The dotted line represents a large propagation distance.

Spatial overlap of two optical beams (e.g. the reflected beam from the cavity and the transmitted beam from the cavity) was accomplished by ensuring that the two beams overlap perfectly at two locations in space, since two points define a straight line. The first point of overlap was chosen to be a small distance after reflection from the partially reflecting mirror of the cavity, and so a portion of the beam was picked off at that point. The second point of overlap was then chosen to be a large distance after reflection from the partially reflecting mirror, so another portion of the beam was picked off at that point. The remaining beam then proceeded to the 10GHz photodiode, whose output was connected to the 40GHz scope.

In order to ensure the reflected beam and the transmitted beam overlapped at Camera_1, the orifice of the iris was chosen so that the spot size at Camera_1 was minimized, which gives the best spatial resolution. Then the intracavity mirror directly after the partial reflector was adjusted so that the reflected beam and the transmitted beam perfectly overlapped on Camera_1. This procedure was then repeated for Camera_2, but now the intracavity mirror directly before the partial reflector was adjusted. By adjusting only these two mirrors, the two beams could be made to overlap at both Camera_1 and Camera_2, thus the two beams were spatially overlapped.

Once the initial spatial alignment of the beams was accomplished, the roundtrip time of the GTI had to be matched to the oscillator (or an integer number of oscillator periods). This was accomplished by first sending just a single pulse into the cavity and measuring the temporal spacing of the ring down pulses to know the temporal length of the cavity. Then the cavity was blocked and two pulses were sent through the system into the photodiode to get a measure of the temporal length of the oscillator. The roundtrip length of the cavity was then adjusted to be as close to that of the oscillator as possible. After that, the two pulse sequence was sent through the system with the cavity unblocked and temporal beating of the stretched pulses was observed on

the scope. This can be attributed to spectral beating that manifests itself in the time domain because the pulses are strongly chirped. The final roundtrip length adjustment was accomplished by maximizing the beating period, which also optimized the interference of the two pulses. After this final roundtrip length adjustment was made, the full oscillator repetition rate was sent through the system with the cavity unblocked. If there was any angular misalignment, it would manifest itself as spatial beating on $Camera_2$, and would need to be eliminated by adjusting the intracavity mirror directly before the partial reflector.

Chapter 6 Conclusions and Future Work

6.1 Conclusions

This thesis focused on developing the theoretical and experimental foundations of coherent pulse stacking amplification, which is a time domain coherent combining technique that can help achieve Joule level energy laser pulses at multi-kHz repetition rates. The analytical tools needed to understand and control this technique are developed. In addition an analysis of the stochastic parallel gradient descent (SPGD) algorithm as it pertains to stabilizing optical cavities is presented. An analysis of the various properties and requirements of the optical cavities is presented for both time and space considerations. The first experiments performed demonstrating the efficacy of coherent pulse stacking amplification for pushing the boundary of what is possible with fiber amplifiers is also presented.

The analysis of coherent pulse stacking amplification shows that bursts of over 80 pulses can be coherently stacked into a single pulse and the requirements on both the pulse burst and the stackers is developed. The underlying theoretical analysis for coherent pulse stacking amplification starts from the simple consideration of a single pulse propagating through a series of lossless Gires-Tournois interferometers and creating a burst of pulses on the other side. Then due to time reversal symmetry of such a system, the output burst can be time reversed, complex conjugated, and propagated back through the same series of interferometers in order to recombine back into a single pulse. This analysis puts the constraint on that burst of pulses that the intensity in the spectral domain must be equal to that for the single pulse. Furthermore, the

required sequence of interferometers required to stack such a burst of pulses can be obtained from the burst profile itself in order to aid the design of such a system. Optimized burst profiles are also presented that have an equal nonlinear phase across the burst. The tolerances and time domain requirements for the interferometers are also presented.

An optimization plus stabilization procedure is presented in order to ensure the optical cavity phases get to and stay at the correct values even in the presence of environmental noise sources. A detector sensitive to peak intensities is proposed to create the feedback signal necessary for the optimization and stabilization. A coarse search based on a Lissajous pattern is proposed since the peak intensity signal measured by the detector contains many undesirable local maxima. An analysis of the stochastic parallel gradient descent (SPGD) technique in the presence of noise is presented and an optimal set of parameters for this algorithm are presented as well as a requirement on the maximum allowable noise between successive measurements.

Two different kinds of optical cavities are analyzed and various requirements on each of these cavities is presented. Optical cavities containing only flat mirrors are considered and input beam size requirements are given for cavities that are 0.3m and 2.7m long, which are of most interest for CPSA. An analysis of Herriott cells is presented and the applicability of these Herriott cells is analyzed in the context of CPSA, showing that they can be used to make very long interferometers in a very compact arrangement.

Coherent pulse stacking amplification experiments have been performed from a single cavity with 5 pulses at low energy to a 4+4 cavity multiplex with 81 pulses at multi-mJ energies in order to demonstrate the feasibility of this technique. Experiments with this wide range of cavity configurations provides very good agreement with the theoretical predictions, thus verifying that this technique works as predicted. Experiments including up to 81 pulses with a

total burst duration over 81ns are shown being able to extract more than 10mJ of energy from a single fiber with a burst profile designed to have a constant nonlinear phase, which is more than two orders of magnitude beyond what is allowable by CPA.

6.2 Future Work

There are several avenues of research to be explored to increase the pulse energy extractable from a single fiber. Further stabilization and optimization methods based on field programmable gate arrays (FPGA) can allow for simultaneous cavity phase stabilization and optimization of the input stacking burst profile at high speeds (>1kHz). By utilizing a high peak power high brightness pulsed pumping scheme, the amount of extractable energy from these large core fibers can be increased beyond the total amount of stored energy.

Coherent spatial combining and/or coherent spectral combining can be used in combination with coherent pulse stacking amplification in order to create high energy high average power laser sources, and further investigation into this area of research should be done.

Appendix: List of Publications

Journal Papers:

1. Zhou, Tong, John Ruppe, Cheng Zhu, I-Ning Hu, John Nees, and Almantas Galvanauskas. "Coherent pulse stacking amplification using low-finesse Gires-Tournois interferometers." *Optics Express* 23, no. 6 (2015): 7442-7462.

Conference Papers:

1. Pei, Hanzhang, John Ruppe, Siyun Chen, John Nees, and Almantas Galvanauskas. "Multi-mJ Ultrashort Pulse Coherent Pulse Stacking Amplification in a Yb-doped 85μm CCC Fiber Based System." In *CLEO: Science and Innovations*, pp. SM1L-2. Optical Society of America, 2017.

2. Ruppe, John, Siyun Chen, Morteza Sheikhsofla, Russell Wilcox, John Nees, and Almantas Galvanauskas. "Multiplexed Coherent Pulse Stacking of 27 Pulses in a 4+ 1 GTI Resonator Sequence." In *Advanced Solid State Lasers*, pp. AM4A-6. Optical Society of America, 2016.

3. Ruppe, John, Siyun Chen, Tong Zhou, Morteza Sheikhsofla, Zhigang Zhang, Guoqing Chang, Franz Kärtner, John Nees, and Almantas Galvanauskas. "Coherent pulse stacking extension of CPA to 9ns effectively-long stretched pulse duration." In *Lasers and Electro-Optics (CLEO), 2016 Conference on*, pp. 1-2. IEEE, 2016.

4. Ruppe, John, Tong Zhou, Cheng Zhu, John Nees, Russell Wilcox, and Almantas Galvanauskas. "Cascading of Coherent Pulse Stacking Using Multiple Gires-Tournois Interferometers." In *Advanced Solid State Lasers*, pp. AW3A-4. Optical Society of America, 2015.

Bibliography

[1] "Nobel Prize in Physics 1964 - Presentation Speech". *Nobelprize.org.* Nobel Media AB 2014. Web. 12 Aug 2017.http://www.nobelprize.org/nobel_prizes/physics/laureates/1964/press.html

[2] Strickland, Donna, and Gerard Mourou. "Compression of amplified chirped optical pulses." *Optics communications* 55, no. 6 (1985): 447-449.

[3] Bahk, S-W., Pascal Rousseau, T. A. Planchon, Vladimir Chvykov, Galina Kalintchenko, Anatoly Maksimchuk, G. A. Mourou, and Victor Yanovsky. "Generation and characterization of the highest laser intensities (10 22 W/cm 2)." *Optics letters* 29, no. 24 (2004): 2837-2839.

[4] Chu, Yuxi, Zebiao Gan, Xiaoyan Liang, Lianghong Yu, Xiaoming Lu, Cheng Wang, Xinliang Wang et al. "High-energy large-aperture Ti: sapphire amplifier for 5 PW laser pulses." *Optics letters* 40, no. 21 (2015): 5011-5014.

[5] Limpert, Jens, Fabian Stutzki, Florian Jansen, Hans-Jürgen Otto, Tino Eidam, Cesar Jauregui, and Andreas Tünnermann. "Yb-doped large-pitch fibres: effective single-mode operation based on higher-order mode delocalisation." *Light: Science and applications* 1 (2012): e8.

[6] Ma, Xiuquan, Cheng Zhu, I-Ning Hu, Alex Kaplan, and Almantas Galvanauskas. "Single-mode chirally-coupled-core fibers with larger than 50μm diameter cores." *Optics express* 22, no. 8 (2014): 9206-9219.

[7] Pei, Hanzhang, John Ruppe, Siyun Chen, John Nees, and Almantas Galvanauskas. "Multi-mJ Ultrashort Pulse Coherent Pulse Stacking Amplification in a Yb-doped 85μm CCC Fiber Based System." In *CLEO: Science and Innovations*, pp. SM1L-2. Optical Society of America, 2017.

[8] Jain, D., Y. Jung, Martin Nunez-Velazquez, and J. K. Sahu. "Extending single mode performance of all-solid large-mode-area single trench fiber." *Optics express* 22, no. 25 (2014): 31078-31091.

[9] Stutzki, Fabian, Florian Jansen, Andreas Liem, Cesar Jauregui, Jens Limpert, and Andreas Tünnermann. "26 mJ, 130 W Q-switched fiber-laser system with near-diffraction-limited beam quality." *Optics letters* 37, no. 6 (2012): 1073-1075.

[10] He, Wenbin, Martin Leich, Stephan Grimm, Jens Kobelke, Yuan Zhu, Hartmut Bartelt, and Matthias Jäger. "Very large mode area ytterbium fiber amplifier with aluminum-doped pump cladding made by powder sinter technology." *Laser Physics Letters* 12, no. 1 (2014): 015103.

[11] Fermann, Martin E., Almantas Galvanauskas, and Gregg Sucha, eds. *Ultrafast lasers: Technology and applications*. Vol. 80. CRC Press, 2002.

[12] Agrawal, Govind P. *Nonlinear fiber optics*. Academic press, 2007.

[13] Boyd, Robert W. *Nonlinear optics*. Academic press, 2003.

[14] Siegman, Anthony E.. *Lasers*. : University Science Books, 1986.

[15] Webster, S., F. C. McDonald, A. Villanger, M. J. Soileau, E. W. Van Stryland, D. J. Hagan, B. McIntosh, W. Torruellas, J. Farroni, and K. Tankala. "Optical damage measurements for high peak power ytterbium doped fiber amplifiers." In *Proc. SPIE*, vol. 5991, p. 599115. 2005.

[16] Treacy, Edmond. "Optical pulse compression with diffraction gratings." *IEEE Journal of quantum Electronics* 5, no. 9 (1969): 454-458.

[17] Leemans, Wim, and Eric Esarey. "Laser-driven plasma-wave electron accelerators." *Phys. Today* 62, no. 3 (2009): 44-49.

[18] Sistrunk, Emily F., Thomas Spinka, Andrew Bayramian, Paul Armstrong, Salmaan Baxamusa, Shawn Betts, Darrell Bopp et al. "All Diode-Pumped, High-repetition-rate Advanced Petawatt Laser System (HAPLS)." In *CLEO: Science and Innovations*, pp. STh1L-2. Optical Society of America, 2017.

[19] Fomin, V., M. Abramov, A. Ferin, A. Abramov, D. Mochalov, N. Platonov, and V. Gapontsev. "10 kW single mode fiber laser." In *SyTu-1.3, Symposium on High-Power Fiber Lasers, 14th International Conference, Laser Optics*. 2010.

[20] Ferin, A., V. Gapontsev, E. Shcherbakov, V. Fomin, A. Unt, S. Maryashin, A. Abramov, and M. Abramov. "Multi-kilowatt average power nano pulse fiber lasers." In *Laser Optics, 2014 International Conference*, pp. 1-1. IEEE, 2014.

[21] Mourou, Gerard, Bill Brocklesby, Toshiki Tajima, and Jens Limpert. "The future is fibre accelerators." *Nature Photonics* 7, no. 4 (2013): 258-261.

[22] Kienel, Marco, Arno Klenke, Steffen Hädrich, Tino Eidam, Jens Limpert, and Andreas Tünnermann. "Divided-Pulse Amplification for High Energy Extraction." In *Advanced Solid State Lasers*, pp. ATu3A-09. Optical Society of America, 2013.

[23] Breitkopf, Sven, Stefano Wunderlich, Tino Eidam, Evgeny Shestaev, Simon Holzberger, Thomas Gottschall, Henning Carstens, Andreas Tünnermann, Ioachim Pupeza, and Jens Limpert. "Extraction of enhanced, ultrashort laser pulses from a passive 10-MHz stack-and-dump cavity." *Applied Physics B* 122, no. 12 (2016): 297.

[24] Ristau, Detlev, ed. *Laser-induced damage in optical materials*. CRC Press, 2014.

[25] Gerchberg, Ralph W. "A practical algorithm for the determination of the phase from image and diffraction plane pictures." *Optik* 35 (1972): 237-246.

[26] Phillips, Charles L., John M. Parr, and Eve A. Riskin. *Signals, systems, and transforms*. Prentice Hall, 1995.

[27] Vorontsov, Mikhail A., and V. P. Sivokon. "Stochastic parallel-gradient-descent technique for high-resolution wave-front phase-distortion correction." *JOSA A* 15, no. 10 (1998): 2745-2758.

[28] Press, W. H.; Flannery, B. P.; Teukolsky, S. A.; and Vetterling, W. T. "Sherman-Morrison Formula." In *Numerical Recipes in FORTRAN: The Art of Scientific Computing, 2nd ed.* Cambridge, England: Cambridge University Press, pp. 65-67, 1992.

[29] Herriott, Donald R., and Harry J. Schulte. "Folded optical delay lines." *Applied Optics* 4, no. 8 (1965): 883-889.

[30] Sennaroglu, Alphan, and James G. Fujimoto. "Design criteria for Herriott-type multi-pass cavities for ultrashort pulse lasers." *Optics Express* 11, no. 9 (2003): 1106-1113.

[31] Zhou, Tong, John Ruppe, Cheng Zhu, I-Ning Hu, John Nees, and Almantas Galvanauskas. "Coherent pulse stacking amplification using low-finesse Gires-Tournois interferometers." *Optics Express* 23, no. 6 (2015): 7442-7462.

[32] Drever, R. W. P., John L. Hall, F. V. Kowalski, J_ Hough, G. M. Ford, A. J. Munley, and H. Ward. "Laser phase and frequency stabilization using an optical resonator." *Applied Physics B* 31, no. 2 (1983): 97-105.

[33] Ruppe, John, Tong Zhou, Cheng Zhu, John Nees, Russell Wilcox, and Almantas Galvanauskas. "Cascading of Coherent Pulse Stacking Using Multiple Gires-Tournois Interferometers." In *Advanced Solid State Lasers*, pp. AW3A-4. Optical Society of America, 2015.

[34] Pulford, Benjamin N. "LOCSET phase locking: operation, diagnostics, and applications." PhD diss., The University of New Mexico, 2011.

[35] Candes, Emmanuel J., Thomas Strohmer, and Vladislav Voroninski. "Phaselift: Exact and stable signal recovery from magnitude measurements via convex programming." *Communications on Pure and Applied Mathematics* 66, no. 8 (2013): 1241-1274.

[36] Stark, Henning, Michael Müller, Marco Kienel, Arno Klenke, Jens Limpert, and Andreas Tünnermann. "Electro-optically controlled divided-pulse amplification." *Optics Express* 25, no. 12 (2017): 13494-13503.